

The School of Mathematics



THE UNIVERSITY
of EDINBURGH

Stability of Selective Solutions to the 3-Body Problem

by

William Jones

Dissertation Presented for the Degree of
MSc in Computational Applied Mathematics

August 2023

Supervised by
Dr. Maximilian Ruffert

Abstract

The general three body problem, which describes three masses interacting freely and purely by gravitational attraction, has been a focus of research in classical mechanics for the past 300 years. Previous analytical work by Euler and Lagrange describes five families of periodic, elliptical, solutions to the problem. Furthermore, modern numerical techniques have unlocked the discovery of many new periodic solutions, such as the distinct ‘figure-8’ orbit. This thesis builds a framework for analysing the stability of such orbits, in both the traditional and Lyapunov sense. It is confirmed that the figure-8 is stable, and Euler and Lagrange’s circular solutions are unstable. A region of stability is found for the figure-8, and the maximum Lyapunov exponents of Euler and Lagrange’s solutions are accurately calculated. The implications of the results are discussed with reference to Celestial mechanics and the N-body problem.

Acknowledgments

I would like to thank my supervisor, Dr Maximilian Ruffert, for providing support and guidance throughout this thesis.

Own Work Declaration

The following work is my own, except when otherwise noted.

Contents

1	Introduction	1
2	Background	2
2.1	Problem Formulation	2
2.2	Integrals of Motion	3
2.3	Keplerian orbits: The two body Case	4
2.4	Euler and Lagrange's 3-Body Solutions	5
2.5	The restricted three-body Problem	6
2.6	The Figure-8 Solution	7
2.7	More 3-body Orbits	8
2.8	N-body Choreographies	8
3	Numerical Integration	9
3.1	Schemes	10
3.1.1	Explicit Euler	10
3.1.2	Symplectic Euler	10
3.1.3	Leapfrog	13
3.1.4	Fourth-order Runge-Kutta	14
3.1.5	Forest-Ruth	16
3.2	Scheme Comparison	18
3.2.1	Scheme order	18
3.2.2	Energy and Angular Momentum	19
3.2.3	Global Error	21
3.2.4	Time Reversibility	22
3.2.5	Results	23
3.3	Time-adaptive Integration	24
3.3.1	Position-velocity dependence	25
3.3.2	Runge-Kutta-Fehlberg	28
4	Three-body orbits	29
4.1	Integration of known Orbits	29
4.1.1	Figure-8	29
4.1.2	Euler's Solution	29
4.1.3	Lagrange's Solution	30
4.2	Stability of the Figure-8	31
4.2.1	Perturbations of the initial Conditions	31
4.2.2	Region of Stability	32
4.2.3	Closure	35
4.2.4	Higher resolution Results	37
4.2.5	Moth I	39
4.2.6	Stability of the Mass	42
4.3	Stabilities of other Orbits	42
4.3.1	Euler's Solution	42
4.3.2	Lagrange's Solution	44
5	Maximum Lyapunov Exponent	46
5.1	Definition of Stability	46
5.2	Measuring the Separation	46
5.3	The Figure-8	48
5.4	Euler and Lagrange's Solutions	50
5.4.1	Initial Investigation	50
5.4.2	Distribution of the MLE	51

5.4.3	An issue with Randomness	51
5.5	N-body Choreographies	53
5.6	Extensions of the MLE	54
6	Conclusions	56
	Appendices	59
	A Source Code	59

List of Tables

1	Butcher Tableau for RK4 [3].	14
2	Estimated order of schemes	18
3	Summary of scheme comparison. Error is the maximum over 100 periods.	24
4	Run-time comparisons of non-adaptive and time-adaptive Leapfrog and PEFRL.	27
5	Butcher Tableau for RKF45 [6, 7].	28
6	Distribution of the MLE over 10000 simulations of the Euler and Lagrange orbits.	51
7	Distribution of the MLE over 2000 simulations of the rotation Euler and Lagrange orbits.	53

List of Figures

1	Two body (Keplerian) Orbits.	5
2	Euler's collinear solution for equal masses.	5
3	Lagrange's triangular solution for equal masses.	6
4	Lagrangian points in CR3BP, in the m_1 reference frame.	6
5	The figure-8 orbit.	7
6	Example solutions to the equal mass three-body problem.	8
7	Example choreographic orbits.	8
8	Ten period, Explicit Euler integration of the two-body equations (2.11) with zero eccentricity and step size $h = 0.1$. Circles indicate initial positions.	10
9	Ten period, Symplectic Euler integration of the two-body equations (2.11) with zero eccentricity and step size $h = 0.1$. Circles indicate initial positions.	11
10	Ten period, Symplectic Euler integration of the two-body equations (2.11) with eccentricity $e = 0.5$ and step size $h = 0.1$	11
11	100 period, Symplectic Euler integration of the two-body equations (2.11) with eccentricity $e = 0.5$ and step size $h = 0.1$	12
12	Ten period, Symplectic Euler integration of the two-body equations (2.11) with eccentricity $e = 0.5$ and step sizes $h = 0.1, h = 0.05$ and $h = 0.025$	12
13	Ten period, Leapfrog integration of the two-body equations (2.11) with eccentricity $e = 0.5$ and step size $h = 0.1$	13
14	100 period, Leapfrog integration of the two-body equations (2.11) with eccentricity $e = 0.5$ and step size $h = 0.1$	14
15	Ten period, Leapfrog integration of the two-body equations (2.11) with eccentricity $e = 0.5$ and step sizes $h = 0.1, h = 0.05$ and $h = 0.025$	14
16	Ten period, RK4 integration of the two-body equations (2.11) with eccentricity $e = 0.5$ and step size $h = 0.1$	15
17	100 period, RK4 integration of the two-body equations (2.11) with eccentricity $e = 0.5$ and step size $h = 0.1$	16
18	Ten period, Forest-Ruth integration of the two-body equations (2.11) with eccentricity $e = 0.5$ and step size $h = 0.1$	17
19	Ten period, PEFRL integration of the two-body equations (2.11) with eccentricity $e = 0.5$ and step size $h = 0.1$	18
20	100 period, PEFRL integration of the two-body equations (2.11) with eccentricity $e = 0.5$ and step size $h = 0.1$	18
21	Relationship between maximum energy error and step size	19
22	Energy comparison with scheme integration of 100 periods of the $e = 0.5$ and $e = 0.8$ ellipses.	20
23	Angular momentum comparison with scheme integration of 100 periods of the $e = 0.5$ and $e = 0.8$ ellipses.	20
24	Scheme integration of m_1 orbiting m_2 on the $e = 0.8$ ellipse, over 100 periods. The exact solution is given by the black ellipse.	21

25	Global error comparison with scheme integration of 100 periods of the $e = 0.5$ and $e = 0.8$ ellipses.	22
26	Time invariance comparison for scheme integration of 100 periods of the $e = 0.5$ and $e = 0.8$ ellipses.	23
27	Integration of a hyperbolic orbit using PEFRL and step size $h = 0.1$	24
28	Proposed two-body step size over ten periods of the $e = 0.5$ ellipse. Colour indicates the distance between the bodies.	25
29	Time-adaptive non-symplectic integration of the $e = 0.5$ ellipse with Leapfrog ($C = 0.16$) and PEFRL ($C = 0.55$).	26
30	Time-adaptive near-symplectic integration of the $e = 0.5$ ellipse with Leapfrog ($C = 0.16$) and PEFRL ($C = 0.55$).	26
31	Adaptive integration of a hyperbolic orbit using PEFRL and step scaler $C = 0.1$. .	27
32	Adaptive integration of a hyperbolic orbit using RK45 with $\tau = 10^{-6}$	28
33	10 period, Figure-8 integration with $C = 0.1$	29
34	10 period, integration of Euler's equal-mass, circular solution with $C = 0.1$	30
35	10 period, integration of Lagrange's equal-mass, circular solution with $C = 0.1$. .	31
36	10 period, integration of Lagrange's equal-mass, circular solution with $C = 0.001$. .	31
37	Step size distribution for the fig-8 orbit over 200 orbits, with $C = 0.5$	32
38	Zoomed-out, region of stability of the figure-8 orbit.	33
39	Region of stability of the figure-8 orbit, with $C = 0.4$	33
40	Region of stability of the figure-8 orbit, with $C = 0.2$	34
41	Region of stability of the figure-8 orbit, with $C = 0.4$ and adjusted parameters. .	34
42	Example 'stable', perturbed figure-8 orbits.	35
43	Grid coverage for the un-perturbed and perturbed figure-8 orbit. Unperturbed covers 249 grid-squares, perturbed covers 1650.	36
44	Closure (%) of perturbations of the figure-8, with grid-size 500x500.	36
45	Closure (%) of perturbations of the figure-8, with varying grid sizes.	37
46	Closure of perturbations of the figure-8 orbit. Darker colours indicate regions of low closure.	37
47	Escape times of perturbations of the figure-8 orbit. Lighter colours indicate regions of higher escape times. Darker colours indicate regions of low escape times. .	38
48	Maximum energy error (%) of perturbations of the figure-8 orbit. Lighter colours indicate regions of low energy. Darker colours indicate regions of high energy. .	38
49	Maximum energy error (%) of perturbations of the figure-8 orbit, where $E < 0.007\%$. .	39
50	Closure (%) of the Moth I orbit.	39
51	20 period integration of Moth I with initial conditions $R = 1.05205$, $p'_1 = 0.46998$ and $p'_2 = 0.37707$	40
52	Progressive zooming on the closure (%) of Moth I.	40
53	20 period integration of Moth I with initial conditions $R = 1.071789884$, $p'_1 = 0.450566112$ and $p'_2 = 0.381389032$	41
54	Escape times of perturbations of the figure-8 orbit, capped to 8 periods.	41
55	Stability of the masses of the figure-8 orbit.	42
56	Stability of Euler's circular equal-mass solution.	43
57	Trajectories of perturbations of Euler's circular equal-mass solution.	43
58	Stability of the collinearity of Euler's solution.	44
59	Stability of Lagrange's circular equal-mass solution.	44
60	Stability of the triangular configuration of Lagrange's solution.	45
61	Separation of the figure-8 orbit and a small perturbation of order 10^{-6} , with different distance metrics.	47
62	Energy error of 300 orbits of the figure-8, with $C = 0.065$	47
63	Euclidean distance between the figure-8 orbit and a small perturbation of order 10^{-6} , in the adjusted phase space.	48
64	Separation of small perturbations of nearby orbits to the figure-8.	49

65	Analysis on the unstable orbit. $\delta v_x = -0.2$ & $\delta v_y = 0.2$: $r_m = 0.68$, $v_m = 24.47$	49
66	Separation of Euler and Lagrange's circular equal-mass three-body solutions.	50
67	10000 estimations of the MLE of Euler and Lagrange's circular equal-mass three-body solutions.	52
68	Uniformly distributed perturbations in the xy -plane.	53
69	2000 estimations of the MLE of rotated Euler and Lagrange's solutions.	53
70	Integration of the 4-circle, with $C = 0.1$	54
71	Integration of the 5-circle, $C = 0.1$	54
72	1000 estimates of the MLE for the N-circle, with $3 \leq N \leq 20$	55

1 Introduction

First proposed by Sir Isaac Newton, the general three-body problem is one of the oldest questions in classical mechanics: If we know the positions and velocities of three masses, which interact via mutual gravitational attraction, can we predict the subsequent motion?

For 300 years, mathematicians have been looking for answers to this question to make sense of the Sun-Earth-Moon system and other celestial mechanics. The problem gained huge traction in the 18th and 19th centuries, captivating names such as Euler, Lagrange and Poincaré. It continues to attract researchers today as the three-body problem has applications in quantum-mechanics, the examination of new candidate exoplanets and in space mission design [23, 27].

Within his *Principia 1687*, Newton built upon work published by Johannes Kepler in 1609 and solved the two-body problem. Here he derived Kepler's laws of planetary motion by describing two orbiting bodies as moving on two separate conics, in the shape of a circle, ellipse, parabola or hyperbola.

Unlike the two-body case, the general three-body problem has no general, closed-form solution, but explicit formulas have been found for five families of periodic orbits [23, 34]. The first three were discovered by Leonhard Euler [5] in 1767, where the three masses are arranged to be collinear at each instant. Euler showed that, with the right initial conditions, this line rotates around the centre of mass, resulting in elliptical periodic orbits of all three orbits.

Five years later, Joseph-Louis Lagrange discovered two other families, the existence of equilateral triangle configurations [15]. The bodies remain as the vertices of a triangle and move on their own elliptical orbits about the centre of mass. These five families of solutions make up the so-called relative equilibrium solutions, or central configurations, where all bodies rotate around the centre of mass with a constant mutual distance between them.

The nature of the three-body problem means it conserves standard mechanical quantities like energy and angular momentum, known as integrals of motion. It was suspected to conserve other non-classical integrals of motion, but in 1887 Heinrich Bruns proved that no such quantities exist [2, 23, 32], at least those expressible by the positions and velocities of the bodies. At a similar time, Henri Poincaré proved the existence of chaotic dynamics within the three-body problem, a finding that implies the three-body problem can never truly be solved in terms of algebraic formulas and integrals as Newton did for two bodies [32]. One century on Karl Sundman did manage to find an infinite series theoretically capable of summing to a solution with non-zero angular momentum, but sadly it was found to converge slowly and be of little use [32, 23].

Fortunately, through the relatively modern technique of numerical integration we can now generate approximations of orbits, with accuracy really only limited to computing power. This has led to the discovery of many new families of periodic orbits of three or more bodies [34]. M. Šuvakov [34] describes a method of finding periodic three-body orbits, and suggests there are many more to be found, especially with large periods. A. Chenciner and R. Montgomery [21] found the distinct figure-8 orbit, with three bodies moving along the same path, known as a choreography. Simo [28] went further and has found a large collection of N-body choreographies by defining an action on the dynamical system and minimising it.

Euler and Lagrange's solutions are generally thought to be unstable, whilst the figure-8 is thought to be stable [21, 23]. This thesis aims to study the stability of these solutions with the intention of learning more about 3-body dynamics. The motivation is to build a framework of stability analysis that can be applied to other known three-body orbits, and extend to N-body interactions with applications in celestial mechanics.

The structure of this thesis is as follows: The first chapter focuses on finding a suitable integration scheme which is not only fast and accurate but also conserves mechanical quantities such as energy and angular momentum. With use of the Kepler orbits as a test case, it turns out an adaptive fourth-order Forest-Ruth [25] scheme is appropriate. Further chapters focus on integrating nearby trajectories of the figure-8, Euler and Lagrange orbits to investigate the region of stability of each. Next, we analyse the maximum Lyapunov exponents and compare to prior results. Lastly, we discuss the extensions of this method to N-body choreographies and applications of the stability analysis.

2 Background

2.1 Problem Formulation

In the general three-body problem, three arbitrary masses move in three-dimensional space according to Newton's law of universal gravitation,

$$F = G \frac{mM}{r^2}. \quad (2.1)$$

If the motion of the bodies are confined to one plane this is called the planar general three-body problem. Throughout this thesis we use Newton's theory of gravity (2.1) to study these planar gravitational interactions, but we will compute in three-dimensional space to maintain flexibility.

Solving the general three-body problem requires the past and future motions to be uniquely determined by the present positions and velocities of the bodies. Furthermore, we work under the assumption that the masses are point masses and are not influenced by any other forces. With this in mind, let the bodies have masses m_1, m_2 and m_3 and respective positions $\mathbf{r}_1(t), \mathbf{r}_2(t)$ and $\mathbf{r}_3(t)$ in three-dimensional, Cartesian space. Then the governing equations of motion can be written as a system of nine second-order, autonomous, ODEs [23]

$$\begin{cases} \mathbf{F}_1 = \mathbf{F}_{12} + \mathbf{F}_{13} = m_1 \ddot{\mathbf{r}}_1 &= -G \frac{m_1 m_2}{|\mathbf{r}_2 - \mathbf{r}_1|^3} (\mathbf{r}_2 - \mathbf{r}_1) - G \frac{m_1 m_3}{|\mathbf{r}_3 - \mathbf{r}_1|^3} (\mathbf{r}_3 - \mathbf{r}_1), \\ \mathbf{F}_2 = \mathbf{F}_{21} + \mathbf{F}_{23} = m_2 \ddot{\mathbf{r}}_2 &= -G \frac{m_2 m_1}{|\mathbf{r}_1 - \mathbf{r}_2|^3} (\mathbf{r}_1 - \mathbf{r}_2) - G \frac{m_2 m_3}{|\mathbf{r}_3 - \mathbf{r}_2|^3} (\mathbf{r}_3 - \mathbf{r}_2), \\ \mathbf{F}_3 = \mathbf{F}_{31} + \mathbf{F}_{32} = m_3 \ddot{\mathbf{r}}_3 &= -G \frac{m_3 m_1}{|\mathbf{r}_1 - \mathbf{r}_3|^3} (\mathbf{r}_1 - \mathbf{r}_3) - G \frac{m_3 m_2}{|\mathbf{r}_2 - \mathbf{r}_3|^3} (\mathbf{r}_2 - \mathbf{r}_3), \end{cases} \quad (2.2)$$

where G is the gravitational constant, \mathbf{F}_{ij} is the force of mass j acting on mass i , \mathbf{F}_i is the resultant force acting on mass i and derivatives are with respect to time. Notice that $\mathbf{F}_{ij} = -\mathbf{F}_{ji}$ so this force calculation can be stored and re-used, cutting computational time in half. A system of second order ODEs can be awkward and slow to work with so instead we make use of the velocities $\mathbf{v}_1(t), \mathbf{v}_2(t)$ and $\mathbf{v}_3(t)$ and state it equivalently as a system of 18 first order ODEs,

$$\begin{cases} \dot{\mathbf{r}}_1 &= \mathbf{v}_1, \\ \dot{\mathbf{r}}_2 &= \mathbf{v}_2, \\ \dot{\mathbf{r}}_3 &= \mathbf{v}_3, \\ \dot{\mathbf{v}}_1 &= -G \frac{m_2}{|\mathbf{r}_2 - \mathbf{r}_1|^3} (\mathbf{r}_2 - \mathbf{r}_1) - G \frac{m_3}{|\mathbf{r}_3 - \mathbf{r}_1|^3} (\mathbf{r}_3 - \mathbf{r}_1), \\ \dot{\mathbf{v}}_2 &= -G \frac{m_1}{|\mathbf{r}_1 - \mathbf{r}_2|^3} (\mathbf{r}_1 - \mathbf{r}_2) - G \frac{m_3}{|\mathbf{r}_3 - \mathbf{r}_2|^3} (\mathbf{r}_3 - \mathbf{r}_2), \\ \dot{\mathbf{v}}_3 &= -G \frac{m_1}{|\mathbf{r}_1 - \mathbf{r}_3|^3} (\mathbf{r}_1 - \mathbf{r}_3) - G \frac{m_2}{|\mathbf{r}_2 - \mathbf{r}_3|^3} (\mathbf{r}_2 - \mathbf{r}_3). \end{cases} \quad (2.3)$$

We can generalise to include any N-body system with $N \geq 2$,

$$\begin{cases} \dot{\mathbf{r}}_i &= \mathbf{v}_i \\ \dot{\mathbf{v}}_i &= -G \sum_{j=1, j \neq i}^N \frac{m_j}{|\mathbf{r}_j - \mathbf{r}_i|^3} (\mathbf{r}_j - \mathbf{r}_i), \end{cases} \quad (2.4)$$

where $i = 1, \dots, N$. The general N-body equations 2.4 are implemented in Python 3.0 and unless stated otherwise, we take $G = 1$ and $m_i = 1, \forall i$. As mentioned in Section 1, it's impossible to describe every solution to (2.4) when $N \geq 3$ [23]. Therefore, we must use computational techniques to integrate and analyse them. We will be focusing periodic solutions so that $\mathbf{r}_i(t) = \mathbf{r}_i(t + T)$, where T is the period. The aim of this thesis is to study the dynamics of example periodic orbits that obey the governing equations 2.3 and address questions about their stabilities. We extend the scope of this to include N-body choreographic solutions to system 2.4, where \mathbf{r}_i follow the same path about a common centre of mass.

2.2 Integrals of Motion

As a consequence of being Hamiltonian, the N-body system (2.4) conserves many standard mechanical quantities, known as integrals of motion. For the three-body problem there are ten integrals of motion, which reduces the 18 ODEs to eight. In fact, Musielak [23] tells us there are a further two when considering the elimination of both time and the ‘ascending node’, reducing the system to 6 ODEs. In 1887 Bruns [2] proved that no other independent integrals of motion exist so an important note is that even if we confine motion to a plane fixed in space this only reduces our system to 4, which is generally unsolvable.

The following are conserved integrals of motion: mass, total linear momentum, total angular momentum and total Energy [14, 32, 23]. As a consequence of the conservation of linear momentum, the centre of mass (CM) moves at a constant velocity (or stays at rest) and its derivative is zero. The N-body CM and its derivative is defined as

$$\mathbf{r}_{CM} = \frac{\sum_{i=1}^N m_i \mathbf{r}_i}{\sum_{i=1}^N m_i} \quad \text{and} \quad \mathbf{v}_{CM} = \frac{\sum_{i=1}^N m_i \mathbf{v}_i}{\sum_{i=1}^N m_i}, \quad (2.5)$$

respectively. Since linear momentum is conserved, we will use the CM reference frame. The transformation $\mathbf{r}'_i = \mathbf{r}_i - \mathbf{r}_{CM}$ and $\mathbf{v}'_i = \mathbf{v}_i - \mathbf{v}_{CM} \forall i = 1, \dots, N$ places the CM at the origin with no impact on the overall dynamics, so that

$$\sum_{i=1}^N m_i \mathbf{r}'_i = \sum_{i=1}^N m_i \mathbf{v}'_i = \mathbf{0}. \quad (2.6)$$

This has the desired effect of forcing the total linear momentum, ρ' , to be zero

$$\rho' = \sum_{i=1}^N \rho'_i = \sum_{i=1}^N m_i \mathbf{v}'_i = \mathbf{0}. \quad (2.7)$$

With zero linear momentum the CM will remain in place when moving through time. As a consequence, we need only apply this transformation once, to the initial conditions. We will do this before any numerical integration and drop the primes from now on.

Moreover, the angular momentum of one body is defined as the cross-product of its position and momentum, $\mathbf{L}_i = m_i \mathbf{r}_i \times \mathbf{v}_i$, i.e. it describes the rotational motion as a vector perpendicular to the plane of motion. We are not really concerned with its direction as a ‘quantity’ so we will take its magnitude. The total angular momentum is therefore

$$L = \left| \sum_{i=1}^N m_i \mathbf{r}_i \times \mathbf{v}_i \right|. \quad (2.8)$$

The final and most important quantity to consider is energy. The total energy of the system is defined in terms of the kinetic (K) and potential (U) energies as

$$E = K + U \quad \text{where} \quad K = \frac{1}{2} \sum_{i=1}^N m_i |\mathbf{v}_i|^2 \quad \text{and} \quad U = -G \sum_{i=1}^N \sum_{j>i}^N \frac{m_i m_j}{|\mathbf{r}_j - \mathbf{r}_i|}. \quad (2.9)$$

Notice the $j > i$ condition, which ensures we only calculate the pairwise potential energies once. If instead we were to calculate the potential energy acting on each body and sum all these we would get a result double in value. As simple as it sounds, this caused a few issues in implementation. The term $\mathbf{r}_j - \mathbf{r}_i$ and its magnitude are used in the force calculation. Re-using these values speeds up implementation.

Montgomery [21] suggests that the negativity of the Energy is important for periodic solutions of N-body systems as it implies boundedness, which implies periodicity. Generally, very

little is known about N-body systems with negative energies, and they are thought to have a mix of chaotic and near-integrable Kolmogorov–Arnold–Moser (KAM) stability [21, 19].

Finally, we can define the Lagrangian as $\mathcal{L} = K - U$, and in turn the action as

$$A(\mathbf{r}) \equiv \int_0^T \mathcal{L}(\mathbf{r}(t), \mathbf{v}(t)) dt. \quad (2.10)$$

By using minimisation techniques and the ‘Least Action Principle’ we can look for candidates that minimise the action in fourier space and are possible solutions to the n-body problem [28, 29, 21]. This plays a key role in looking for N-body choreographies.

2.3 Keplerian orbits: The two body Case

Before we explore any three-body solutions we need to first understand the two-body case, otherwise known as Kepler’s orbits:

$$\begin{cases} \mathbf{F}_{12} = m_1 \ddot{\mathbf{r}}_1 &= -G \frac{m_1 m_2}{|\mathbf{r}_2 - \mathbf{r}_1|^3} (\mathbf{r}_2 - \mathbf{r}_1), \\ \mathbf{F}_{21} = m_2 \ddot{\mathbf{r}}_2 &= -G \frac{m_2 m_1}{|\mathbf{r}_1 - \mathbf{r}_2|^3} (\mathbf{r}_1 - \mathbf{r}_2). \end{cases} \quad (2.11)$$

Kepler’s three laws of planetary motion describe the motion of one mass orbiting a much larger mass (e.g. the Earth and Sun) where the larger mass does not move [14, 20]. The two-body problem is a lot more general than this, but we can utilise the mathematics behind it. We describe the motion of m_1 orbiting m_2 as $\mathbf{r} = \mathbf{r}_1 - \mathbf{r}_2$ and

$$\ddot{\mathbf{r}} = \ddot{\mathbf{r}}_1 - \ddot{\mathbf{r}}_2 = \frac{\mathbf{F}_{12}}{m_1} - \frac{\mathbf{F}_{21}}{m_2} = \frac{1}{\mu} \mathbf{F}_{12}, \quad (2.12)$$

where $\mu = \frac{m_1 m_2}{m_1 + m_2}$ is the reduced mass. From this we can recover the motion of both bodies about the CM by

$$\begin{cases} \mathbf{r}_1(t) &= \mathbf{r}_{CM} + \frac{m_2}{m_1 + m_2} \mathbf{r}(t) \\ \mathbf{r}_2(t) &= \mathbf{r}_{CM} - \frac{m_1}{m_1 + m_2} \mathbf{r}(t) \end{cases} \quad (2.13)$$

Kepler’s laws tells us that, in the plane of motion, the path of \mathbf{r} takes the polar shape

$$r(\varphi) = \frac{a(1 - e^2)}{1 + e \cos \varphi} = a - ae \cos \Phi, \quad (2.14)$$

where a is the ‘semi-major axis’ (size), e is the eccentricity (shape), φ is the true anomaly and Φ is the eccentric anomaly [4]. The eccentricity, semi-major axis and period are defined as

$$e^2 = 1 + \frac{2\epsilon l^2}{\alpha^2} = 1 + \frac{2E_0 L_0^2}{\mu^3 \alpha^2}, \quad (2.15)$$

$$a = \frac{r(0)}{1 - e} \quad \text{and} \quad (2.16)$$

$$T^2 = \frac{4\pi^2}{\alpha} a^3, \quad (2.17)$$

where ϵ is the specific orbital energy, l the specific relative angular momentum and $\alpha = G(m_1 + m_2)$ the standard gravitational parameter [14, 20, 4]. Equation (2.15) is always non-negative [4] so equation (2.14) represents an ellipse with eccentricity e for $E_0 < 0$, a parabola for $E_0 = 0$ and a hyperbola for $E_0 > 0$. Furthermore, equation (2.14) can be represented as function of time

$$\frac{a^4(1-e^2)^2}{(1+e\cos\varphi-\varphi^*)^2}d\varphi = L_0dt, \quad (2.18)$$

where φ^* is found by the initial conditions. After integration, this represents an implicit equation for $\varphi(t)$ [4]. Using the CM reference frame ($\mathbf{r}_{CM} = 0$) equation (2.14) describes the two orbiting bodies moving around the CM on two separate conics, in one of the shapes shown in Figure 1.

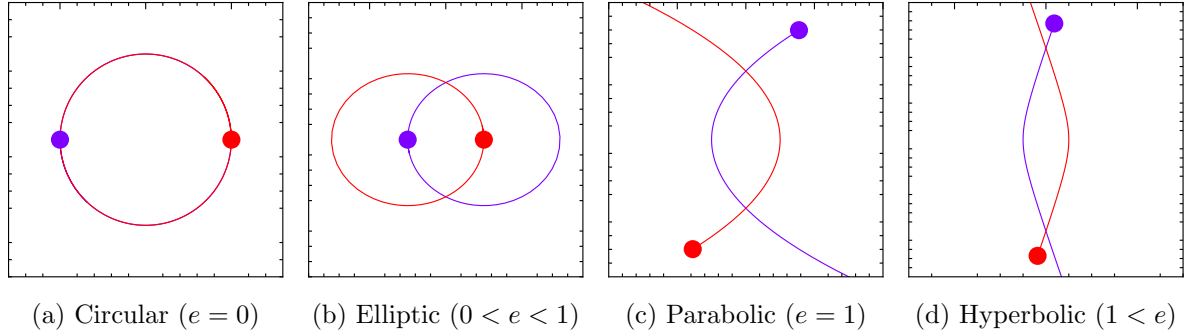


Figure 1: Two body (Keplerian) Orbits.

2.4 Euler and Lagrange's 3-Body Solutions

As mentioned in Section 1, though the general three-body problem is broadly unsolvable, there do exist five families of solutions to which we can describe the full motion.

The first three families come from Euler [5] in 1765, who arranged the three masses on a line and showed that, under the right initial conditions, the three masses orbit on ellipses about the centre of mass while maintaining their original structure and distance ratios (figure 2). One such proof of the succeeding motion can be seen in [9]. We gain three families by placing each mass in the centre.

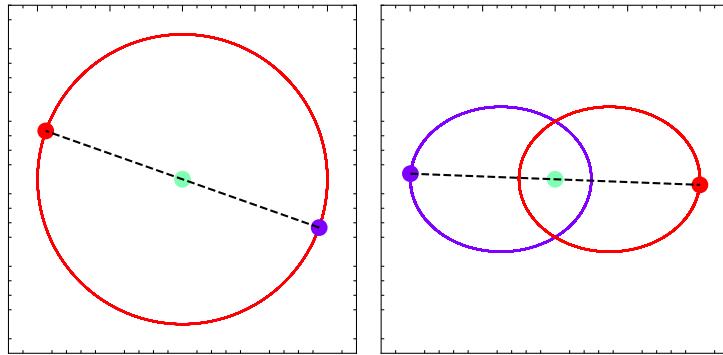


Figure 2: Euler's collinear solution for equal masses.

Seven years later and Lagrange discovered two families of solutions by placing the masses at the vertices of an equilateral triangle (figure 3). The bodies orbit the centre of mass on ellipses while remaining vertices of an equilateral triangle. We can arrange the masses on a triangle in two distinct ways, giving two families.

Together, the five families form the ‘Central Configurations’ of the three-body problem, meaning that if you released them from rest they would collapse to a single point. It has been shown that the Euler families are asymptotically unstable, and the Lagrange families are generally unstable unless one of the masses is much larger than the others [9]. Some regions of stability of the Lagrange families were found by Mansilla in 2006 [17]. This thesis will analyse the stability of the simplest case of both families, focusing on the equal mass case with all masses moving about the CM in a circle.

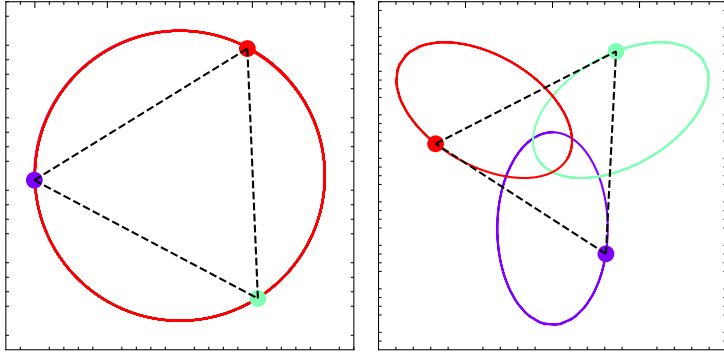


Figure 3: Lagrange’s triangular solution for equal masses.

2.5 The restricted three-body Problem

In addition to the central configurations, while investigating the Sun-Earth-Moon system Euler developed what is now known as the circular restricted three-body problem (CR3BP), as well as the elliptic restricted three-body problem (ER3BP) [23, 5]. By modelling one of the bodies as mass-less (i.e. the moon) it can be decoupled from the remaining two. Without loss of generality, making m_3 mass-less gives

$$\begin{cases} \ddot{\mathbf{r}}_1 = -G \frac{m_2}{|\mathbf{r}_2 - \mathbf{r}_1|^3} (\mathbf{r}_2 - \mathbf{r}_1), \\ \ddot{\mathbf{r}}_2 = -G \frac{m_1}{|\mathbf{r}_1 - \mathbf{r}_2|^3} (\mathbf{r}_1 - \mathbf{r}_2), \\ \ddot{\mathbf{r}}_3 = -G \frac{m_1}{|\mathbf{r}_1 - \mathbf{r}_3|^3} (\mathbf{r}_1 - \mathbf{r}_3) - G \frac{m_2}{|\mathbf{r}_2 - \mathbf{r}_3|^3} (\mathbf{r}_2 - \mathbf{r}_3), \end{cases} \quad (2.19)$$

which Euler went on to formulate in a rotating (synodic) frame [23, 5], and is solvable.

This was built upon by Lagrange in his prize-winning paper *Essai sur le Probleme des Trois Corps, 1772* [15] where he came up with the idea of equilibrium points. Otherwise known as Lagrange points, these correspond to the collinear solutions found by Euler L_1, L_2 and L_3 and the namesake triangular points L_4 and L_5 . To be more precise, they are the locations where the gravitational pull due to m_1 and m_2 balances with the centripetal force needed for a ‘mass-less’ object m_3 to move with them. Figure 4 shows where the Lagrange points lie in relation to m_2 orbiting m_1 . It has been shown that L_1, L_2 and L_3 are unstable, whereas L_4 and L_5 are stable so long as $m_2/m_1 > 24.96$ [24], which is satisfied for the Sun-Earth system.

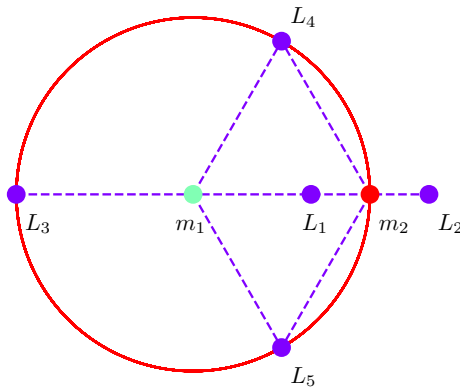


Figure 4: Lagrangian points in CR3BP, in the m_1 reference frame.

In the Sun-Earth system, L_2 is the home of the James Webb Space Telescope, which orbits about the equilibrium point. Being at L_2 makes communication easy and provides a good view of deep space, but at this timescale L_2 is unstable at 23 days so it has to undergo some course corrections [24].

Additionally, in 2010 NASA's WISE telescope confirmed that a Trojan asteroid TK7 orbits Earth's leading Lagrange point, L_4 . This is stable so no course-correction is needed for the asteroid. Many more Trojan asteroids, first discovered by German astronomer August Kopff in 1906-1907, have been confirmed to exist at Jupiter's L_4 and L_5 points.

Unlike the general three-body problem, Jacobi [13] took Euler's new synodic reference frame and proved the existence of a new integral of motion, the Jacobi integral. This allowed Hill [12] to find regions in space where m_3 is allowed to move, known as zero-velocity curves. He also established an even more niche case of CR3BP where two of the masses are negligible compared to the remaining one. Think of m_2 and m_3 orbiting each other while both orbiting m_1 , i.e. the Sun-Earth-Moon system. This opened the doors for a new set of periodic solutions to be established.

All of this history demonstrates how relevant understanding the dynamics of the three-body problem is in celestial mechanics. With enough time and the right tools, it would be interesting to study CR3BP or ER3BP in more detail, especially regarding the stability of placing example objects into Lagrange points.

2.6 The Figure-8 Solution

Fast-forward to the modern day and researchers are no longer using analytical techniques to search for solutions to the three and N-body problem. In 1912 Sundman did find a power series expansion to the three-body problem with non-zero angular momentum, but it was found to converge slowly and provide little use [11, 23, 21]. Therefore, it makes sense to use the modern computational power at our disposal to look for new solutions.

In 1993 C. Moore discovered the first known periodic solution to the three-body problem with zero angular momentum, what is now known as the figure-8 solution [22], shown in figure 5. In 2000 R. Montgomery and A. Chenciner rediscovered and popularised it [21], inspiring the discovery of many new equal mass N-body 'choreographies' by Simó [28]. This periodic orbit will form the backbone of the thesis, with most analysis focusing on it.

The figure-8 is a periodic solution to the general three-body problem with equal mass. If T is the period of the orbit, then $\mathbf{r}_2(t) = \mathbf{r}_1(t - T/3)$ and $\mathbf{r}_3(t) = \mathbf{r}_1(t - 2T/3)$. The bodies move along a figure-8 shaped curve, phase shifted from each other by $T/3$.

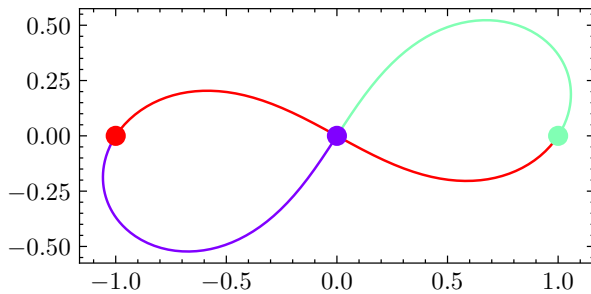


Figure 5: The figure-8 orbit.

It's important to note that the figure-8 can be translated, rotated, scaled and flipped to give variations of the orbit, but the underlying dynamics are thought to be unique [21]. Montgomery [21] suggests that by scaling symmetry there exists a figure-8 for any period, and that it is unique according to numerical investigations, but this is yet to be proved.

To analyse the stability of this we have access to the Kolmogorov–Arnold–Moser (KAM) theorem [19] which tells us that an orbit is KAM stable if solutions through most initial conditions sufficiently close stay near it for all time. For those that do leave, they leave so slowly that they can't be identified by any power series. Simó proved that the fig-8 is KAM stable [29] but this thesis will provide more analysis by also considering its Lyapunov stability [16]. The stability of the figure-8 is interesting as it means, in theory, we could find a solar system with

this exact set-up. Calculations put this at somewhere in the region of one per galaxy to one per universe [21].

2.7 More 3-body Orbits

In 2013, Šuvakov and Dmitrašinović found a further 13 new periodic solutions to the equal mass general three-body problem [34]. They provide an in-depth guide for those willing to look for more solutions, suggesting that for large periods of $T > 100$ relative to orbit size there are plenty more to be found. Some examples can be seen in Figure 6. This would provide an interesting subject of further research - Can more be found? Or can we analyse the stability of some of these new orbits?

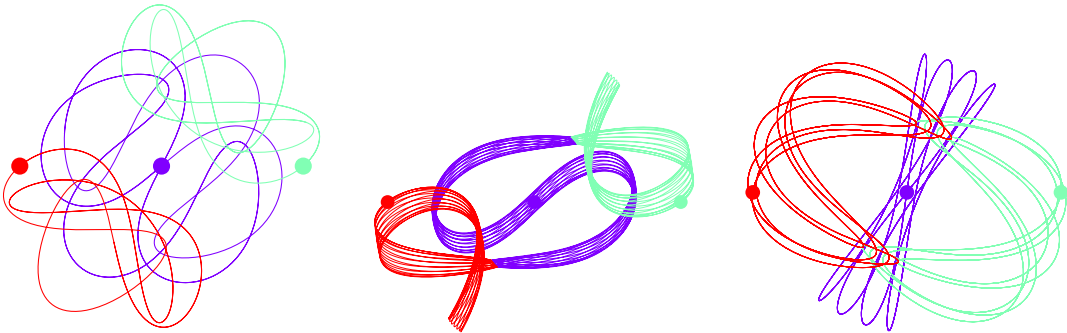


Figure 6: Example solutions to the equal mass three-body problem.

2.8 N-body Choreographies

Lastly, we can look at N-body choreographies. These are periodic solutions to the equal-mass N-body problem where each particle follows the same trajectory, phase shifted by T/N . By dreaming up trajectories and minimising the action (2.10) in Fourier space, Simó [29] was able to find many of these orbits. The key point is that minimising the action avoids collisions, so we are more likely to find a periodic orbit. Many questions can be asked about these. Can we find some of our own? Do they have any symmetries? Or what about stability? This thesis aims to formulate a method to answer the latter, but first we need some tools to do so.

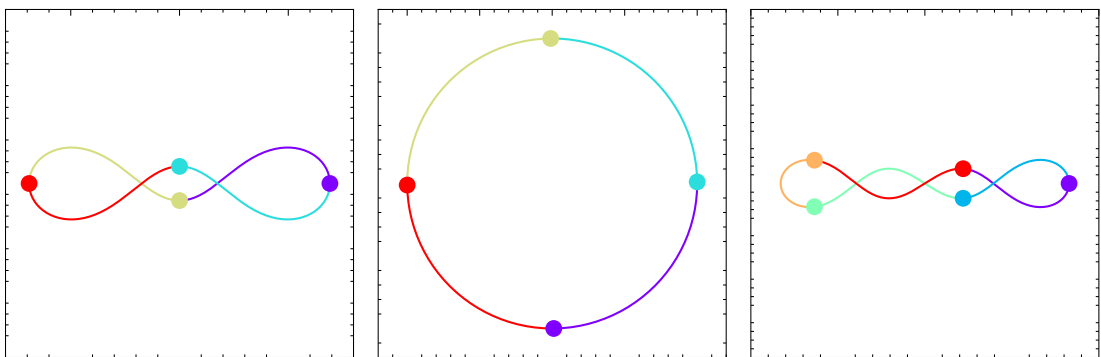


Figure 7: Example choreographic orbits.

3 Numerical Integration

The primary goal of this section is to find a suitable numerical scheme to integrate the N-body system (2.4) forward or backward in time, to an arbitrary level of accuracy. We test schemes on the equal mass two-body problem in the xy -plane, described in sections 2.1 and 2.3, where $G = m_1 = m_2 = 1$. These cases work well as the exact behaviour of different eccentricities (2.15) is known, so it is easy to spot obvious implementation errors. For the elliptical case ($0 \leq e < 1$) we choose the initial conditions

$$\begin{cases} \mathbf{r}_1(0) = [e - 1, 0, 0]^T, & \mathbf{r}_2(0) = [1 - e, 0, 0]^T, \\ \mathbf{v}_1(0) = [0, -\sqrt{\frac{1+e}{1-e}}, 0]^T, & \mathbf{v}_2(0) = [0, +\sqrt{\frac{1+e}{1-e}}, 0]^T, \end{cases} \quad (3.1)$$

so that $E_0 = -1/4$, $L_0^2 = 1 - e^2$, $a = 2$ and $\varphi^* = 0$, with a period $T = 4\pi$. Negative energy implies these are indeed bounded ellipses, and equation (2.15) confirms the eccentricity.

We could just integrate system (2.11) with these initial conditions and compare to the analytic solution (2.18) but when $N \geq 2$ we generally can't do this. However, we still want to be confident when integrating an unknown orbit and need to be able to measure this confidence. A popular technique when integrating analytically unsolvable systems is to watch the change in energy and angular momentum. We expect these quantities to remain constant, so anything else suggests an error in calculation.

Using angular momentum (2.8) and energy (2.9) has the obvious advantage of being expressed in terms of position and velocity, so they are calculable at all time. However, the main challenge of this approach is that if the energy of an orbit were to change by one, this suggests a large error in a system with initial energy one, but a small error in a system with initial energy 100. In actuality, we actually want to know the absolute change in energy relative to the initial energy. We define the relative energy error as

$$E_{err} = \frac{|E - E_0|}{\hat{E}_0}, \quad (3.2)$$

where E_0 is the initial energy error and $\hat{E}_0 = |E_0|$ if $E_0 \neq 0$ and $\hat{E}_0 = \max_i |E_0^i|$ otherwise. This is a fractional representation, so a value of 0.01 would represent an error of 1%. We define the relative angular momentum error similarly, as

$$L_{err} = \frac{|L - L_0|}{\hat{L}_0}, \quad (3.3)$$

where L_0 is the initial angular momentum and $\hat{L}_0 = |L_0|$ if $L_0 \neq 0$ and $\hat{L}_0 = \max_i |L_0^i|$ otherwise. We could go one step further and analyse the linear momentum also, but the CM reference frame forces this to be zero, so it's not much use as an estimate of the relative error.

The schemes we consider in this section are Explicit Euler, Symplectic Euler, Leapfrog, Fourth-Order Runge-Kutta and Forest-Ruth [4, 1, 3, 25, 8]. Each is defined generally for N-bodies and this section performs an in-depth comparison of each, concluding that a Forest-Ruth scheme is the most appropriate. Finally, a time-adaptive modification is considered to speed up calculations.

3.1 Schemes

3.1.1 Explicit Euler

The first scheme considered is Explicit Euler. This is a first order scheme taking the general vector form $\mathbf{y}_{n+1} = \mathbf{y}_n + h f(\mathbf{y}_n)$ where $h = \Delta t$ is the time-step and $f(\mathbf{y}_n)$ defines the derivative of \mathbf{y} [4, 1]. In this context, we define a step as

$$\begin{aligned} (\mathbf{r}_i)_{n+1} &= (\mathbf{r}_i)_n + h(\mathbf{v}_i)_n, \\ (\mathbf{v}_i)_{n+1} &= (\mathbf{v}_i)_n + h(\dot{\mathbf{v}}_i)_n, \end{aligned} \quad (3.4)$$

for $i = 1, \dots, N$ and initial conditions $(\mathbf{r}_i)_0 = \mathbf{r}_i(t_0)$, $(\mathbf{v}_i)_0 = \mathbf{v}_i(t_0)$. We implement and test it on the simplest of the two-body orbits with eccentricity $e = 0$ and initial conditions (3.1).

Zero eccentricity is the lower limit case of the ellipses so both masses should move around the centre of mass in a circle. As a result the masses will be the same distance apart, and maintain their initial speed at all time. Integration is done over ten periods with a step size of $h = 0.1$, defined relative to the period so that $h/T \approx 0.008$. These are somewhat arbitrarily picked but it is seen that they highlight the differences between schemes.

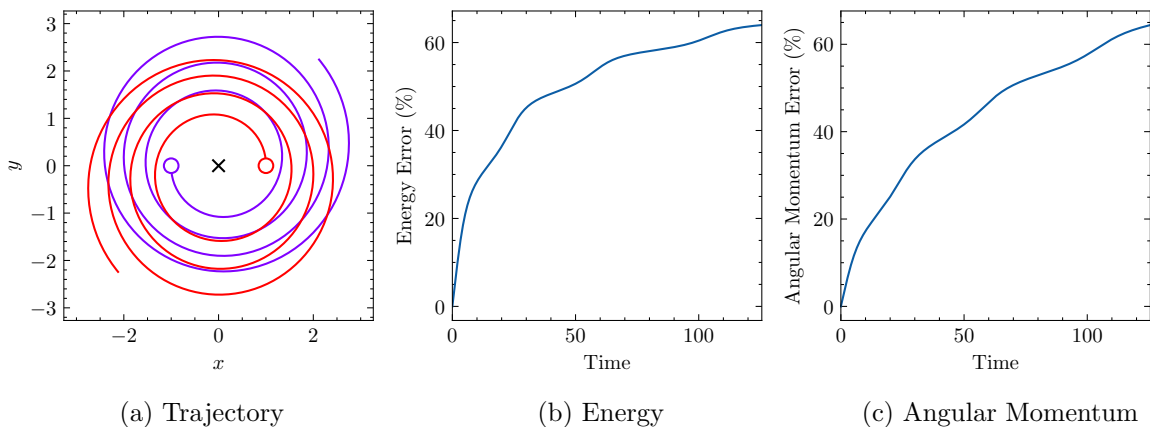


Figure 8: Ten period, Explicit Euler integration of the two-body equations (2.11) with zero eccentricity and step size $h = 0.1$. Circles indicate initial positions.

Such an integration gives Figure 8. The masses do not stay on a circle but instead spiral outwards. Behaviour like this is somewhat expected, as Explicit Euler is a first order scheme it is widely considered not very accurate unless the step size is small (a trade-off with computational run-time) [1]. Regardless, the energy and angular momentum error both increase to a high error (~ 60%). Dropping the step-size would scale the error down but it would still not be conserved. This motivates looking for a scheme more specific to our problem, one that keeps the integrals of motion bounded at the very least.

3.1.2 Symplectic Euler

The solution to unbounded energy comes in the form of symplectic integrators, which are numerical integration schemes developed specifically for Hamiltonian systems. Mathematically speaking, symplectic means that the solution exists on a symplectic manifold, a solution set which is defined by a 2-form [1]. This isn't very helpful - for our purposes the notion of symplectic refers to both the conservation of Hamiltonian quantities and time-reversibility. The simplest of the symplectic integrators is the first-order Symplectic Euler scheme (otherwise known as Euler-Cromer) [4, 1] where

$$\begin{aligned} (\mathbf{v}_i)_{n+1} &= (\mathbf{v}_i)_n + h(\dot{\mathbf{v}}_i)_n, \\ (\mathbf{r}_i)_{n+1} &= (\mathbf{r}_i)_n + h(\mathbf{v}_i)_{n+1} \end{aligned} \quad (3.5)$$

for $i = 1, \dots, N$. It is a variation on Explicit Euler that, at each step, first calculates the new momenta and uses that to calculate the new positions. There is one force calculation ($\dot{\mathbf{v}}$) per step, so computationally this costs the same as Explicit Euler. Using Symplectic Euler, we integrate the same orbit as Figure 8.

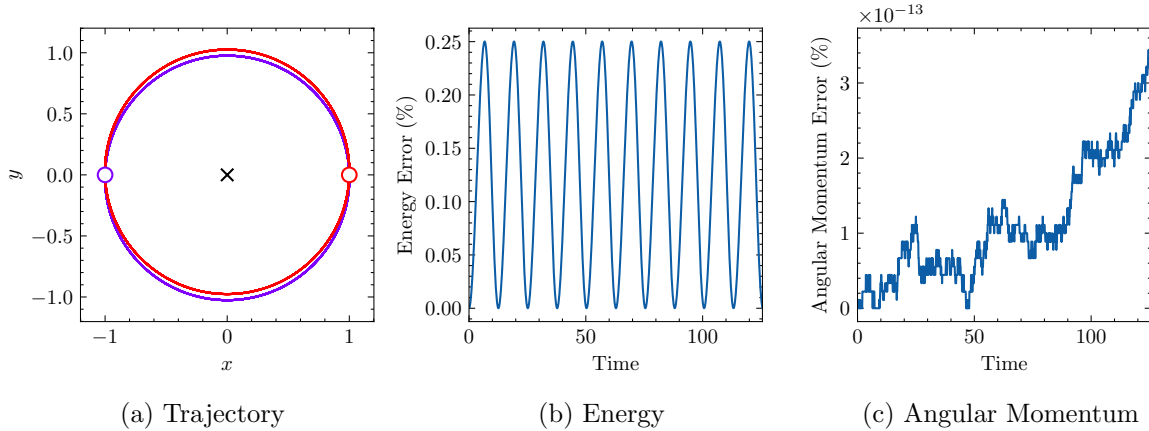


Figure 9: Ten period, Symplectic Euler integration of the two-body equations (2.11) with zero eccentricity and step size $h = 0.1$. Circles indicate initial positions.

Figure 9 shows the difference this simple change makes. The trajectories don't spiral out, the energy error is looks to be small (0.25%) and bounded over this timescale and the angular momentum error is order 10^{-13} , likely due to machine precision error. Clearly Symplectic Euler does a better job than Explicit Euler, but there are still issues. The trajectories don't line up with an error of less than one percent, and such errors seem suspiciously low for a large step size $h = 0.1$ relative to the period (~ 126 steps per period). So is the scheme appropriate, or is it a bad test case? In a circle, the kinetic and potential energies will remain the same throughout, and not just balance each other out. In turn, this test case may not be the best for measuring accuracy, but it does confirm the implementation of the N-body equations (2.4) and the two schemes are likely correct.

In light of this, we pick an elliptical orbit with eccentricity $e = 0.5$ and initial conditions (3.1). It is expected that the bodies move on two identical ellipses about the CM. Once again, integration is done on ten periods with step size $h = 0.1$.

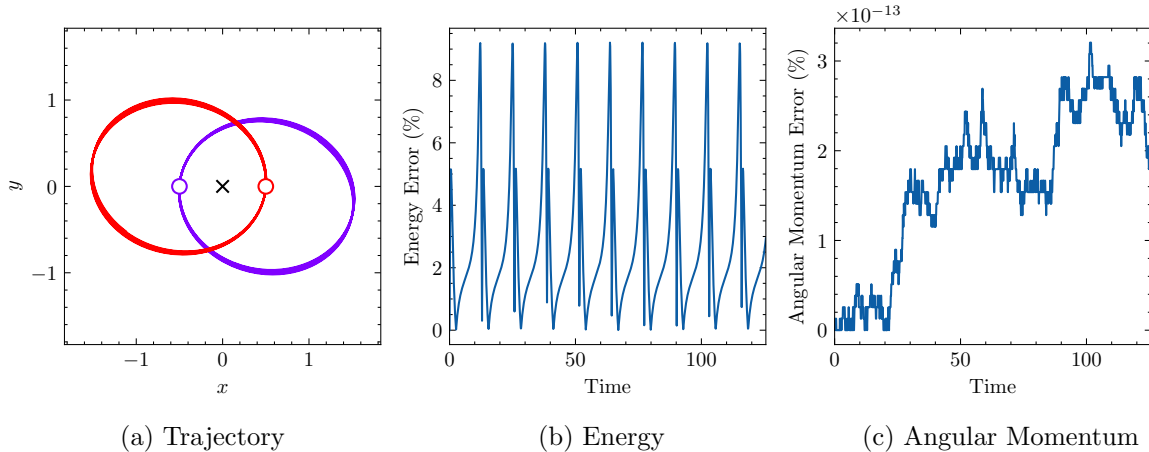


Figure 10: Ten period, Symplectic Euler integration of the two-body equations (2.11) with eccentricity $e = 0.5$ and step size $h = 0.1$.

Figure 10 shows the results of using Symplectic Euler to integrate this ellipse. The angular momentum remains a couple of orders of magnitudes above double precision and the energy is still conserved but with an error 36 times higher than the circular case. For much of this

project we are interested in long term behaviour and errors like this can still be problematic. To illustrate this we integrate 100 periods and keep the step size as $h = 0.1$.

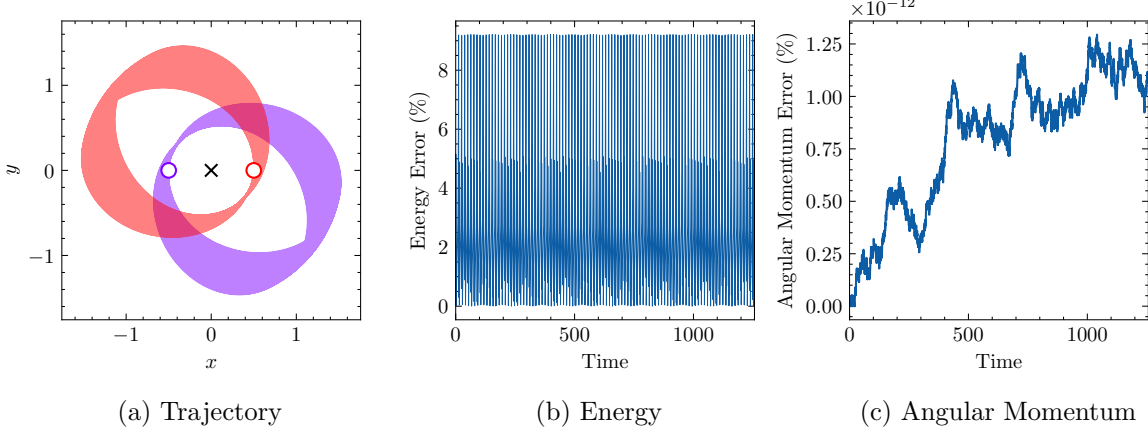


Figure 11: 100 period, Symplectic Euler integration of the two-body equations (2.11) with eccentricity $e = 0.5$ and step size $h = 0.1$.

Figure 11 shows that the energy and angular momentum are conserved, but the ellipses drift clockwise away from the true solution. Decreasing the step size would help but how much do we have to reduce it to make the error? For that we can look to the order of the scheme. A scheme is order p if the error of one interval is proportional to h^{p-1} and when integrated over $n = t_{\max}/h$ steps the scheme gives an error proportional to h^p [4, 1].

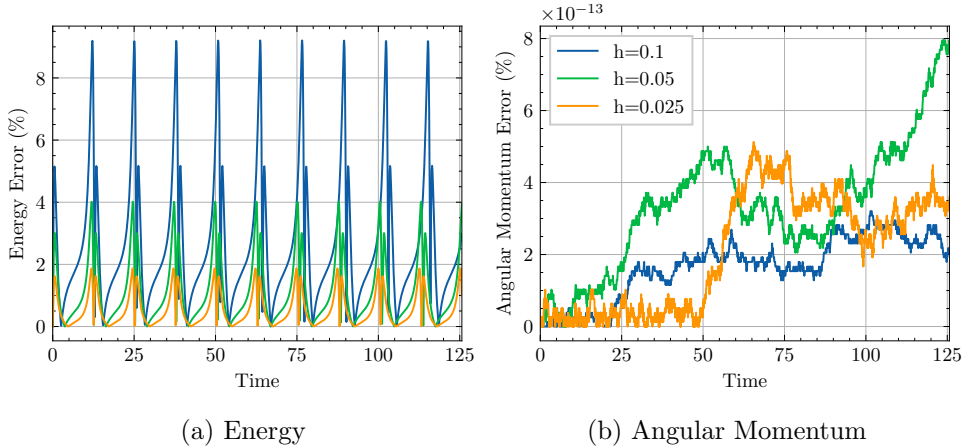


Figure 12: Ten period, Symplectic Euler integration of the two-body equations (2.11) with eccentricity $e = 0.5$ and step sizes $h = 0.1$, $h = 0.05$ and $h = 0.025$.

Repeating the ten period integration of the $e = 0.5$ ellipse with step sizes $h = 0.025$, $h = 0.05$ and $h = 0.1$ gives Figure 12. The angular momentum error is still at machine epsilon but it is easy to read off that halving the step size halves the energy error, confirming that Symplectic Euler is indeed first order. This validates the implementation.

However, halving the step size also doubles the number of steps, doubling the computational time. If we were to pick a small enough step-size then Symplectic Euler would accurately integrate an N-body system but it would take a long time. Consequently, we look to higher order schemes. Higher-order schemes use additional terms in their approximations, which allow them to capture more details of the model. This means that they can provide better approximations, especially when the step size is relatively large.

3.1.3 Leapfrog

The first higher order scheme we consider is Störmer-Verlet, known also as the Störmer method in astronomy, the Verlet method in molecular dynamics or Leapfrog in this context [4, 1]. It is a second order symplectic integrator, so it is expected it to conserve energy and be time-reversible like Symplectic Euler. By the second-order difference quotient, a second order discretisation of the N-body equations (2.4) is

$$(\mathbf{r}_i)_{n+1} - 2(\mathbf{r}_i)_n + (\mathbf{r}_i)_{n-1} = h^2(\dot{\mathbf{r}}_i)_n = h^2(\dot{\mathbf{v}}_i)_n. \quad (3.6)$$

The derivatives $\mathbf{v}_i = \dot{\mathbf{r}}_i$ can be approximated by

$$(\mathbf{v}_i)_n = \frac{(\mathbf{r}_i)_{n+1} - (\mathbf{r}_i)_{n-1}}{2h} \quad \text{and} \quad (\mathbf{v}_i)_{n+1/2} = \frac{(\mathbf{r}_i)_{n+1} - (\mathbf{r}_i)_n}{h}. \quad (3.7)$$

for $i = 1, \dots, N$, which admits a one-step formulation for actual computations: Equation (3.6) can be written as $(\mathbf{v}_i)_{n+1/2} - (\mathbf{v}_i)_{n-1/2} = h(\dot{\mathbf{v}}_i)_n$ and we use $(\mathbf{v}_i)_{n+1/2} - (\mathbf{v}_i)_{n-1/2} = 2(\mathbf{v}_i)_n$ to eliminate $(\mathbf{v}_i)_{n+1/2}$ or $(\mathbf{v}_i)_{n-1/2}$ [4, 1]. This gives the explicit step-formulae

$$\begin{aligned} (\mathbf{v}_i)_{n+1/2} &= (\mathbf{v}_i)_n + \frac{h}{2}(\dot{\mathbf{v}}_i)_n, \\ (\mathbf{r}_i)_{n+1} &= (\mathbf{r}_i)_n + h(\mathbf{v}_i)_{n+1/2}, \\ (\mathbf{v}_i)_{n+1} &= (\mathbf{v}_i)_{n+1/2} + \frac{h}{2}(\dot{\mathbf{v}}_i)_{n+1}, \end{aligned} \quad (3.8)$$

for $i = 1, \dots, N$, known as velocity Verlet. If instead the half step was taken in the position, then it would be known as position Verlet. It might seem unnatural using $(\dot{\mathbf{v}}_i)_{n+1}$ to calculate $(\mathbf{v}_i)_{n+1}$ but this is a force function of the $(\mathbf{r}_i)_{n+1}$ explicitly defined in the previous step. Notice that there are two force calculations $(\dot{\mathbf{v}}_i)_n$ and $(\dot{\mathbf{v}}_i)_{n+1}$ but the second force calculation can be stored and used as the first force calculation in the next step, so really there is only one. Using this to integrate ten periods of the $e = 0.5$ ellipse with a step size $h = 0.1$ gives Figure 13.

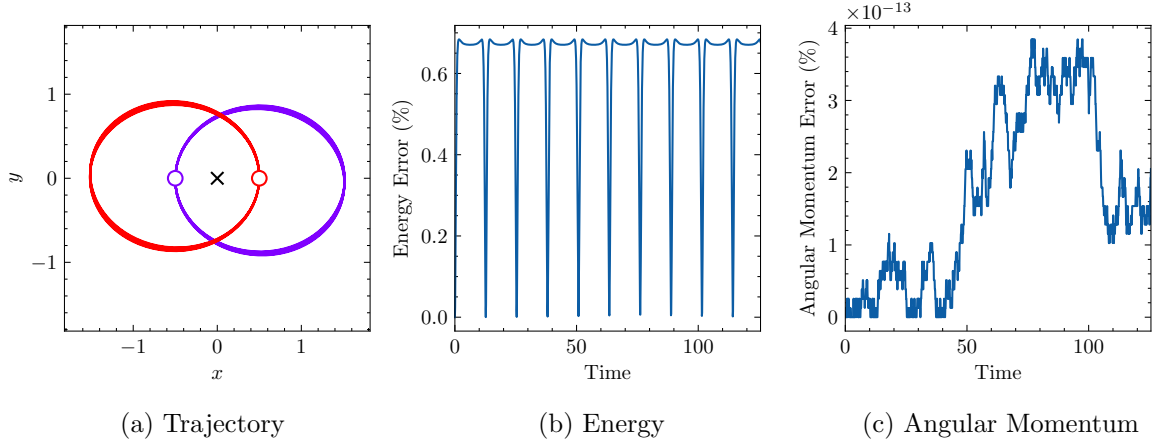


Figure 13: Ten period, Leapfrog integration of the two-body equations (2.11) with eccentricity $e = 0.5$ and step size $h = 0.1$.

It is read off that this scheme is already much better than Symplectic Euler, in fact the energy error is improved by a whole order of magnitude. The angular momentum is once again irrelevant.

Figure 14 shows the results of 100 period integration. They don't seem quite right - the energy error remains much lower (0.7%) but there is a similar amount of clockwise drift to Symplectic Euler. The scheme may be implemented wrong so the same step size test as in Figure 12 is performed.

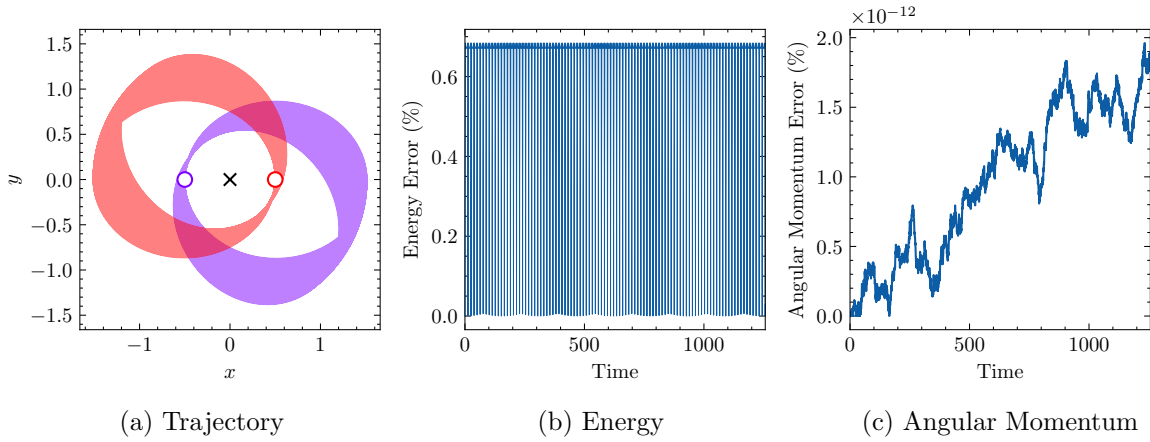


Figure 14: 100 period, Leapfrog integration of the two-body equations (2.11) with eccentricity $e = 0.5$ and step size $h = 0.1$.

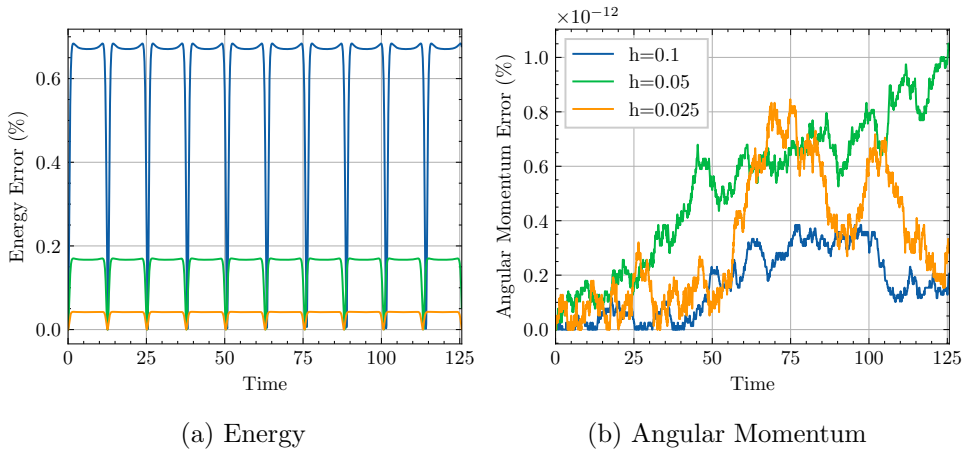


Figure 15: Ten period, Leapfrog integration of the two-body equations (2.11) with eccentricity $e = 0.5$ and step sizes $h = 0.1$, $h = 0.05$ and $h = 0.025$.

Figure 15 shows that halving the step size quarters the error, so the implementation is second order. This coupled with the conservation of energy gives enough evidence to support the implementation is correct. The solution is to either decrease the step size or look to other, higher-order schemes.

3.1.4 Fourth-order Runge-Kutta

The most obvious choice for a higher-order scheme is the classical fourth-order Runge-Kutta method, RK4, defined by the butcher tableau 1 [3]:

	0			
$\frac{1}{2}$		$\frac{1}{2}$		
$\frac{1}{2}$		0	$\frac{1}{2}$	
1	0	0	1	
	$\frac{1}{6}$	$\frac{1}{3}$	$\frac{1}{3}$	$\frac{1}{6}$

Table 1: Butcher Tableau for RK4 [3].

In this context, an explicit representation of one RK4 step is:

$$\begin{aligned}
k_{r1} &= h(\mathbf{v}_i)_n, \\
k_{v1} &= h(\dot{\mathbf{v}}_i)_n, \\
k_{r2} &= h \left[(\mathbf{v}_i)_n + \frac{k_{v1}}{2} \right], \\
k_{v2} &= h \frac{d^2}{dt^2} \left[(\mathbf{r}_i)_n + \frac{k_{r1}}{2} \right], \\
k_{r3} &= h \left[(\mathbf{v}_i)_n + \frac{k_{v2}}{2} \right], \\
k_{v3} &= h \frac{d^2}{dt^2} \left[(\mathbf{r}_i)_n + \frac{k_{r2}}{2} \right], \\
k_{r4} &= h [(\mathbf{v}_i)_n + k_{v3}], \\
k_{v4} &= h \frac{d^2}{dt^2} [(\mathbf{r}_i)_n + k_{r3}], \\
(\mathbf{r}_i)_{n+1} &= (\mathbf{r}_i)_n + \frac{1}{6}(k_{r1} + 2k_{r2} + 2k_{r3} + k_{r4}), \\
(\mathbf{v}_i)_{n+1} &= (\mathbf{v}_i)_n + \frac{1}{6}(k_{v1} + 2k_{v2} + 2k_{v3} + k_{v4}),
\end{aligned} \tag{3.9}$$

for $i = 1, \dots, N$. There are four force calculations per RK4 step, so this scheme is four times as expensive as Leapfrog and Symplectic Euler. Moreover, RK4 is not symplectic, which comes with its obvious disadvantages. We are interested in seeing if the fourth-order accuracy outweighs the drawbacks. As per usual, we integrate the $e = 0.5$ ellipse for ten and 100 periods with step size $h = 0.1$, shown in Figures 16 and 17.

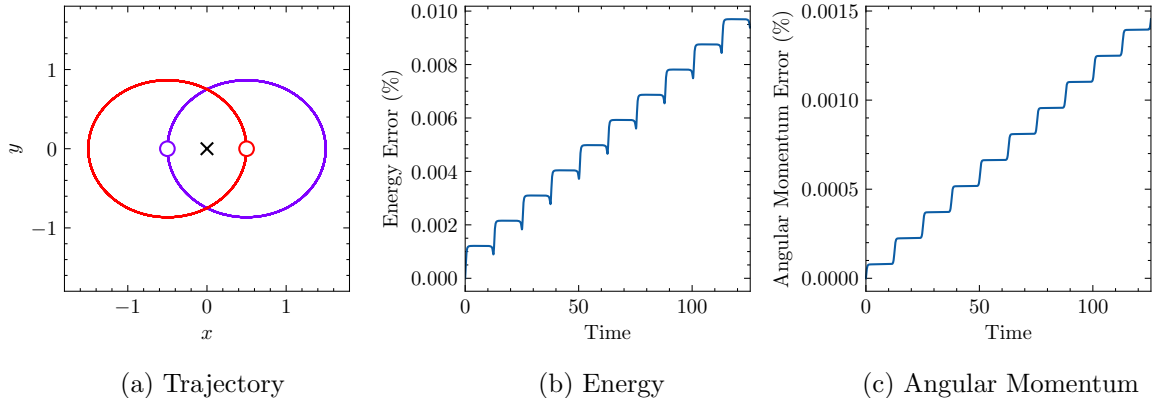


Figure 16: Ten period, RK4 integration of the two-body equations (2.11) with eccentricity $e = 0.5$ and step size $h = 0.1$.

There are a few interesting things to comment on here. Firstly, the energy is not conserved but it is small. Extrapolating the maximum error implies it would take ~ 700 periods to reach the same maximum error as Leapfrog. The energy and angular momentum error steps up every period, signifying that when the bodies are close error is introduced. This is an important factor when expecting bodies to come very close e.g. with hyperbolic orbits.

The angular momentum is not at machine precision any more but energy is still the dominating error. There is no obvious drift in the trajectories, likely due to the low error. The evidence suggests that even though RK4 is computationally more expensive and not energy conserving, it may be the preferred scheme for shorter time-scales.

Implementing a higher order or different Runge-Kutta method may improve accuracy, but RK4 seems to be sufficient, and it would not help the symplectic issue. Instead, what is really needed is a fourth or higher-order symplectic scheme.

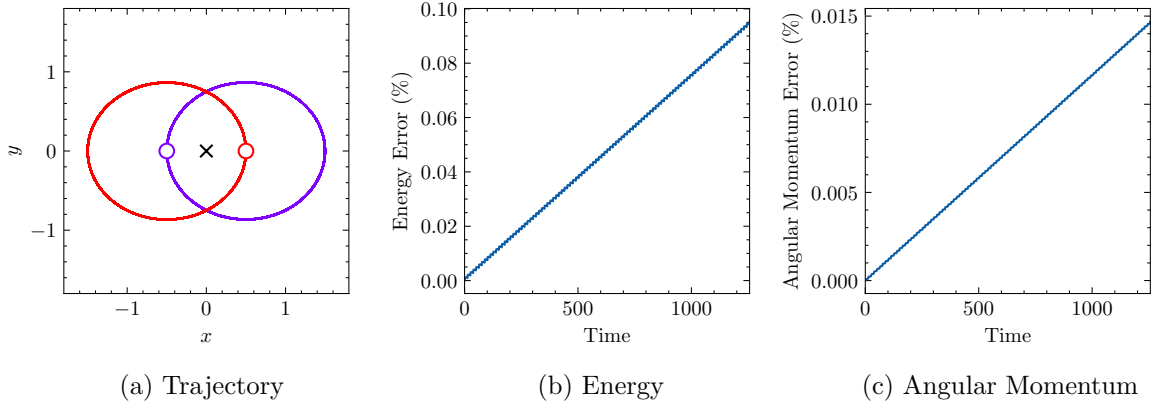


Figure 17: 100 period, RK4 integration of the two-body equations (2.11) with eccentricity $e = 0.5$ and step size $h = 0.1$.

3.1.5 Forest-Ruth

Thanks to the work of E. Forest and R.D. Ruth [8] such higher order symplectic schemes do exist. One step of the standard Forest-Ruth (FR) scheme [8] is defined:

$$\begin{aligned}
 (\mathbf{r}_i)_n^1 &= (\mathbf{r}_i)_n + \theta \frac{h}{2} (\mathbf{v}_i)_n, \\
 (\mathbf{v}_i)_n^1 &= (\mathbf{v}_i)_n + \theta h (\dot{\mathbf{v}}_i)_n^1, \\
 (\mathbf{r}_i)_n^2 &= (\mathbf{r}_i)_n^1 + (1 - \theta) \frac{h}{2} (\mathbf{v}_i)_n^1, \\
 (\mathbf{v}_i)_n^2 &= (\mathbf{v}_i)_n^1 + (1 - 2\theta) h (\dot{\mathbf{v}}_i)_n^2, \\
 (\mathbf{r}_i)_n^3 &= (\mathbf{r}_i)_n^2 + (1 - \theta) \frac{h}{2} (\mathbf{v}_i)_n^2, \\
 (\mathbf{v}_i)_{n+1} &= (\mathbf{r}_i)_n^3 + \theta h (\dot{\mathbf{v}}_i)_n^3, \\
 (\mathbf{r}_i)_{n+1} &= (\mathbf{r}_i)_n^3 + \theta \frac{h}{2} (\mathbf{v}_i)_{n+1},
 \end{aligned} \tag{3.10}$$

where

$$\theta = \frac{1}{2 - \sqrt[3]{2}} \simeq 1.35120719195966$$

and $i = 1, \dots, N$. Superscript distinguishes between different values of velocity and position.

This method requires three force calculations ($\dot{\mathbf{v}}_i{}_n^1$, $\dot{\mathbf{v}}_i{}_n^2$ and $\dot{\mathbf{v}}_i{}_n^3$), so is computationally less expensive than RK4 but more than Leapfrog. Note also that the equations are symmetric about the middle equation, ensuring time-reversible invariance. The value of θ is picked to ensure that the scheme is fourth-order when integrated over T/h steps.

The usual test is performed - ten periods of the $e = 0.5$ ellipse with $h = 0.1$. Figure 18 shows an unexpected result: the scheme massively jumps in energy error, and the bodies fly away from each other. With behaviour like this it is harder to test the order of the scheme, but there must be a reason for the error. Looking closely at the FR algorithm (3.10), we see the middle step has coefficient $1 - 2\theta \simeq -1.7024$, stepping back in time by a large magnitude. This is likely where the error is coming from, so we address it.

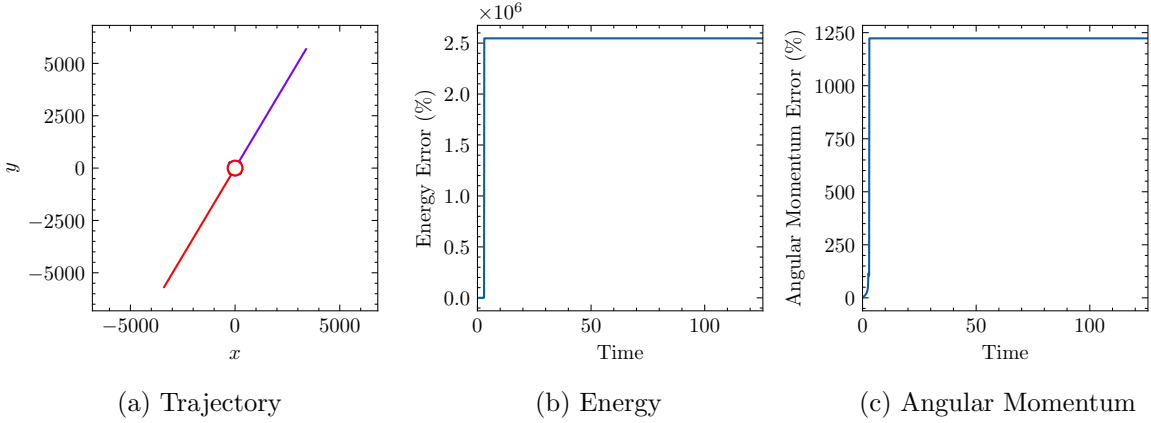


Figure 18: Ten period, Forest-Ruth integration of the two-body equations (2.11) with eccentricity $e = 0.5$ and step size $h = 0.1$.

One can avoid stepping back in time more than magnitude h by using the “Position Extended Forest-Ruth Like” (PEFRL) scheme introduced by Omelyan et al. [25, 33]:

$$\begin{aligned}
 (\mathbf{r}_i)_n^1 &= (\mathbf{r}_i)_n + \xi h(\mathbf{v}_i)_n, \\
 (\mathbf{v}_i)_n^1 &= (\mathbf{v}_i)_n + (1 - 2\eta) \frac{h}{2} (\dot{\mathbf{v}}_i)_n^1, \\
 (\mathbf{r}_i)_n^2 &= (\mathbf{r}_i)_n^1 + \chi h(\mathbf{v}_i)_n^1, \\
 (\mathbf{v}_i)_n^2 &= (\mathbf{v}_i)_n^1 + \eta h(\dot{\mathbf{v}}_i)_n^2, \\
 (\mathbf{r}_i)_n^3 &= (\mathbf{r}_i)_n^2 + (1 - 2(\chi + \xi)) h(\mathbf{v}_i)_n^2, \\
 (\mathbf{v}_i)_n^3 &= (\mathbf{v}_i)_n^2 + \eta h(\dot{\mathbf{v}}_i)_n^3, \\
 (\mathbf{r}_i)_n^4 &= (\mathbf{r}_i)_n^3 + \chi h(\mathbf{v}_i)_n^3, \\
 (\mathbf{v}_i)_{n+1} &= (\mathbf{v}_i)_n^3 + (1 - 2\eta) \frac{h}{2} (\dot{\mathbf{v}}_i)_n^4, \\
 (\mathbf{r}_i)_{n+1} &= (\mathbf{r}_i)_n^4 + \xi h(\mathbf{v}_i)_{n+1},
 \end{aligned} \tag{3.11}$$

where

$$\begin{aligned}
 \xi &= +0.1786178958448091E + 00, \\
 \eta &= -0.2123418310626054E + 00, \\
 \chi &= -0.6626458266981849E - 01.
 \end{aligned} \tag{3.12}$$

This modification does four force calculations rather than three but removes the large time step so should be more accurate. Note also that it is still symmetric, so is time-reversible.

Repeating the integration gives Figure 19 where the problem seems to be fixed, in fact the scheme performs the best out of any scheme seen so far. The energy error is conserved and much lower than RK4 and Leapfrog. The angular momentum is at machine precision. The long term behaviour of PEFRL is shown in Figure 20. Nothing unexpected occurs, there is no drift and the error remains very low.

Taking these results into consideration, it seems unnecessary to carry out the extra work needed to check if the original FR implementation is wrong or if it is just inappropriate for this problem. P.Young [33] suggests that PEFRL is about 26 times more accurate than FR for the same step size anyway.

From now on the only Forest-Ruth scheme we consider is PEFRL. Moreover, Omelyan [25] suggests that symplectic integrators of order higher than four are probably not worth the extra complexity. With this in mind, we can stop our search for possible schemes and perform a more in-depth comparison.

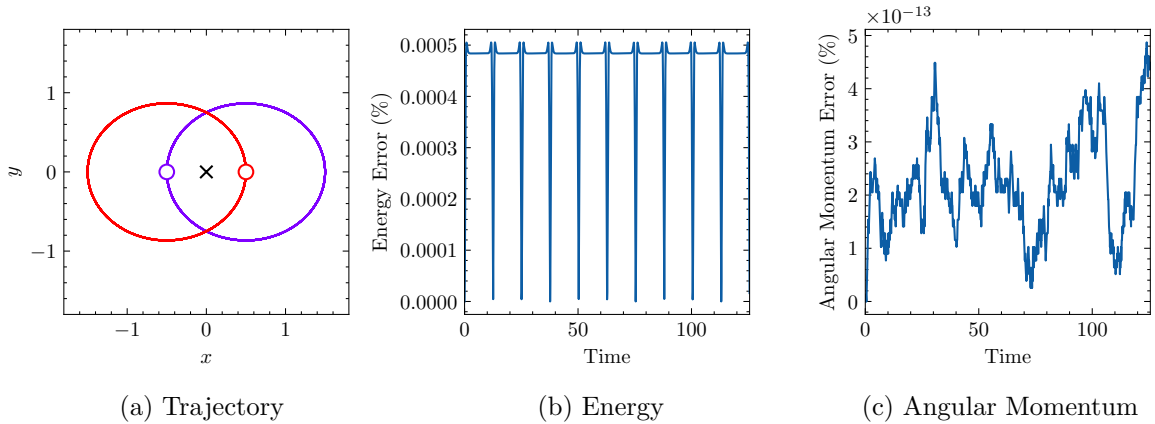


Figure 19: Ten period, PEFRL integration of the two-body equations (2.11) with eccentricity $e = 0.5$ and step size $h = 0.1$.

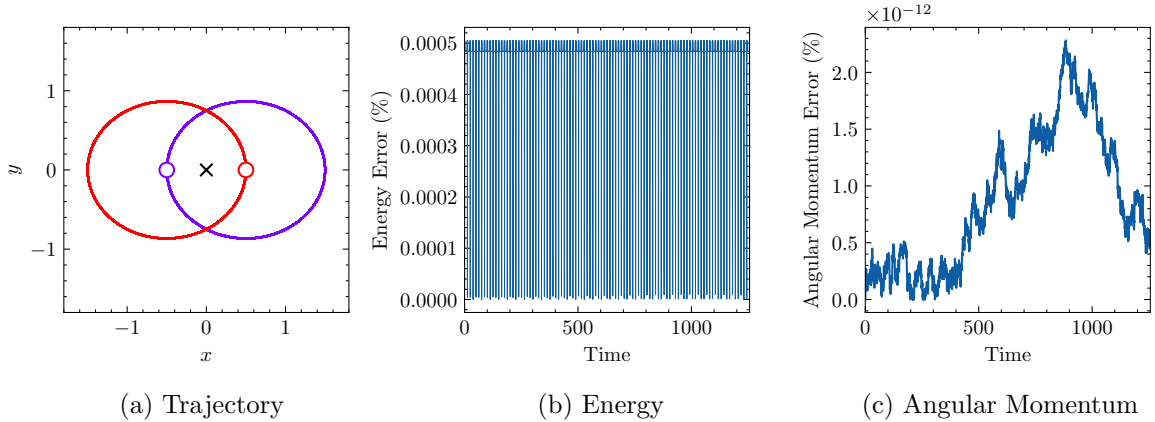


Figure 20: 100 period, PEFRL integration of the two-body equations (2.11) with eccentricity $e = 0.5$ and step size $h = 0.1$.

3.2 Scheme Comparison

There are still questions to be answered about which scheme to use. Evidence points towards using PEFRL, but Leapfrog or RK4 could still be sufficient. To answer relevant questions, this subsection addresses the schemes covered in Section 3.1 and compares each via a selection of comparisons.

3.2.1 Scheme order

The first thing to check is that the schemes are the order they say they are. This will give us good confidence they have all been implemented correctly. The step size is varied and maximum energy error over ten periods ($10T/h$ steps) of the ellipse $e = 0.5$ measured. The step size is varied relative to the period, from $h/T = 0.005/4\pi$ to $h/T = 0.1/4\pi$. It has been shown angular momentum would not provide a good indicator here, as it typically remains at double precision.

Figure 21 shows the results of such a test. Plotting on a log-log scale and measuring the gradient gives the exponent and thus the estimated order of the scheme. The gradients are summarised in table 2. By section 3.1 it is known that Symplectic Euler and Leapfrog are first and second order respectively, but table 2 confirms it.

Scheme	Explicit Euler	Symplectic Euler	Leapfrog	RK4	PEFRL
Order	0.18913	1.19839	2.00732	4.89481	4.00358

Table 2: Estimated order of schemes

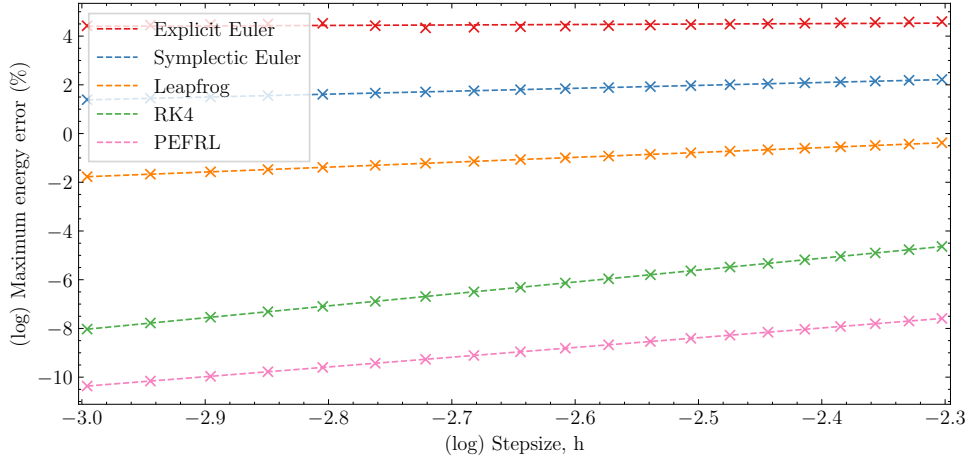


Figure 21: Relationship between maximum energy error and step size

In addition, PEFRL is indeed fourth order, but Explicit Euler and RK4 are harder to interpret. Explicit Euler is definitely at most first order and RK4 is at least fourth order, in fact RK4 is almost fifth order. Difficulties are likely because both are non-symplectic, so the overall error is harder to measure accurately. The order comparison tells us that to improve accuracy we would have to drop the step size of PEFRL much less than Leapfrog (keeping in mind that PEFRL does four force calculations compared to the one of Leapfrog). From now on we remove Explicit Euler as it offers no benefits over the other first order scheme, Symplectic Euler. Symplectic Euler is kept as a reference first order scheme.

3.2.2 Energy and Angular Momentum

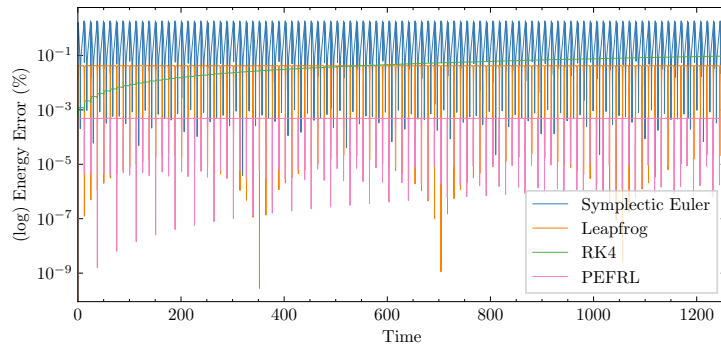
Throughout Section 3.1 schemes are integrated and compared using the same step size. However, the fourth order schemes have four times as many force calculations as the lower order schemes, so it isn't fair to compare them directly with the same step size. Instead, we re-integrate 100 periods with step size proportional to the work done. For the remaining comparisons, a step-size of $h = 0.1$ is used in PEFRL and RK4. Leapfrog and Symplectic Euler use $h = 0.025$. Furthermore, integration is done on the $e = 0.5$ and $e = 0.8$ ellipses to gain a wider view of performance. The $e = 0.8$ ellipse gives a better idea of what happens when the bodies come closer to each other.

Figure 22 shows the energy comparison. In the case of $e = 0.5$ PEFRL is the best scheme, followed by Leapfrog, RK4 and then Symplectic Euler. However, over a long enough timescale we would expect RK4 to become worse than Symplectic Euler. The results of this can be seen in figures 22b & 24c where RK4 rapidly increases in energy until the bodies become hyperbolic. Of course the step size could be decreased but PEFRL works better for the same cost. This highlights the importance of using a symplectic scheme for N-body dynamics.

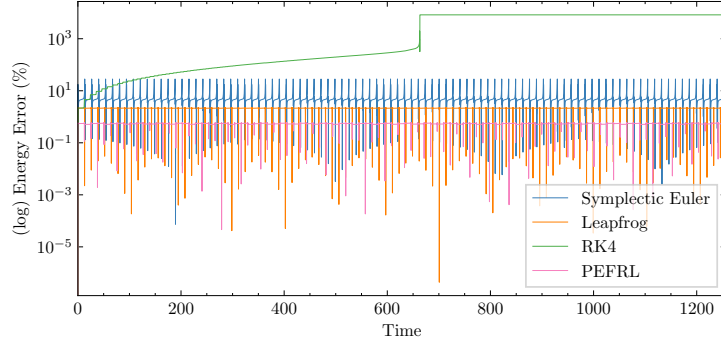
Notice that the energies in figure 22b are at orders of magnitudes higher than figure 22a, implying that the closer the masses come to each other, the greater the errors. Consequently, to calculate a hyperbolic orbit correctly, a much smaller step size will be needed.

Figure 23 shows the comparison of angular momentum. It doesn't tell us much, other than RK4 is the only scheme not to conserve angular momentum, as expected. For the remaining three schemes, the angular momentum sits at double precision, so a comparison can't be made.

A conclusion can be made that RK4 really shouldn't be used when there is access to symplectic schemes. Moreover, PEFRL is better than Symplectic Euler and Leapfrog, but the latter is still accurate so would still be appropriate for our problem. Section 3.2.1 says that this comparison should hold true as we decreased the step size.

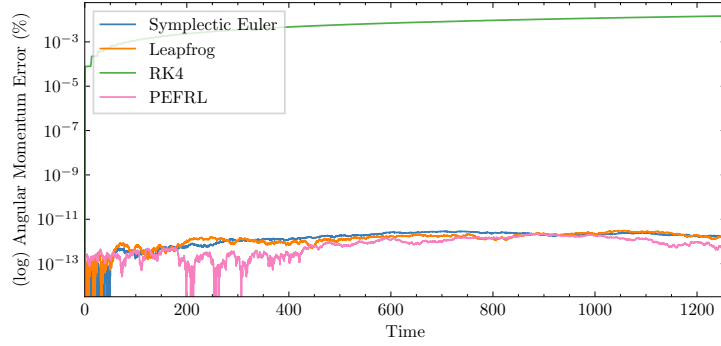


(a) $e = 0.5$

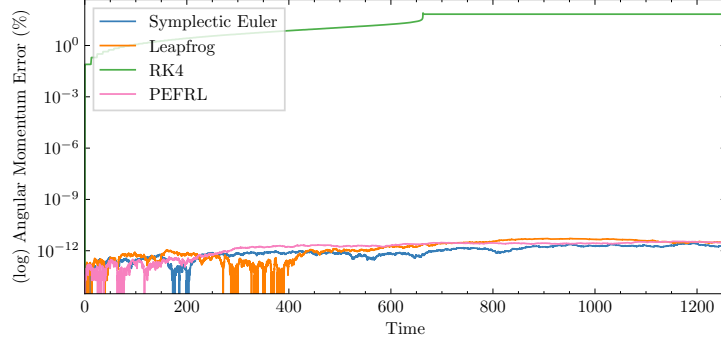


(b) $e = 0.8$

Figure 22: Energy comparison with scheme integration of 100 periods of the $e = 0.5$ and $e = 0.8$ ellipses.



(a) $e = 0.5$



(b) $e = 0.8$

Figure 23: Angular momentum comparison with scheme integration of 100 periods of the $e = 0.5$ and $e = 0.8$ ellipses.

3.2.3 Global Error

Recall the clockwise drift of Leapfrog in figure 14. This drift is not captured by the energy error as the bodies are moving in the correct orbit but being continually rotated. However, it is still valuable to compare schemes by this metric. In other words, we want to measure the global error by using analytical equation (2.18).

Integration is done on 100 periods using the step sizes mentioned in section 3.2.2. Equation (2.18) concerns the motion of one mass orbiting the other, so integrated trajectories are converted to the m_2 reference frame. Integration of the exact equation (2.18) is done using the SciPy [30] Python package and compared to the numerical scheme to give the absolute error at each time-step. To make sense of the absolute error, it should be measured relative to the size of the orbit. The error is divided by the size (a) of the ellipse and expressed as a percentage.

Figure 24 shows the drift of the $e = 0.8$. Interestingly, all the symplectic integrators drift clockwise. Symplectic Euler drifts the most, then Leapfrog and PEFRL. In RK4, m_1 spirals toward m_2 before turning hyperbolic and flying away, making more sense of the RK4 behaviour seen in figure 22b.

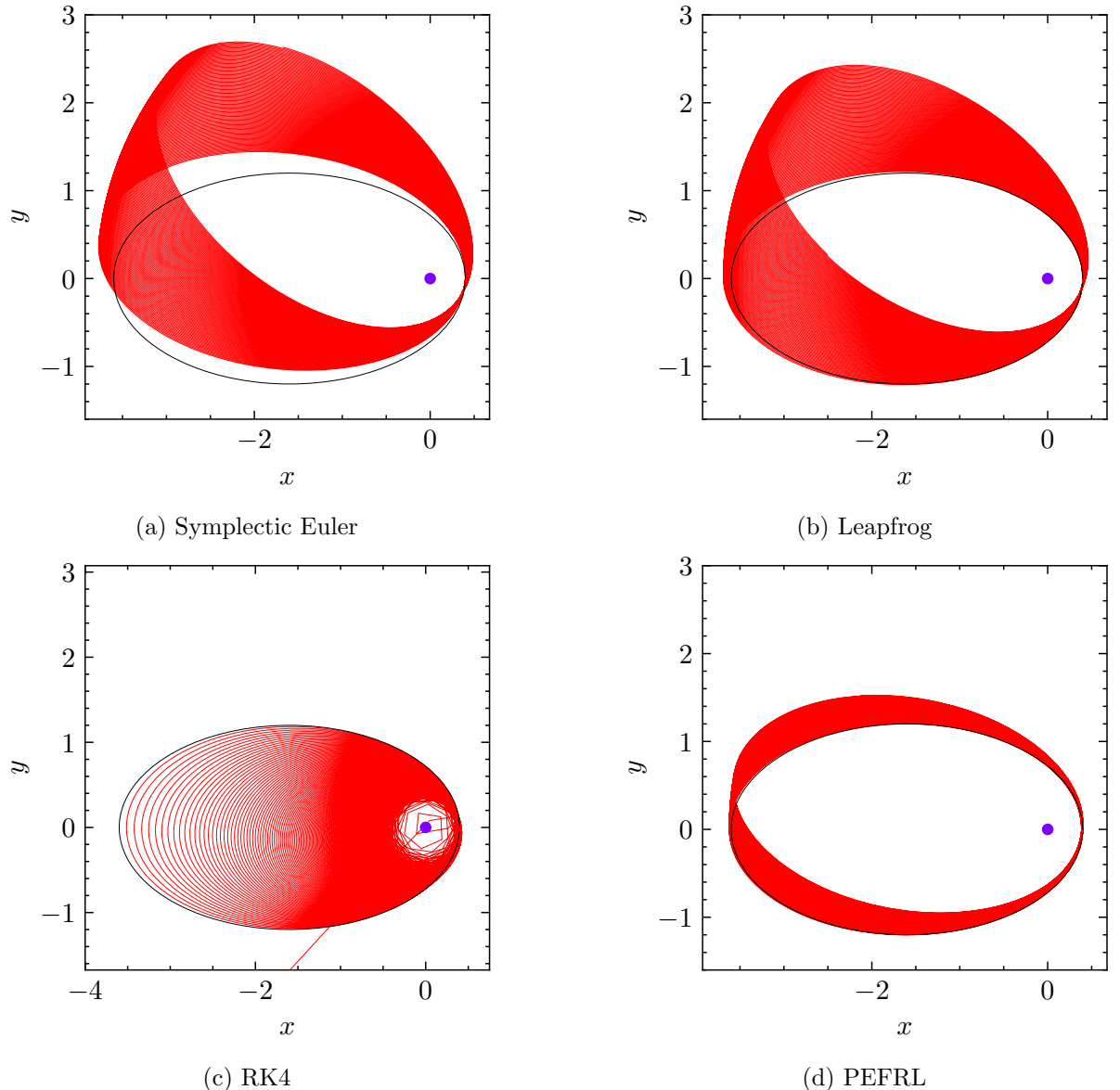
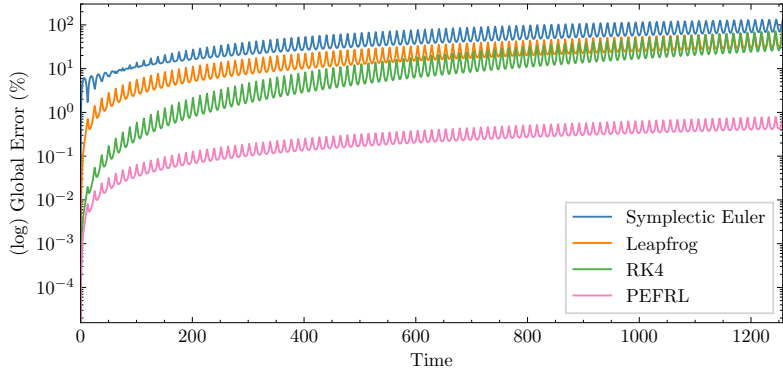
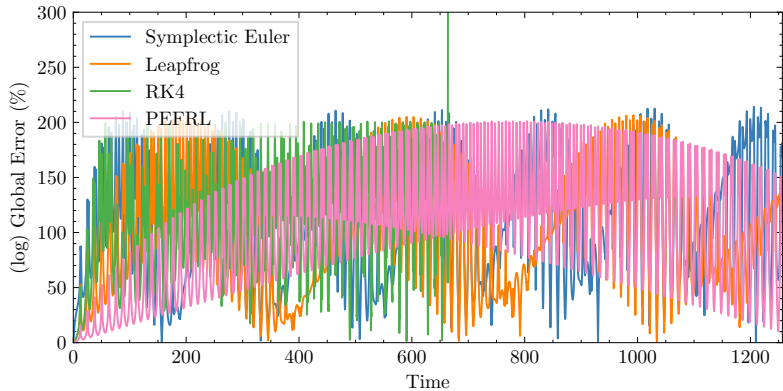


Figure 24: Scheme integration of m_1 orbiting m_2 on the $e = 0.8$ ellipse, over 100 periods. The exact solution is given by the black ellipse.



(a) $e = 0.5$



(b) $e = 0.8$

Figure 25: Global error comparison with scheme integration of 100 periods of the $e = 0.5$ and $e = 0.8$ ellipses.

In figure 25a PEFRL massively out-performs the other schemes, and Leapfrog actually has a similar global error to Symplectic Euler. Something unexpected happens in figure 25b: the global error of the symplectic schemes max out at about 200%. It gives rise to suspicion that this method is implemented wrong or is inappropriate, but the RK4 behaviour does agree with that seen in figure 24. Maybe if the $e = 0.5$ ellipse is integrated for much longer it would give a similar result, but this would need testing.

Once again, the importance of being accurate when the bodies are close is highlighted. It also tells us that Leapfrog does not keep up with PEFRL in this scenario.

3.2.4 Time Reversibility

An important part of Newton's N-body equations (2.4) is they are invariant under time-reversal. In section 3.1 the focus of symplectic has meant the conservation of energy and angular momentum but symplectic also regards time-reversal invariance [33]. What this means is as follows: Suppose we integrate the initial conditions from $(\mathbf{r}_i)_0, (\mathbf{v}_i)_0$ at time t_0 to $(\mathbf{r}_i)_n, (\mathbf{v}_i)_n$ at time t_n . If we were to also integrate the backwards motion starting from $(\mathbf{r}_i)_n$ with opposite velocity $(\mathbf{v}_i)_n$ for time t_0 to t_n , we should land exactly where we started, at $(\mathbf{r}_i)_0$.

An interesting test to conduct would be to integrate forward in time, then integrate backward in time and progressively measure the distance of one of the particles is from where it was on its forward integration. This error should be relative to the size of the orbit, so it is defined as:

$$\text{Distance Error}(t) = \frac{|\mathbf{r}_1^{\text{forward}}(t_n - t) - \mathbf{r}_1^{\text{backward}}(t)|}{a} \quad \text{for } 0 \leq t \leq t_n. \quad (3.13)$$

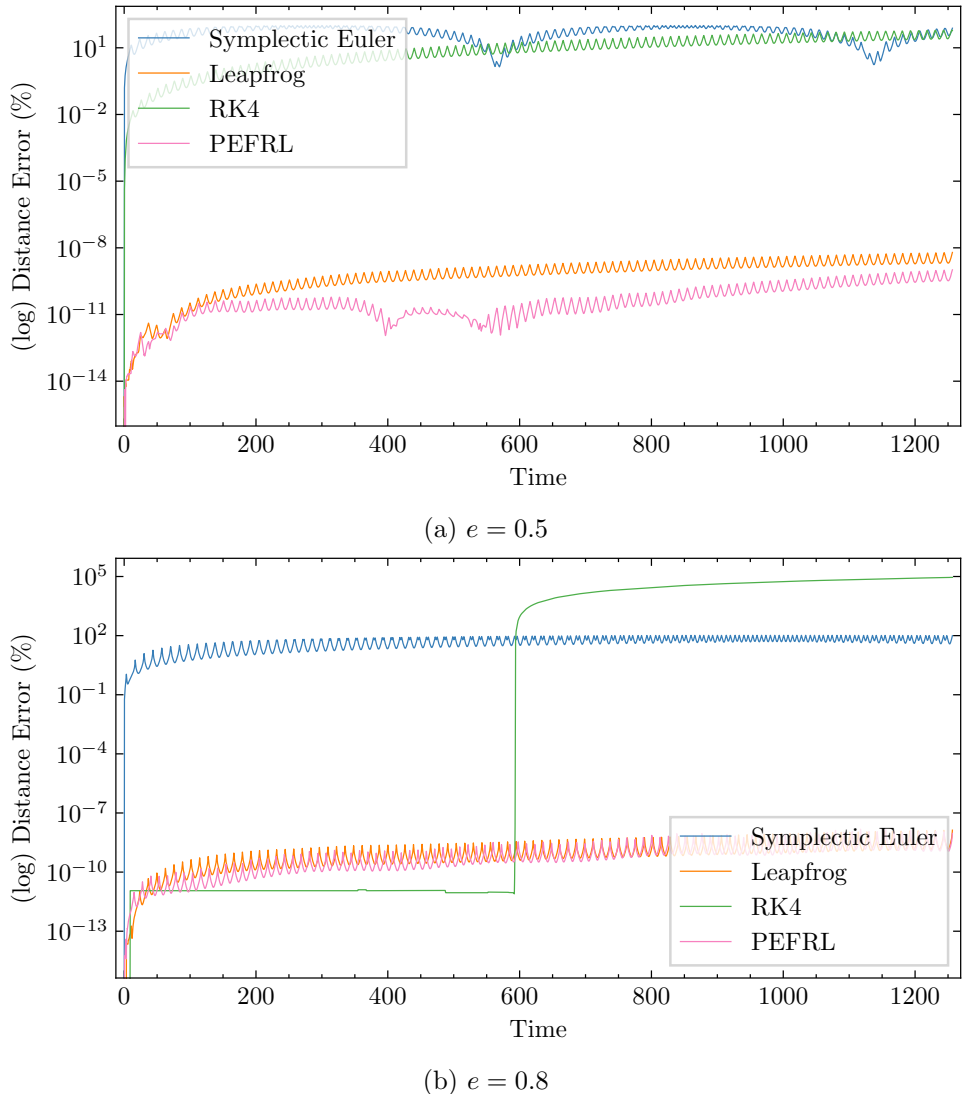


Figure 26: Time invariance comparison for scheme integration of 100 periods of the $e = 0.5$ and $e = 0.8$ ellipses.

Once again, we integrate 100 orbits with the comparable step sizes. Figure 26 shows that PEFRL and Leapfrog perform the best under time-invariance. This is to be expected as they are the higher order symplectic schemes. Importantly, there isn't much between the two schemes, and either could be considered good here. Furthermore, the behaviour of RK4 in figure 26b agrees with that discussed in previous sections. Since we are starting the backward integration of the RK4 integration from far away, it seems unlikely that it would be accurate all the way back to the beginning.

3.2.5 Results

A summary of all the results covered in this section is presented in table 3. PEFRL performed the best across all tests and will be the scheme used moving forward. RK4 highlights the importance of using a symplectic scheme for this problem. Even though RK4 is fourth order, it was consistently out-performed by the lower-order schemes.

On the other hand, Leapfrog could still have a use when computational speed is preferred over high-accuracy. Leapfrog is still accurate but only does one force calculation per step rather than the four of PEFRL. Lastly, it is seen that the energy error is the better indicator of accuracy over the angular momentum, which is generally at double precision.

	Ellipse	S.Euler	Leapfrog	RK4	PEFRL
Order	$e = 0.5$	1.19839	2.00732	4.89481	4.00358
Energy Error (%)	$e = 0.5$	1.8713×10^1	4.2481×10^{-2}	9.5364×10^{-2}	5.0544×10^{-4}
	$e = 0.8$	2.8402×10^1	2.2571×10^0	8.2822×10^3	6.0590×10^{-1}
AM Error (%)	$e = 0.5$	2.8972×10^{-12}	3.1282×10^{-12}	1.4697×10^{-2}	2.2819×10^{-12}
	$e = 0.8$	2.7570×10^{-12}	5.2551×10^{-12}	7.9741×10^1	3.6267×10^{-12}
Global Error (%)	$e = 0.5$	1.3209×10^2	6.5924×10^1	7.3293×10^1	7.9778×10^{-1}
	$e = 0.8$	2.1413×10^2	2.0650×10^2	2.6841×10^5	2.0101×10^2
Time Invariance (%)	$e = 0.5$	1.0179×10^2	6.2114×10^{-9}	6.2647×10^1	1.0213×10^{-9}
	$e = 0.8$	1.0480×10^2	1.3433×10^{-8}	9.0304×10^4	1.5068×10^{-8}

Table 3: Summary of scheme comparison. Error is the maximum over 100 periods.

3.3 Time-adaptive Integration

As hinted at in the previous section, when the bodies come close together (relative to their speed) more error is introduced. This can be investigated further by looking at the behaviour of a hyperbolic orbit with initial conditions

$$\begin{cases} \mathbf{r}_1(0) = [-1, 0, 0]^T, & \mathbf{r}_2(0) = [1, 0, 0]^T, \\ \mathbf{v}_1(0) = [1, -0.5, 0]^T, & \mathbf{v}_2(0) = [-1, 0.5, 0]^T, \end{cases} \quad (3.14)$$

where $E_0 = 0.75$, $L_0 = 1.0$ and $e = 2$. Figure 27 shows such an integration for a short time period. The energy error spikes when the bodies are at their closest and then levels out. This behaviour is also evidenced in the ellipses: Recall in figure 16 the error steps up every period, when the bodies are close.

Integration could be done accurately at all time, thus keeping the error small, but this is very inefficient when the bodies are not close. Instead, we would like to increase the accuracy when the bodies are close and decrease when further away (while still being accurate enough). The step size should be dependent on whether the error will be large or not. Being able to get away with larger step sizes when applicable will speed up computations.

This section addresses the topic by looking at a position-velocity approach to picking a step size, and a predictive local truncation error method.

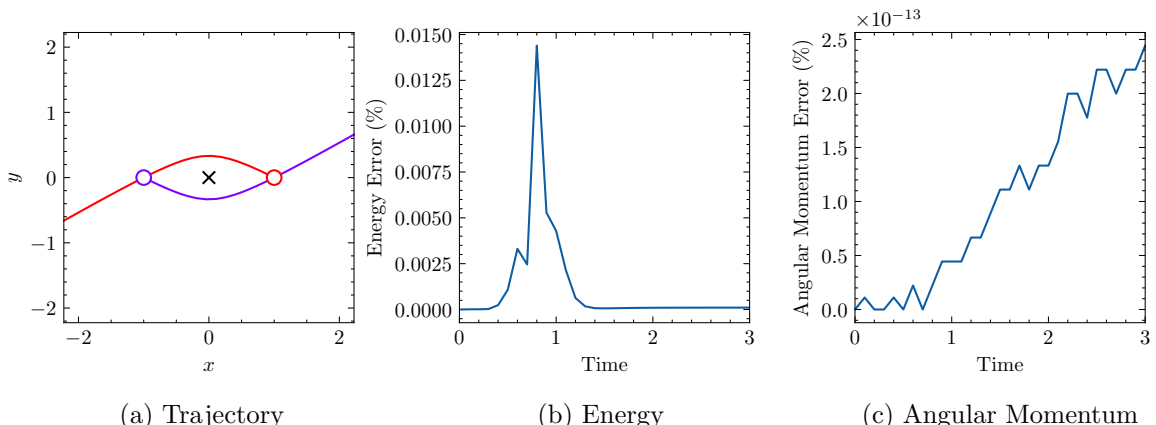


Figure 27: Integration of a hyperbolic orbit using PEFRL and step size $h = 0.1$.

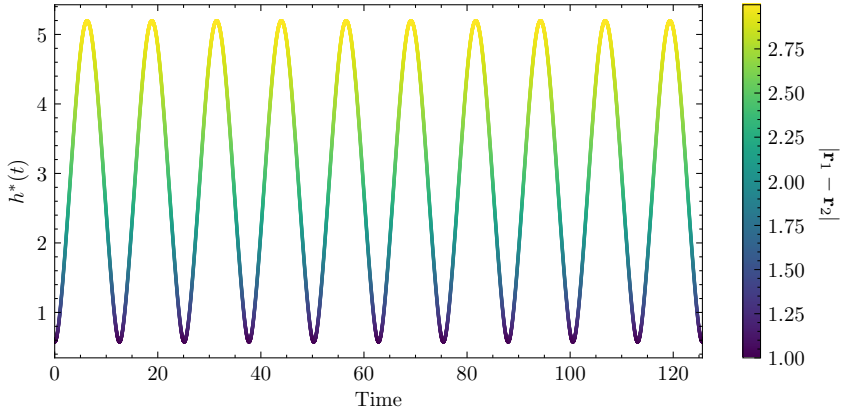


Figure 28: Proposed two-body step size over ten periods of the $e = 0.5$ ellipse. Colour indicates the distance between the bodies.

3.3.1 Position-velocity dependence

Evidence suggests that we would like to pick a step size function that decreases as the distance between bodies decreases and the velocity between bodies increases. In the two-body case, the following step size is proposed:

$$h^*(t) = \frac{|\mathbf{r}_1 - \mathbf{r}_2|}{|\mathbf{v}_1 - \mathbf{v}_2|}. \quad (3.15)$$

Figure 28 shows how this proposed step size changes over an integration of ten periods of the $e = 0.5$ ellipse. It is clear that the step size is at its lowest when the bodies are the closest, and the opposite is true. Furthermore, it can be read off that the minimum value is about 0.5 and the max is 5, implying the step size needs scaling down to something more appropriate.

For N-bodies a small step size is needed whenever any two bodies are close, so we generalise equation (3.15) to

$$h^*(\mathbf{r}_i, \mathbf{v}_i) = h^*(t) = C \min \frac{|\mathbf{r}_i - \mathbf{r}_j|}{|\mathbf{v}_i - \mathbf{v}_j|} \quad \text{for } i = 1, \dots, N \quad \text{and } j = i + 1, \dots, N. \quad (3.16)$$

Before each step of the integration a new h^* is found, based on the previous step's positions and velocities. Notice that $j > i$, ensuring we are not calculating any pairwise step size twice. Moreover, h^* is a unit of time.

The exact value of C will depend on the problem in hand. Generally speaking, an error of 1% or less is desirable. In the case of ten periods of the $e = 0.5$ ellipse, trial and error suggests $C = 0.16$ and $C = 0.55$ gives a maximum energy error of 1% for Leapfrog and PEFRL respectively. We can integrate 10 and 500 periods to see the effects of the new step size.

From figure 29 it is obvious that this new step size method makes the schemes non-symplectic. Interestingly, the energy error levels out at $t = 4000$ and the step sizes converge. Moreover, initially Leapfrog is even better than PEFRL, but this changes after about 100 orbits. This new time-adaption makes the schemes non-symplectic because the integration is no longer exactly time-reversible.

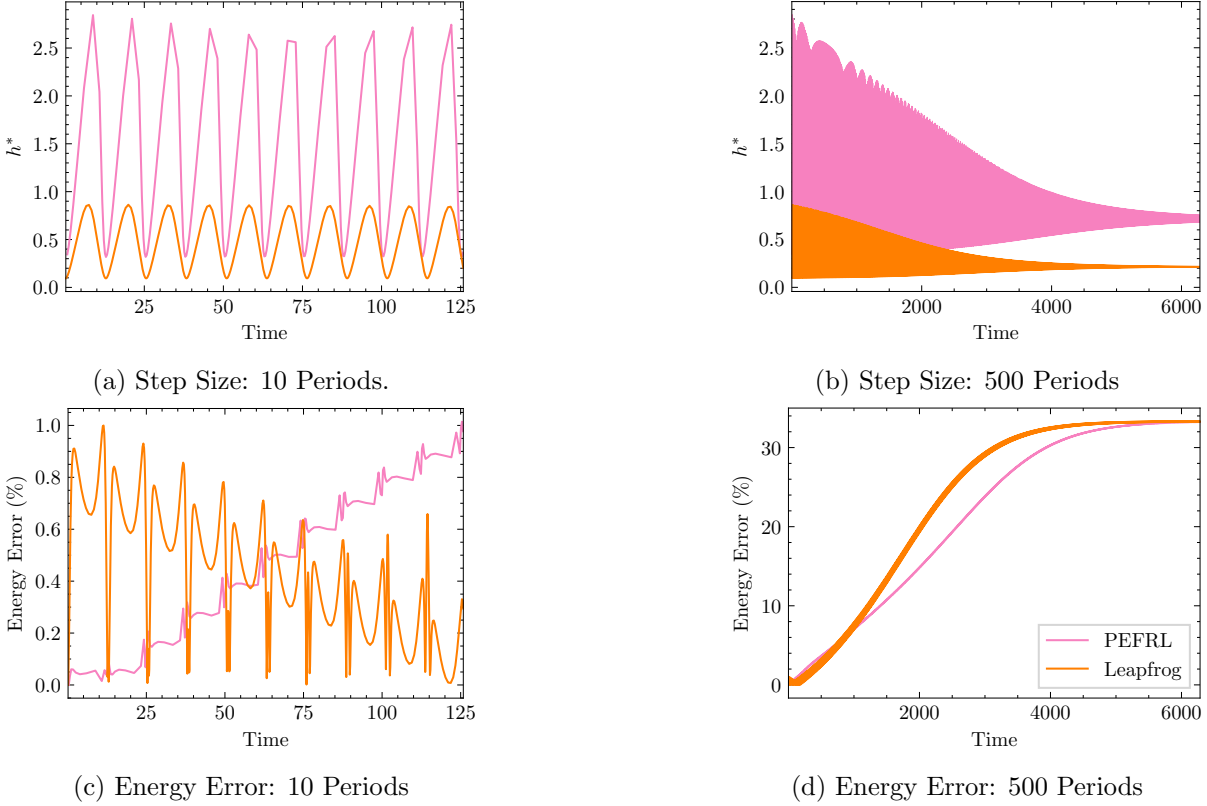


Figure 29: Time-adaptive non-symplectic integration of the $e = 0.5$ ellipse with Leapfrog ($C = 0.16$) and PEFRL ($C = 0.55$).

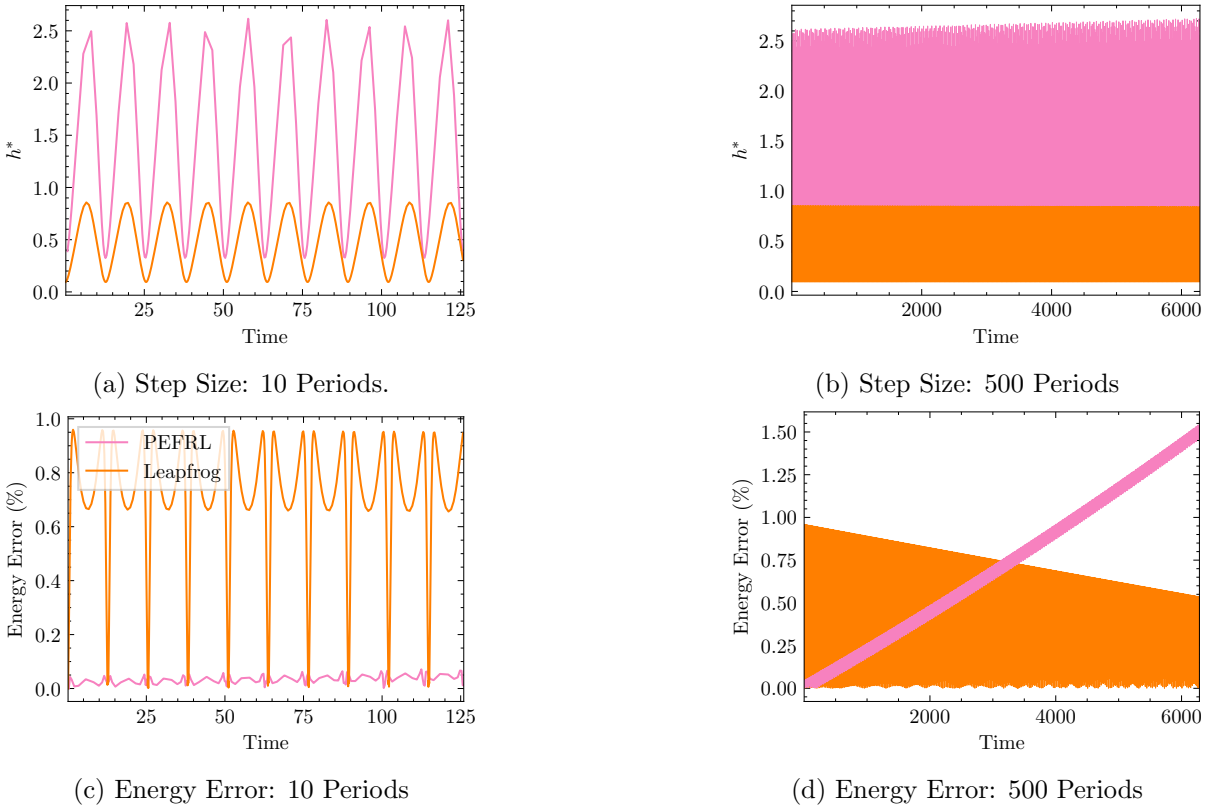


Figure 30: Time-adaptive near-symplectic integration of the $e = 0.5$ ellipse with Leapfrog ($C = 0.16$) and PEFRL ($C = 0.55$).

To fix the time-reversibility issue, each step is changed to

$$\begin{aligned}
h &= h^*((\mathbf{r}_i)_n, (\mathbf{v}_i)_n) \\
\bar{\mathbf{r}}_i, \bar{\mathbf{v}}_i, &= PEFRLStep((\mathbf{r}_i)_n, (\mathbf{v}_i)_n, h), \\
\bar{h} &= h^*(\bar{\mathbf{r}}_i, \bar{\mathbf{v}}_i), \\
h_{\text{new}} &= \frac{h_{\text{old}} + \bar{h}}{2}, \\
(\mathbf{r}_i)_{n+1}, (\mathbf{v}_i)_{n+1} &= PEFRLStep((\mathbf{r}_i)_n, (\mathbf{v}_i)_n, h_{\text{new}}).
\end{aligned} \tag{3.17}$$

This should do a much better job of preserving time-reversible invariance by not overstepping. Figure 30 shows the results of such a change and an improvement is seen. The long-term results look to be the same as the short-term results of previous simulation (figure 29). It looks like over a long enough time we would see behaviour like 29, but an accuracy like this for 500 periods will be more than good enough.

Notice the two PEFRL steps, which implies there is at least double the computation per step compared to the non time-adaptive schemes. We want to see if this has a big effect on the run-times. In the non-adaptive case, trial and error suggests $h = 0.12$ and $h = 0.6$ gives a maximum energy error of 1% for Leapfrog and PEFRL respectively. Using these step sizes for both the non-adaptive and adaptive schemes, a fair comparison can be made at 10 and 500 periods, shown in table 4. Note that this is the run time of all calculations, including energy and angular momentum, and therefore dealing with memory. Nonetheless, it is clear that using this adaptive step size is much faster in the long term and that, as expected, PEFRL is quicker as it can handle a larger scaling coefficient.

Num. Periods	Leapfrog		PEFRL	
	Non-adaptive	Adaptive	Non-adaptive	Adaptive
10	0.34569	0.21065	0.08799	0.08590
500	125.68351	25.65789	5.79929	3.22122

Table 4: Run-time comparisons of non-adaptive and time-adaptive Leapfrog and PEFRL.

We can now look back at the motivating case - the hyperbolic orbit (3.14). Figure 31 gives us good confidence in the improvements. The energy still spikes as the bodies come close but stays at a lower order of magnitude. The angular momentum is even better than before. Furthermore, more steps are taken as the bodies come close and then get more sparse as they fly away. One problem is that the energy starts to increase again rather than level off because the step size is monotonically increasing. If this is shown to be an issue in further calculation, an upper limit can be added to the step size.

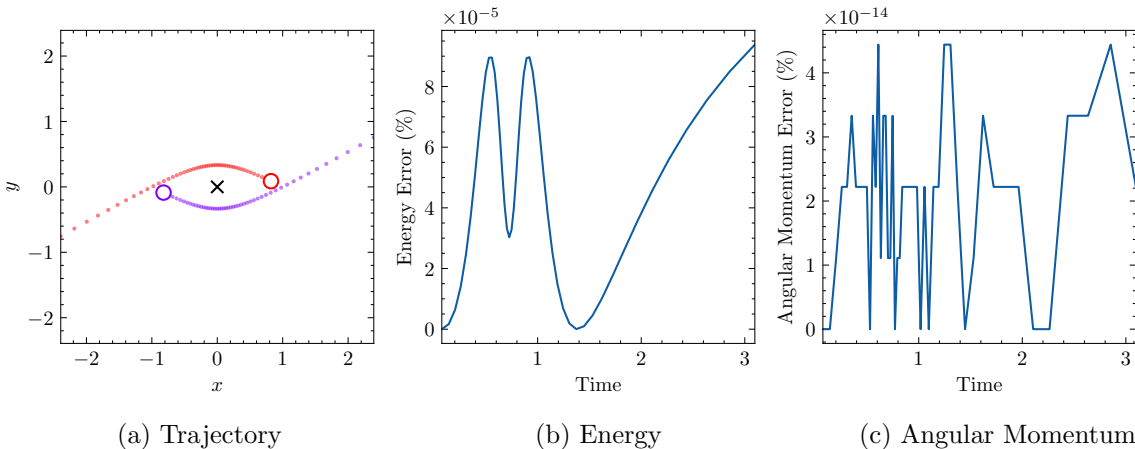


Figure 31: Adaptive integration of a hyperbolic orbit using PEFRL and step scaler $C = 0.1$.

3.3.2 Runge-Kutta-Fehlberg

This method of an adaptive step size worked well, but there may be a better method. General adaptive step size schemes do already exist, and it makes sense to compare to one. The existing method chosen to compare to is Runge-Kutta-Fehlberg (RK45) [6, 7], developed by German mathematician Erwin Fehlberg. It is a fourth-order Runge-Kutta method with a fifth order error estimator. Although it has previously been decided that RK4 wasn't appropriate, this was because it wasn't Symplectic, but our new adaptive scheme isn't either. RK45 works by first calculating one Runge-Kutta step using the Butcher Tableau 5 at step size h .

0	0	0	0	0	0	0
1/4	1/4	0	0	0	0	0
3/8	3/32	9/32	0	0	0	0
12/13	1932/2197	-7200/2197	7296/2197	0	0	0
1	439/216	-8	3680/513	-845/4104	0	0
1/2	-8/27	2	-3544/2565	1859/4104	-11/40	0
	25/216	0	1408/2565	2197/4104	-1/5	0
	16/135	0	6656/12825	28561/56430	-9/50	2/55

Table 5: Butcher Tableau for RKF45 [6, 7].

The two bottom rows give a fourth and fifth order solution. By taking the absolute difference between these the local truncation error, τ , can be estimated. If the local truncation error is less than some threshold, ϵ , then the fifth order solution is used and step size increased to $h_{\text{new}} = 5h$. If $\tau > \epsilon$ then disregard this solution and pick a new step size by

$$h_{\text{new}} = 0.9 \cdot h \cdot \left(\frac{\epsilon}{\tau}\right)^{\frac{1}{5}}. \quad (3.18)$$

This method is implemented and tested on the motivating hyperbolic case shown in figure 32. From this, it is easy to see that adaptive-PEFRL performs much better (lower energy error) for the same parameters and cost. In fact, RK45 took 1.47 seconds compared to the 0.032 seconds of adaptive-PEFRL. This isn't to say RK45 isn't good, in fact it calculates accurately and could be used in the problem, but adaptive-PEFRL is just better. Time could be spent checking the implementation, fine-tuning the parameters, or applying this local truncation idea to other methods, but it will likely waste time. As a result, the remainder of this project uses the adaptive PEFRL integrator.

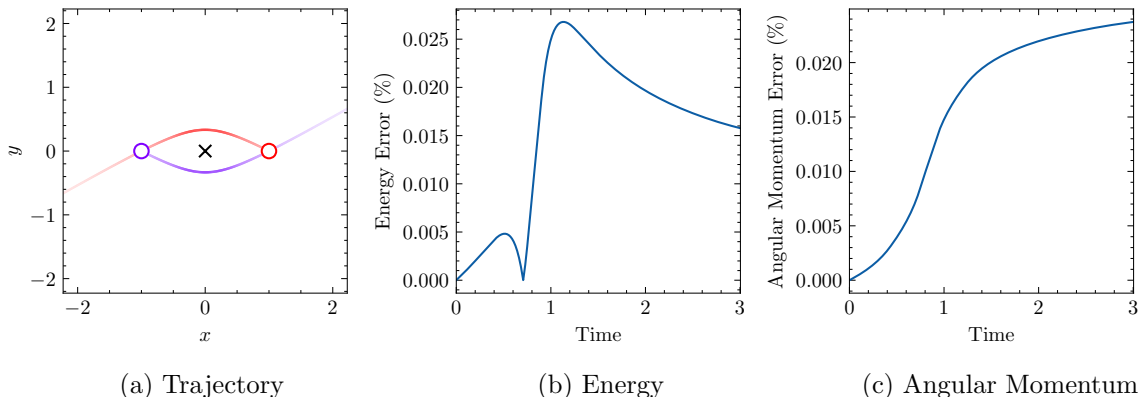


Figure 32: Adaptive integration of a hyperbolic orbit using RK45 with $\tau = 10^{-6}$.

4 Three-body orbits

Now that we have access to an accurate and efficient N-body integrator, it can be used to analyse the dynamics and stability of a few known figure-8 in the xy -plane three-body orbits that obey system 2.3. Namely, the figure-8 and equal-mass, circular Euler and Lagrange orbits in the xy -plane.

4.1 Integration of known Orbits

4.1.1 Figure-8

We begin by integrating figure-8 in the xy -plane using adaptive PEFRL. Montgomery [21] tells us the figure-8 has initial conditions

$$\begin{cases} \mathbf{r}_1(0) = [-1, 0, 0]^T, & \mathbf{r}_2(0) = [0, 0, 0]^T, & \mathbf{r}_3(0) = [1, 0, 0]^T \\ \mathbf{v}_1(0) = [p_1, p_2, 0]^T, & \mathbf{v}_2(0) = [-2p_1, -2p_2, 0]^T, & \mathbf{v}_3(0) = [p_1, p_2, 0]^T \end{cases} \quad (4.1)$$

where $p_1 = 0.347111$ and $p_2 = 0.532728$. This has $E_0 = -1.287146$, $L_0 = 0$ and a period of $T = 6.324449$. Notice that the initial velocities sum to zero in each direction, which is important for conservation of the CM. Figure 33 shows integration of ten periods using $C = 0.1$. The energy error very low, so $C = 0.1$ has scope to be increased. Furthermore, the integration looks to be correct and adaptive-PEFRL is working on this case.

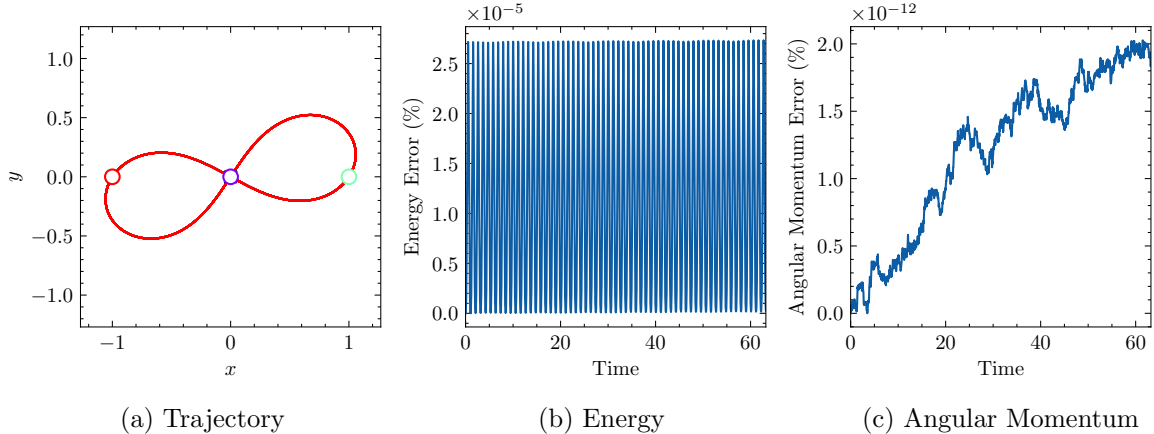


Figure 33: 10 period, Figure-8 integration with $C = 0.1$.

4.1.2 Euler's Solution

The second orbit to be discussed is one of Euler's collinear solutions. As discussed in section 2, the masses in Euler's orbits begin on a line and rotate about the centre of mass while maintaining this structure. In the equal-mass, circular case they are placed in the same configuration as the figure-8, so that the outer masses move on a circle with radius 1. Furthermore, the speed at which to let the bodies off at can be found analytically, without using the action. The absolute centrifugal force of mass i at a distance R from the centre is defined as:

$$|\hat{\mathbf{F}}_i| = m_i \omega_i^{2R}, \quad (4.2)$$

for $i = 1, 2, 3$, where $\omega = |\boldsymbol{\omega}|$ is the angular velocity initially acting in the y -direction. The resultant force acting on m_3 is $\mathbf{F}_3 = [0, 5/4, 0]^T$, which has magnitude $5/4$. Equating this to the centrifugal force gives

$$\omega = \sqrt{\hat{F}_3} = \frac{\sqrt{5}}{2} \quad (4.3)$$

Then the initial conditions, spinning clockwise, are written

$$\begin{cases} \mathbf{r}_1(0) = [-1, 0]^T, & \mathbf{r}_2(0) = [0, 0]^T, & \mathbf{r}_3(0) = [1, 0]^T, \\ \mathbf{v}_1(0) = [0, \omega]^T, & \mathbf{v}_2(0) = [0, 0]^T, & \mathbf{v}_3(0) = [0, -\omega]^T, \end{cases} \quad (4.4)$$

with $E_0 = -5/4$, $L_0 = 2\omega = \sqrt{5}$ and period $T = 2\pi/\omega = 4\pi/\sqrt{5}$.

Integrating these initial conditions for 10 periods gives figure 34. It is seen that the energy is much lower than the figure-8. The reasoning is similar to the two-body zero-eccentricity ellipse: the relative distances and velocities remain the same at every step.

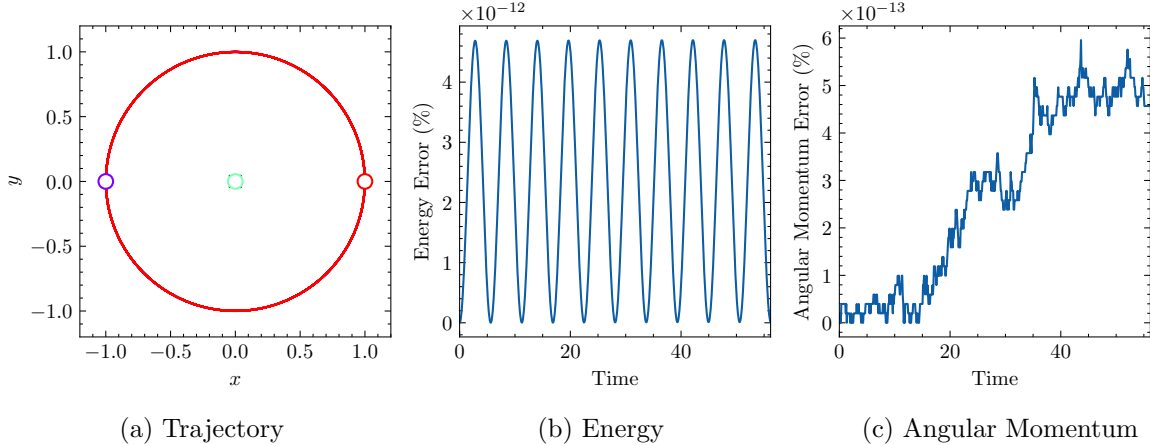


Figure 34: 10 period, integration of Euler's equal-mass, circular solution with $C = 0.1$.

4.1.3 Lagrange's Solution

The final 3-body orbit studied is one of Lagrange's solutions, where bodies move around a circle on vertices of an equilateral triangle. To be comparable with Euler's solution, the masses are also placed on a circle radius one but with an angle $2\pi/3$ between each. Employing the same thinking as (4.4), the initial conditions are

$$\begin{cases} \mathbf{r}_1(0) = [0, 1, 0]^T, & \mathbf{r}_2(0) = [-\cos \frac{\pi}{6}, -\sin \frac{\pi}{6}, 0]^T, & \mathbf{r}_3(0) = [\cos \frac{\pi}{6}, -\sin \frac{\pi}{6}, 0]^T, \\ \mathbf{v}_1(0) = [\omega, 0, 0]^T, & \mathbf{v}_2(0) = [\omega \sin \frac{\pi}{6}, -\omega \cos \frac{\pi}{6}, 0]^T, & \mathbf{v}_3(0) = [\omega \sin \frac{\pi}{6}, \omega \cos \frac{\pi}{6}]^T, \end{cases} \quad (4.5)$$

where $\omega = 3^{-1/4}$, with $E_0 = -3/2\sqrt{3}$, $L_0 = 3\omega = 3^{3/4}$ and period $T = 2\pi/\omega = 2 \cdot 3^{1/4} \cdot \pi$.

Figure 35 shows the same integration as Euler's solution and the figure-8. Clearly something goes wrong here - the integration completes seven periods of the circle before admitting non-periodic behaviour. Figure 36) shows the results of a more precise integration, with $C = 0.001$ (figure 36). This helps, but the solutions still begin to spiral out of control on the tenth period.

The energy error is now at machine precision, so a lower step size will not help. To verify, the energy of the final trajectory points is checked: $E_{10T} = -0.8660254037844418 \approx -0.8660254037844386 = E_0$. The error is almost exactly conserved, but this doesn't line up with the exhibited behaviour.

We can be certain that the implementation is correct, as both Euler and the figure-8 work. Furthermore, the initial conditions give the expected behaviour for the first periods. Clearly, the system is sensitive to small error, even at machine precision. What this points out that the Lagrange orbit is unstable. Our aim to measure this instability alongside the stabilities of Euler's solution and the figure-8. Keep in mind that integration of Lagrange's solution does at least exhibit the expected behaviour for five periods, even at $C = 0.1$.

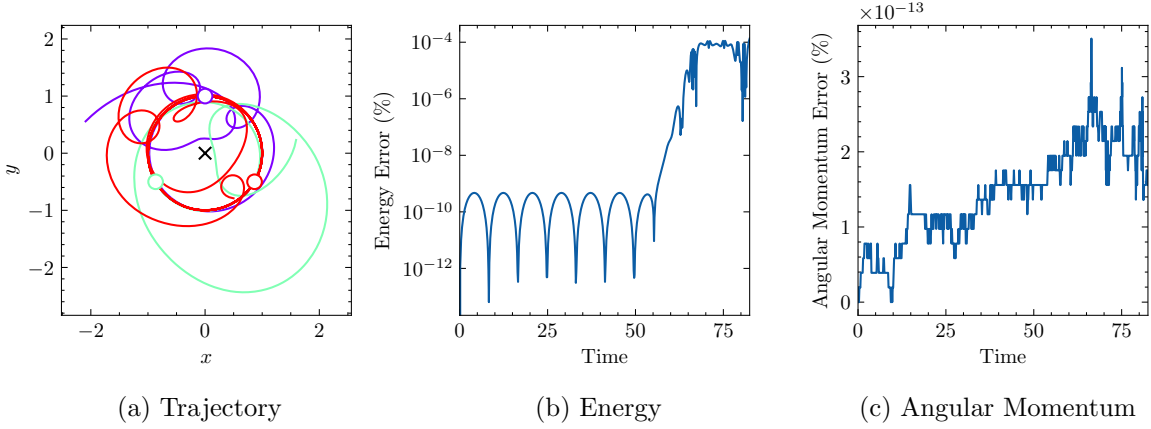


Figure 35: 10 period, integration of Lagrange's equal-mass, circular solution with $C = 0.1$.

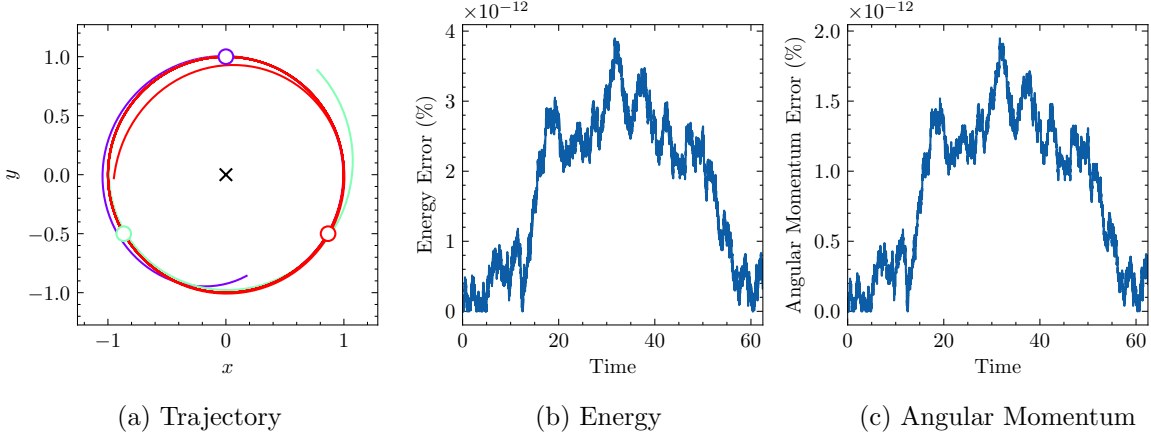


Figure 36: 10 period, integration of Lagrange's equal-mass, circular solution with $C = 0.001$.

4.2 Stability of the Figure-8

This section regards the stability of the above orbits. It will be easier to start on the stable, figure-8, case and check the methodology is correct, before applying it to the unstable cases. As mentioned in Section 2, the figure-8 orbit has previously been proven to be KAM stable [21, 23], but we will perform our own analysis on the stability, to learn more about its behaviour.

4.2.1 Perturbations of the initial Conditions

To measure the stability of the figure-8, we are interested in the long -term behaviour of solutions through small perturbations of the initial conditions (4.1). However, the big question comes with how the initial conditions are perturbed - there are 18 variables in the three-body system (2.3), which is a lot to pick from. To make a qualitative and direct comparison with the unperturbed figure-8 it makes sense to pick perturbations which give the same energy and angular momentum. Montgomery [21] tells us the figure-8 can be scaled, rotated and flipped. Therefore, perturbations are kept in the xy plane. With that in mind, let a perturbed figure-8 have initial conditions

$$\begin{cases} \mathbf{r}_1(0) = [-R, 0, 0]^T, & \mathbf{r}_2(0) = [0, 0, 0]^T, & \mathbf{r}_3(0) = [R, 0, 0]^T \\ \mathbf{v}_1(0) = [p'_1, p'_2, 0]^T, & \mathbf{v}_2(0) = [-2p'_1, -2p'_2, 0]^T, & \mathbf{v}_3(0) = [p'_1, p'_2, 0]^T \end{cases} \quad (4.6)$$

where $p'_1 = p_1 + \delta v_x$, $p'_2 = p_2 + \delta v_y$ and radius R are to be determined. A direct relationship between these three variables can be made. Let E_0 and L_0 be the initial energy and angular momentum of the unperturbed figure-8, and E'_0 and L'_0 the initial energy and angular momentum of the perturbed orbit. Notice that $L'_0 = | -p'_2 \cdot R + p'_2 \cdot R | = 0 = L_0$ is always satisfied. Then

it remains to find an energy equivalence. The perturbed energy can be written

$$\begin{aligned} E'_0 &= K'_0 + U'_0 = K'_0 - G \frac{m_1 m_2}{R} + \frac{m_1 m_3}{2R} + \frac{m_2 m_3}{R}, \\ &= K'_0 - G \frac{2m_1 m_2 + m_1 m_3 + 2m_2 m_3}{2R}, \end{aligned} \quad (4.7)$$

where K'_0 is a function of p'_1, p'_2 and the m_i . Rearranging and enforcing $E'_0 = E_0$ gives

$$R = G \frac{2m_1 m_2 + m_1 m_3 + 2m_2 m_3}{2(K'_0 - E_0)}. \quad (4.8)$$

Substituting masses $m_i = 1$ and $G = 1$ gives the relationship

$$R = \frac{5}{2(K'_0 - E_0)}. \quad (4.9)$$

Therefore, for any perturbation $\delta v_x, \delta v_y$ around the unperturbed figure-8, all the perturbed initial conditions (4.6) can be directly calculated. This is important because only two variables need to be investigated to understand stability.

4.2.2 Region of Stability

The next question to answer is how to measure stability. The goal is to determine whether the succeeding motion of a perturbed initial condition exhibits qualitatively similar behaviour to the unperturbed figure-8.

In the unperturbed figure-8, the maximum and minimum distances between bodies remains in a tight bound. In fact, we can look at the distribution of step size over 200 orbits (figure 37). The step sizes are bound between $0.16 \leq h \leq 0.23$ for $C = 0.5$. Therefore, we stop an orbit evolution if the step size becomes significantly smaller than this (dependent on C) or the maximum distance, d , between any two masses gets significantly large. These conditions tell us the perturbed orbit no longer acts like the unperturbed orbit, and there is no point continuing.

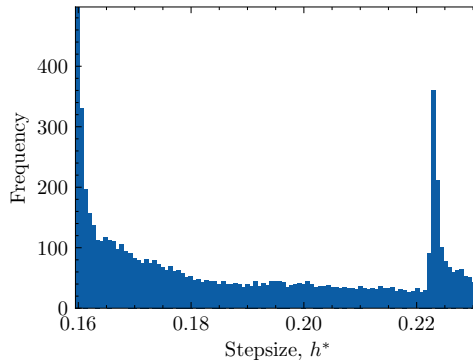


Figure 37: Step size distribution for the fig-8 orbit over 200 orbits, with $C = 0.5$.

On top of this, an orbit calculation is stopped if its energy gets large, suggesting a higher accuracy is needed. We don't worry about angular momentum, as it has been shown to sit around machine precision. Lastly, we stop at a long-term number of periods, suggesting qualitatively similar behaviour of orbits. This gives the stopping conditions:

- $E > 1\%$,
- $h < 0.001$,
- $t > 1000$ (~ 160 periods),
- $d = \max |{\mathbf r}_i - {\mathbf r}_j| > 10$.

These conditions are strategically chosen but still arbitrary and subject to change if needed. For example, the value of C impacts both step size and energy error. A perturbation search is performed on a zoomed out, discrete, 101×101 region where $-2 < \delta v_x, \delta v_y < 1$. Integration is done from each initial condition given by equations (4.6) & (4.9). Integrating 160 periods of the unperturbed orbit with $C = 0.5$ gives an energy error of 0.2%, so we use this to start.

Perturbations are coloured according to the stopping condition. Green is where perturbations complete full integration, so are likely bounded at long time and therefore periodic. This is what we will consider ‘stable’: orbits that start near stay near for a long time. Beige is the region of high error and anything else is qualitatively different behaviour to the figure-8, or ‘unstable’.

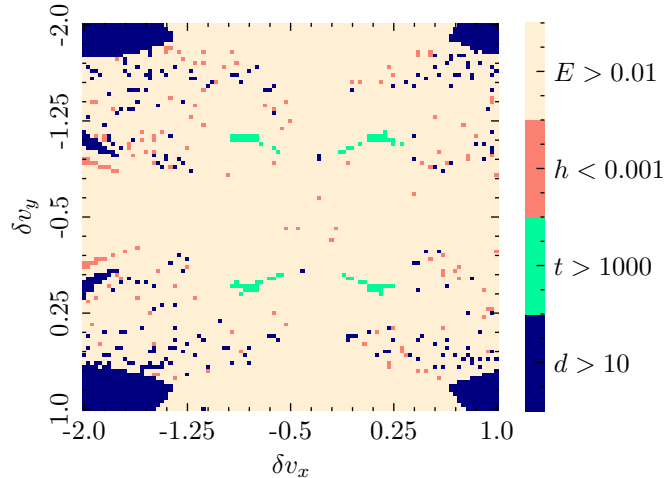


Figure 38: Zoomed-out, region of stability of the figure-8 orbit.

Figure 38 shows that $C = 0.5$ is too high, and most perturbations stop due to energy error. However, this simulation is not completely useless. There is an obvious symmetry in the x and y directions, which means the orbit can be flipped along the x and y axis and yield the same results, confirming symmetry. We zoom in to the original orbit (4.1) and perform the search on a 201×201 grid where $-0.3 < \delta v_x, \delta v_y < 0.3$, but with $C = 0.4$. Furthermore, the ‘escape time’ is defined as the final time of integration.

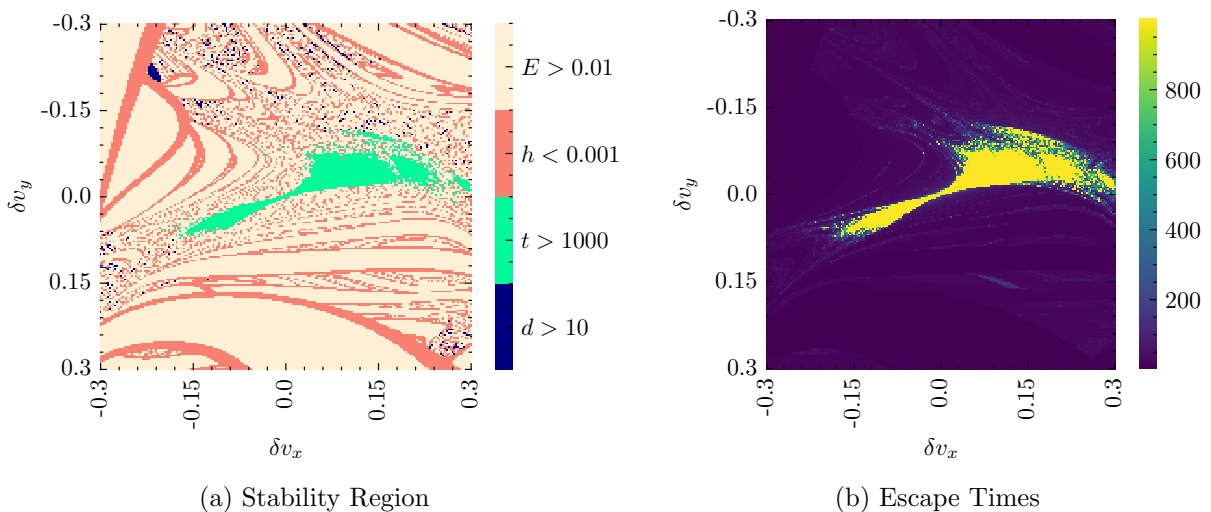


Figure 39: Region of stability of the figure-8 orbit, with $C = 0.4$

Figure 39a shows that $C = 0.4$ does a better job at finding the stable region, but not entirely. There are bands of high energy that get tighter moving toward the stable region, but inside these bands is unknown. The most obvious solution here is to re-simulate again with a smaller step size $C = 0.2$.

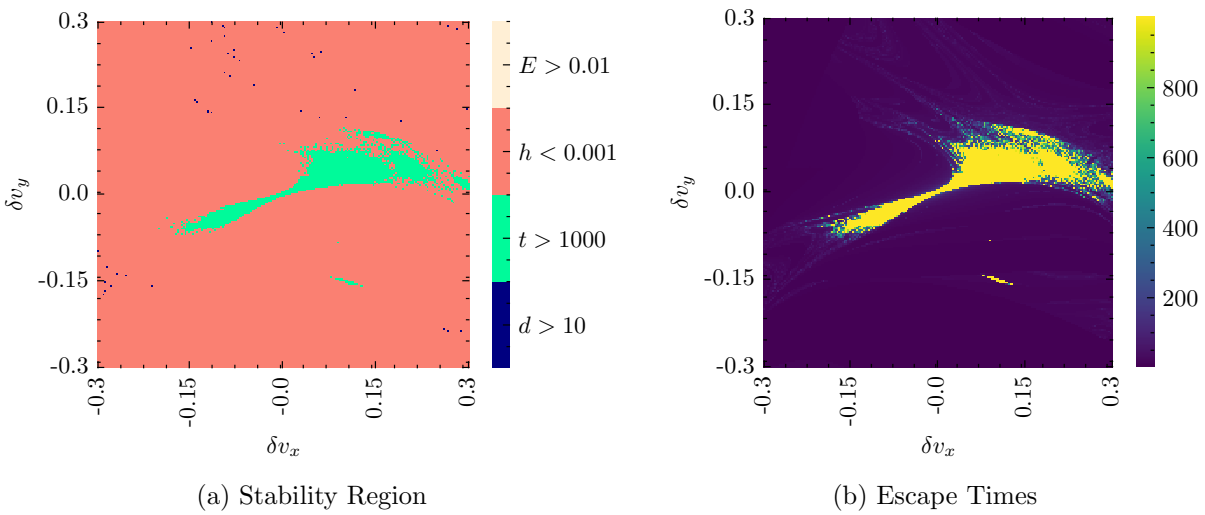


Figure 40: Region of stability of the figure-8 orbit, with $C = 0.2$.

Figure 40 is more precise and fills in the question marks. There is a clear border between stable and unstable perturbations and a small separate region of stability. However, before making any concrete conclusions about this we would like a higher resolution version, but that is going to be a computationally expensive task to generate. Hence, we would like to save time when possible. The stable region is approximately the same across both simulations, which tells us we might be able to get away with the higher $C = 0.4$, if we stop earlier. We rarely stop because of $d > 10$, so this can be decreased to $d > 5$. Most stops come with $h < 0.001$, so it is likely this can be increased to $h < 0.01$ (bearing in mind that a higher C increases h also).

Moreover, the escape times of both simulations (figures 39b & 40b) are very similar for either value of C . The escape times tell us most of the computation comes with calculating the full, long time orbits, and that we need not calculate so many periods. A maximum time of 400 (~ 60 orbits) looks like the stability region will maintain its structure.

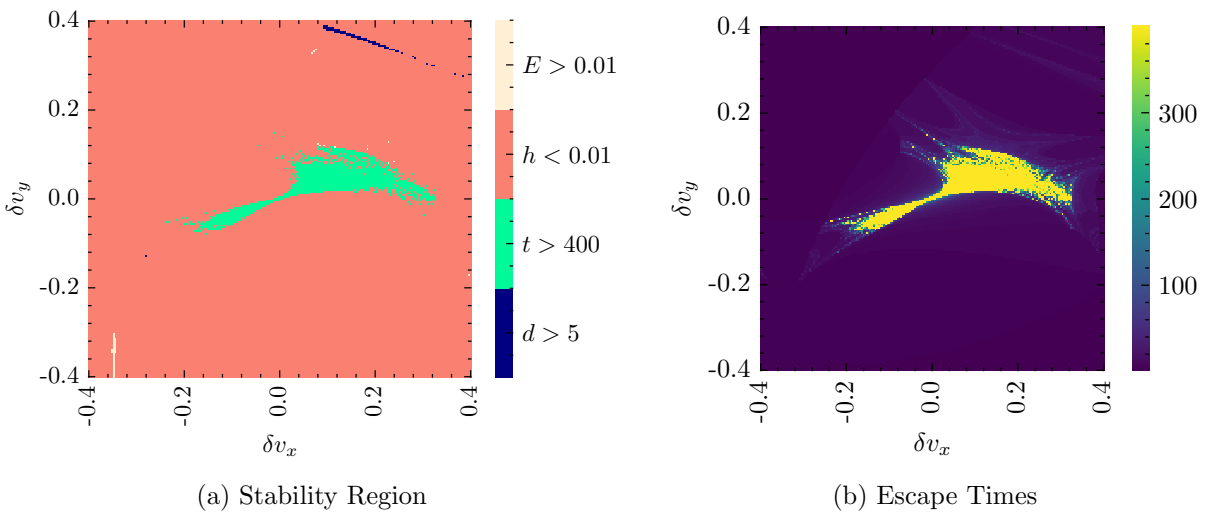


Figure 41: Region of stability of the figure-8 orbit, with $C = 0.4$ and adjusted parameters.

Another simulation is done with the adjusted parameters, on a larger crop $-0.4 < \delta v_x, \delta v_y < 0.4$, yielding figure 41. This was much quicker to generate, but at the cost of some accuracy. The stand-alone orbit is lost to the larger step size restriction and larger C . Furthermore, the stability region is slightly less fine, but it's hard to tell if this is due to step size, the time restriction, or mesh resolution. The wider crop is proven to be a good choice as it captures the full region.

Moving forward, time could be spent optimising these parameters, but this seems a little pointless. The step size and distance restrictions don't save much time, so it would be better if they remained as in figure 40b. Furthermore, we would rather be integrating accurately, so we choose $C = 0.2$. The consequent time-hindrance can be countered by reducing the maximum integration time to $t \leq 400$.

To see what is happening within the region of stability, some of the 'stable' trajectories can be plotted. Figure 42 shows one solution close to the unperturbed figure-8, and one farther away. The bodies on the closer solution move on three separate figure-8-like paths. It's harder to decipher the motion on figure 42b, but seemingly an extreme version of the motion in figure 42b. The closer solution can be considered more 'closed' than the outer solution. Understanding more about the region of stability points toward measuring this closure, which the next section addresses.

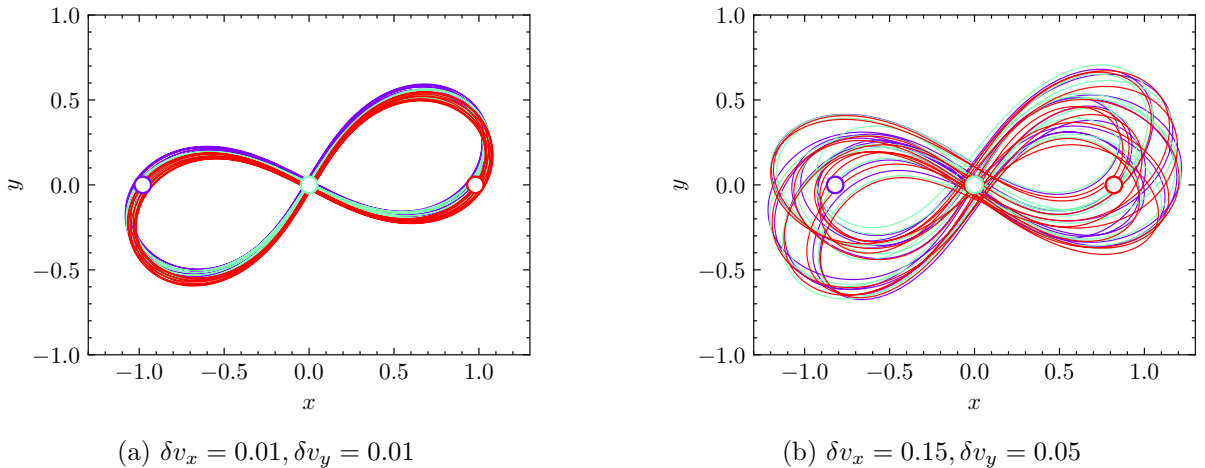


Figure 42: Example 'stable', perturbed figure-8 orbits.

4.2.3 Closure

To measure the closure of an orbit, we can look at the shape the three bodies make, as vertices of a triangle. Let the sides of the triangle be defined by the vectors

$$\begin{cases} \mathbf{x}_1 = \mathbf{r}_3 - \mathbf{r}_2, \\ \mathbf{x}_2 = \mathbf{r}_3 - \mathbf{r}_1, \\ \mathbf{x}_3 = \mathbf{r}_2 - \mathbf{r}_1, \end{cases} \quad (4.10)$$

with lengths $x_1 = |\mathbf{x}_1|$, $x_2 = |\mathbf{x}_2|$ and $x_3 = |\mathbf{x}_3|$. The normalised triangle is given by

$$\begin{cases} \hat{\mathbf{x}}_1 = \mathbf{x}_1/M, \\ \hat{\mathbf{x}}_2 = \mathbf{x}_2/M, \\ \hat{\mathbf{x}}_3 = \mathbf{x}_3/M, \end{cases} \quad (4.11)$$

where $M = x_1 + x_2 + x_3$. Then any two sides of the triangle determine its shape by $\hat{x}_1 + \hat{x}_2 + \hat{x}_3 = 1$. Plotting \hat{x}_2 against \hat{x}_1 at every time step gives a path in 'shape space'. Note: a periodic orbit is expected to be periodic in shape space and $0 \leq \hat{x}_i \leq 1/2$.

Figure 43a shows how the unperturbed and a perturbed figure-8 look in such a shape space. It demonstrates that a closed orbit takes up less space than a lesser closed orbit. As a result, to measure how closed an orbit is, we want to measure its area in shape space. To do this, place a grid over the shape space and fill in every grid point where more or one of the path coordinates lie (figure 43b). Then the total number of filled grid points is its area, dependent on grid size. We express the closure in the same way as energy error, as a percentage relative to the minimum

closure. Then the unperturbed figure-8 has a closure of 0%. Lower closure % indicates an orbit is more similar to the unperturbed orbit.

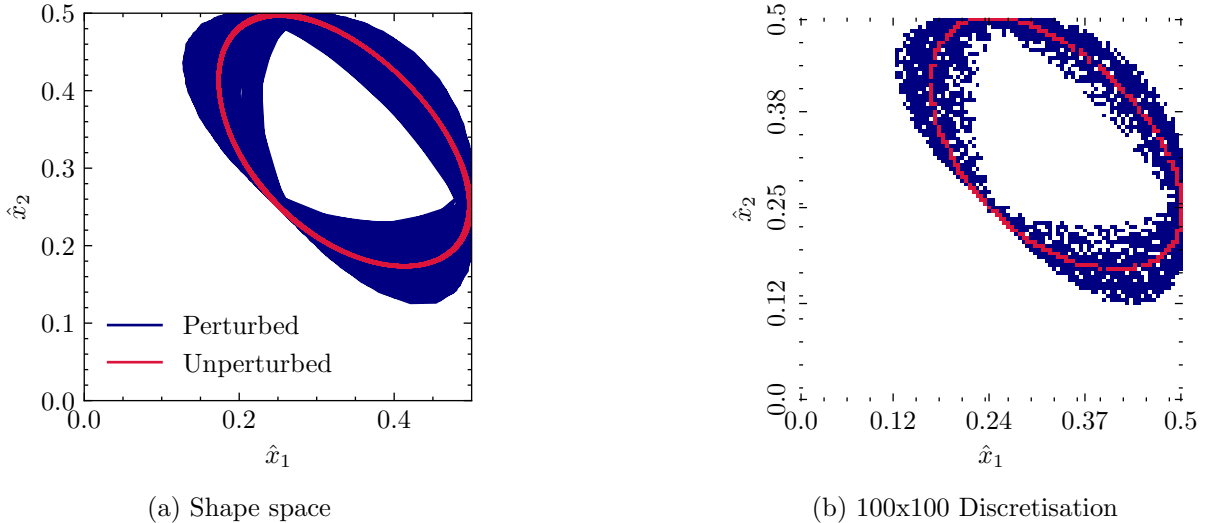


Figure 43: Grid coverage for the un-perturbed and perturbed figure-8 orbit. Unperturbed covers 249 grid-squares, perturbed covers 1650.

Using a grid size of 500x500, this method is applied to every orbit found in the stable region. Specifically, the data from most accurate experiment with $C=0.2$ and $t \leq 1000$. Any orbit in the unstable region will be assigned an arbitrarily high closure, e.g. the maximum closure of the stable region.

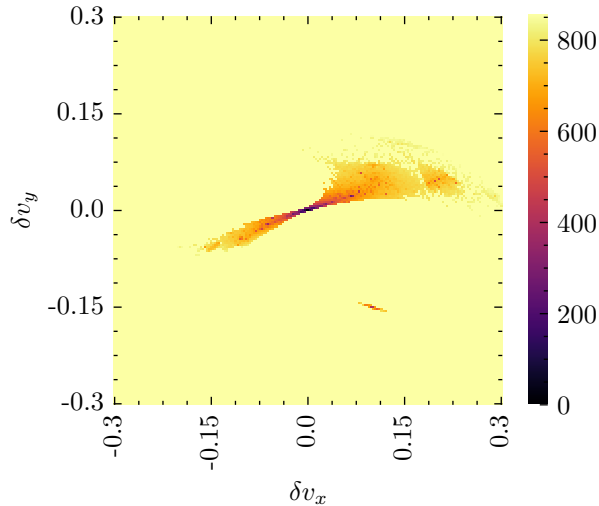


Figure 44: Closure (%) of perturbations of the figure-8, with grid-size 500x500.

Figure 44 shows the results of such an experiment. The orbits closer to the unperturbed figure-8 are more closed than the outer orbits. The effects of using different grid sizes to discretise the shape space are in figure 45. It is evidenced that a finer resolution actually harms the results. Less variation in the upper closures is seen, and the maximum closure (%) drops. With more boxes to fill and only a finite number of points in our trajectory, the filled boxes are more sparse. Running the integration for longer would improve this, but this has obvious downsides. On the other hand, bringing the resolution down gives less variation in the lower closures and increases the maximum closure (%). Consequently, a shape space grid size of 500x500 seems sensible, at least for these time periods.

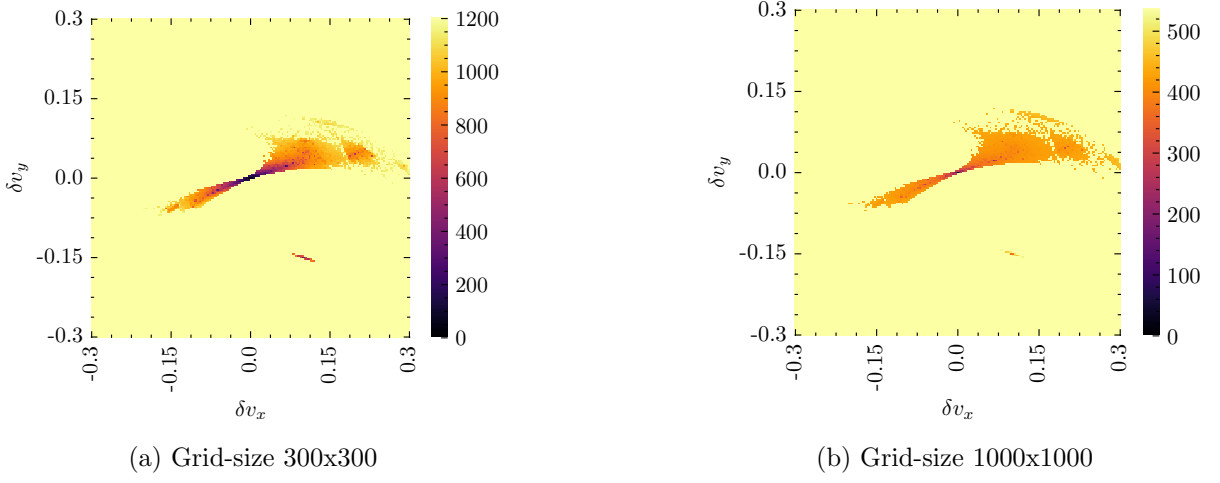


Figure 45: Closure (%) of perturbations of the figure-8, with varying grid sizes.

4.2.4 Higher resolution Results

To draw some conclusions about the figure-8 we generate a higher (400x400) resolution image of the previous section's results. We use $C = 0.2$, stop on $0.001 > h, d > 10, E > 1\%, t \geq 400$ and discretise the shape space on a grid size 500x500. Some of the intricacies have already been discussed, but this section ties them together.

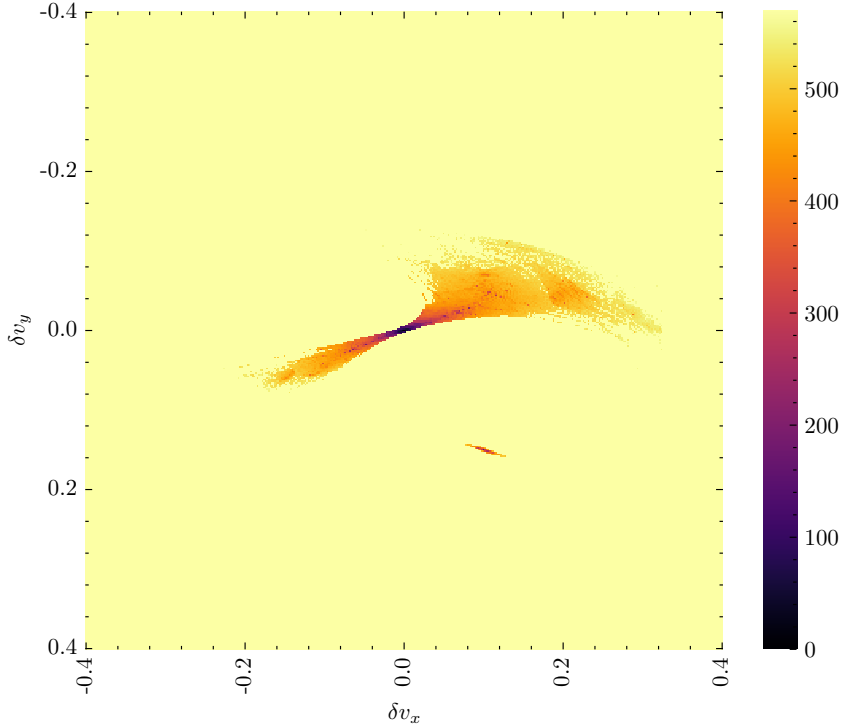


Figure 46: Closure of perturbations of the figure-8 orbit. Darker colours indicate regions of low closure.

Figure 46 tells us that the figure-8 orbit is indeed stable. Orbits through small perturbations of the figure-8 stay near for long-time. Furthermore, the closure tells us that the small perturbations are generally more closed than larger perturbations. As a consequence, the closed orbits can be considered more stable. The figure-8 is more stable in one direction than the other, roughly where $\delta v_x = 2\delta v_y$. Intuitively this makes sense - Figure 33 shows the figure-8 is twice as long as it is tall, so the relative change in both directions is the same. When an orbit moves in or out of the stability region it undergoes a bifurcation and changes stability.

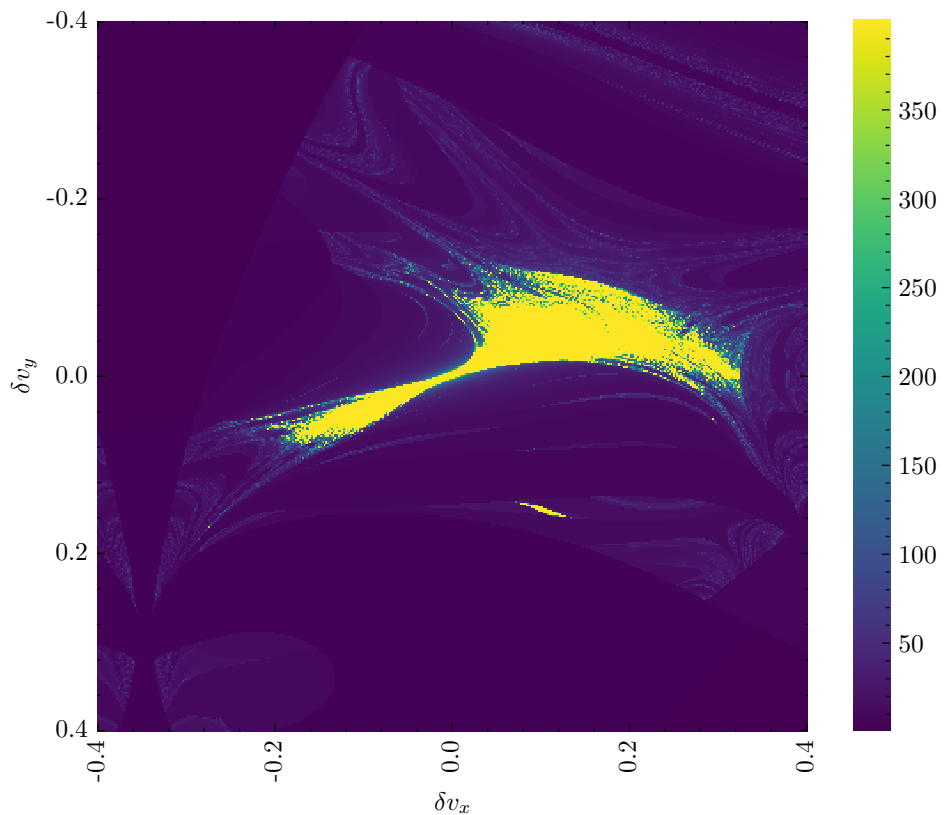


Figure 47: Escape times of perturbations of the figure-8 orbit. Lighter colours indicate regions of higher escape times. Darker colours indicate regions of low escape times.

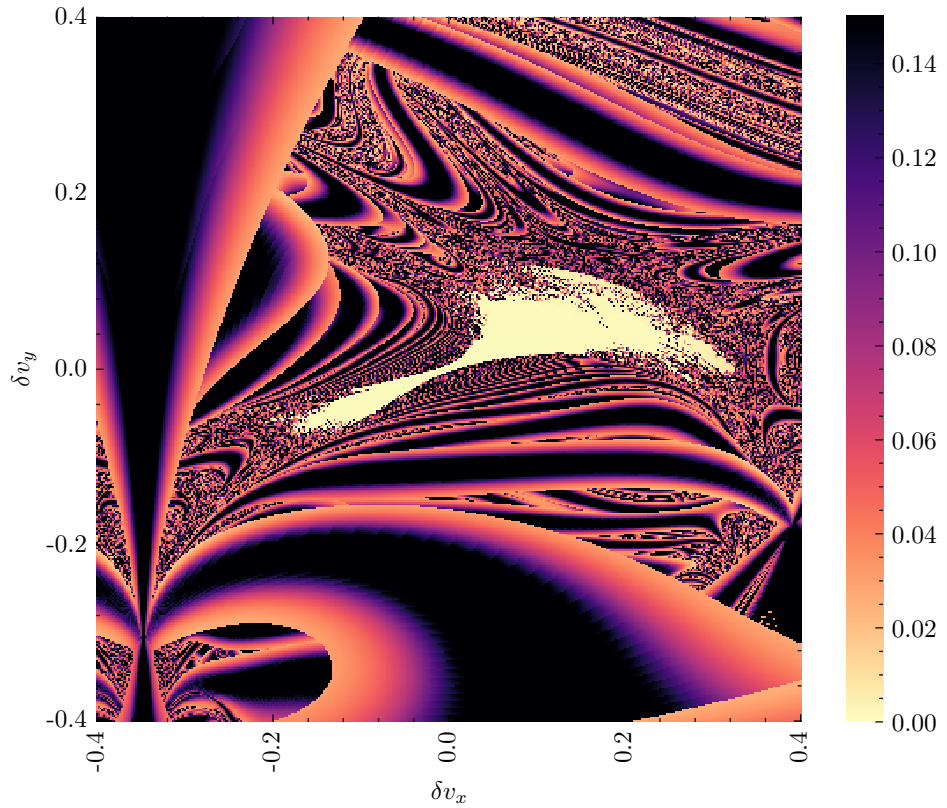


Figure 48: Maximum energy error (%) of perturbations of the figure-8 orbit. Lighter colours indicate regions of low energy. Darker colours indicate regions of high energy.

The escape times (Figure 47) tells us that the maximum escape time can be reduced further, and we need not run so many periods to understand the stability region. This is important for analysing the unstable cases where even the exact solutions may act chaotically due to introduced error and therefore integrating hundreds of periods will yield useless results.

From Figure 48 it is clear that the stable region gives a distinctly lower energy error. We can go one step further in figure 49 and cap the energy error. This shows that the energy error in the stable region is at its lowest toward the unperturbed orbit. As a result, the energy could be used as a marker of stability. In this scenario, energy that grows slowly indicates a more stable orbit, than an orbit with fast-growing energy. This makes sense, as the unperturbed orbit has no close interactions of bodies, whereas an unstable orbit does.

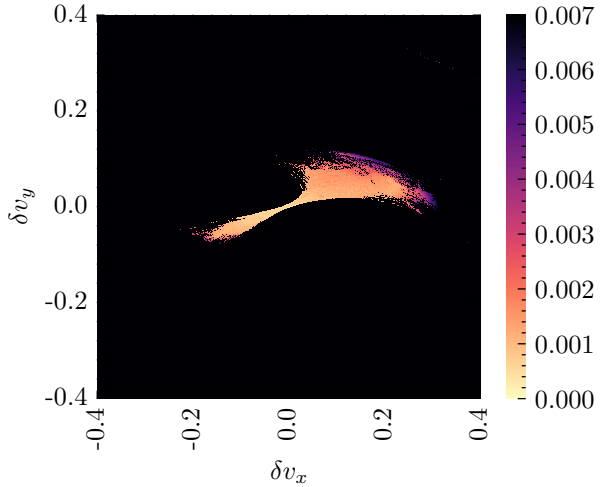


Figure 49: Maximum energy error (%) of perturbations of the figure-8 orbit, where $E < 0.007\%$.

Notice the small, standalone, stable cluster away from the unperturbed orbit in figures 46 & 47. This is likely a separate periodic orbit, and we investigate it. This region does not appear in the energy plot, but maybe it is just less stable than the figure-8 and has close interactions. This could be why it doesn't appear in Figure 41.

4.2.5 Moth I

We zoom in on the cluster and calculate the stable region and closures using the aforementioned method. Note that closure is calculated relative to the minimum closure on this grid. This gives figure 50, showing that there is a stable orbit at its centre, but less stable ones around it. The most closed candidate has perturbations $\delta v_x = 0.12286$ and $\delta v_y = -0.15566$ and the initial conditions are given by equation (4.6) as $R = 1.05205$, $p'_1 = 0.46998$ and $p'_2 = 0.37707$.

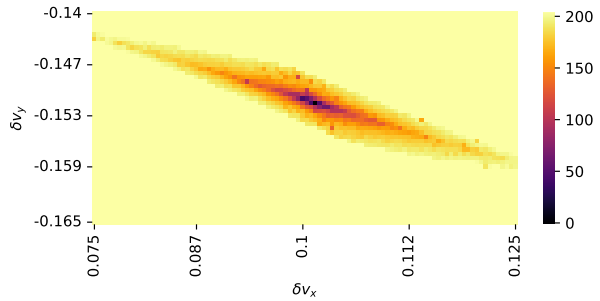


Figure 50: Closure (%) of the Moth I orbit.

We integrate 20 periods with $C = 0.2$ to give Figure 51, showing that there is indeed a periodic orbit distinctly different from the figure-8. This orbit looks much like the orbit found by Šuvakov [34] in 2014, dubbed ‘Moth I’. However, it is not perfect - with three bodies moving

on three different paths, we expect the shape space to show one distinct path. This tells us we need to keep zooming in. The method to zoom in is as follows: find the minimum closure and associated initial conditions; pick a smaller perturbation search area around the new initial conditions; find the closures of orbits in the new search area; repeat until sufficiently small.

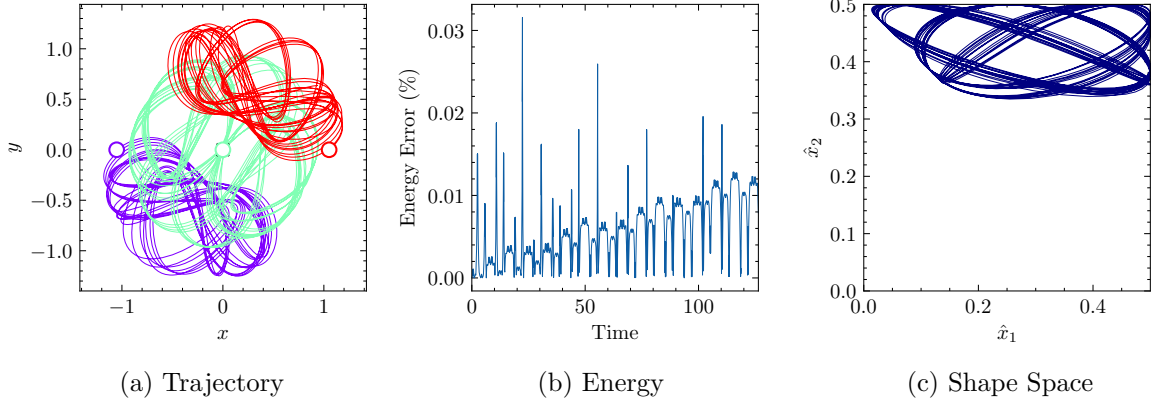


Figure 51: 20 period integration of Moth I with initial conditions $R = 1.05205, p'_1 = 0.46998$ and $p'_2 = 0.37707$.

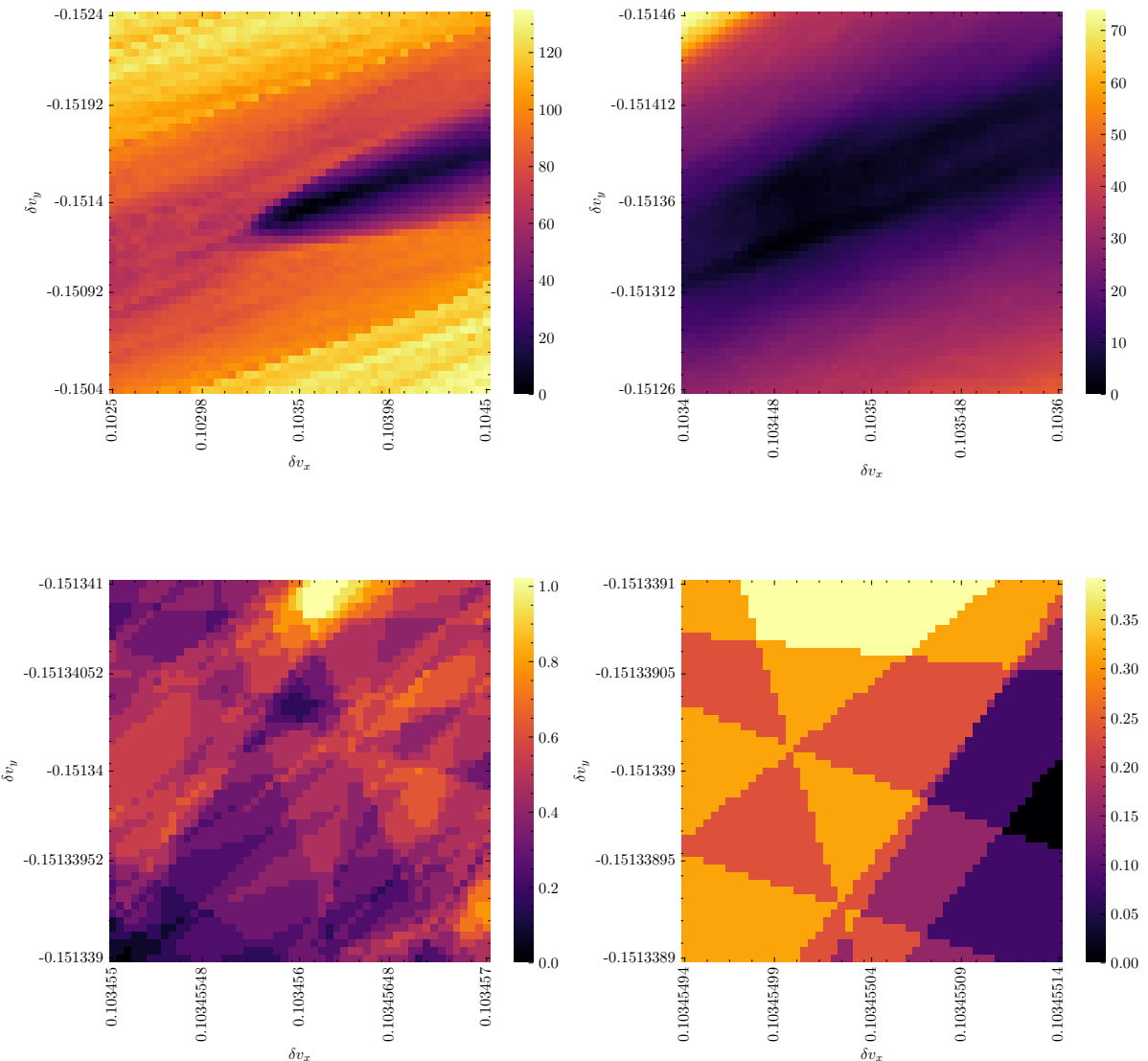


Figure 52: Progressive zooming on the closure (%) of Moth I.

Figure 52 illustrates the zooming in process, on what is expected to be the most closed of the Moth orbits. More precise values of $\delta v_x = 0.103455112$ and $\delta v_y = -0.151338969$ are found, giving $R = 1.071789884$, $p'_1 = 0.450566112$ and $p'_2 = 0.381389032$. Once again, we integrate 20 periods to give Figure 53. The shape space and trajectories are much tighter and the maximum energy error has halved. This is a more stable and better version of the initial guess. However, the orbit is still not perfectly closed, suggesting we are still not quite there.

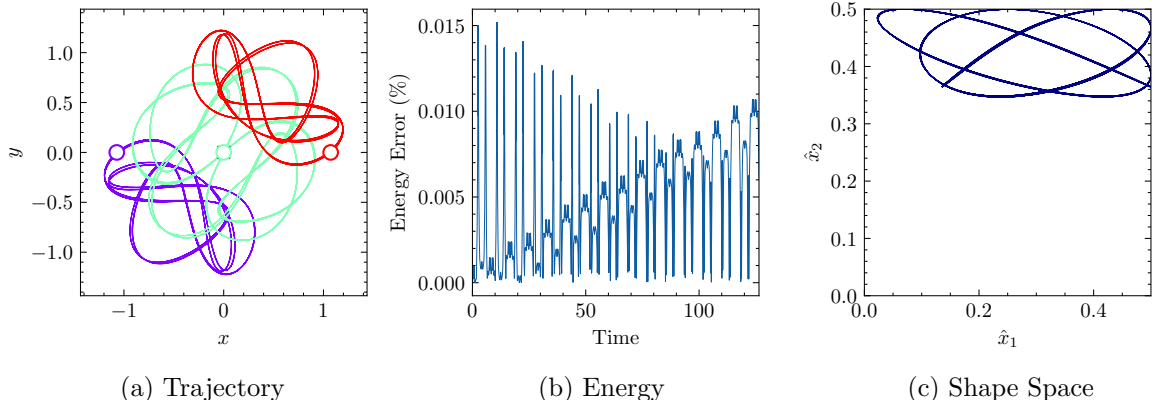


Figure 53: 20 period integration of Moth I with initial conditions $R = 1.071789884$, $p'_1 = 0.450566112$ and $p'_2 = 0.381389032$.

Notice that in the zooming in process, the closures get smaller each stage, and we get regions of identical closure. Distinguishing between perturbations in the region of minimum closure gets harder the further we go. It is likely that as we zoom in we should be integrating for longer, or changing the grid-size for measuring closure. This should smooth out the borders between regions but increase computational time. Furthermore, it is likely by just zooming in to one region we will miss the optimal value. For that reason, employing a method like gradient descent may be much more effective, and should be the subject of further research.

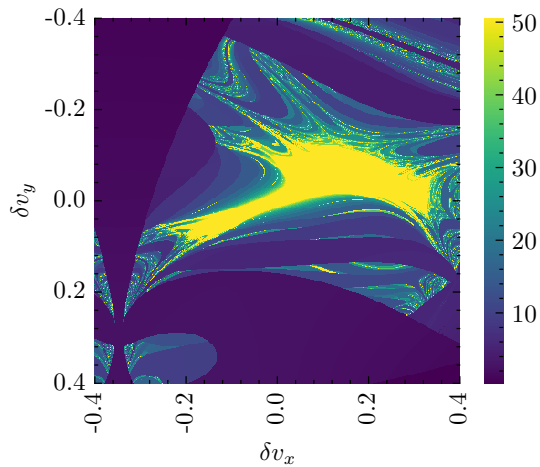


Figure 54: Escape times of perturbations of the figure-8 orbit, capped to 8 periods.

A question to be answered is: can we find other distinct orbits using a similar method? In Figure 54 the escape times are capped to 8 periods. It can be seen that there are perturbations away from the stable region that may be candidate regions of stable orbits. They might have smaller regions of stability and aren't so clear unless calculating on a very fine mesh size. This could be another subject of further research.

4.2.6 Stability of the Mass

As an extension, we can look at how the masses affect stability of the figure-8. By fixing one mass as $m'_2 = 1$ the other two are perturbed by $m'_1 = 1 + \delta m_1$ and $m'_3 = 1 + \delta m_3$. This lets us understand how any mass ratio $m_1 : m_2 : m_3$ affects the orbit. We integrate with initial velocities p_1 and p_2 as in initial conditions (4.1) and find the appropriate radius from equation (4.8). Galán et al. [10] suggests the region of stability for the masses is very small (10^{-4}), so we only look at a perturbation search area of this magnitude. We find the closure and escape times with identical parameters to section 4.2.4.

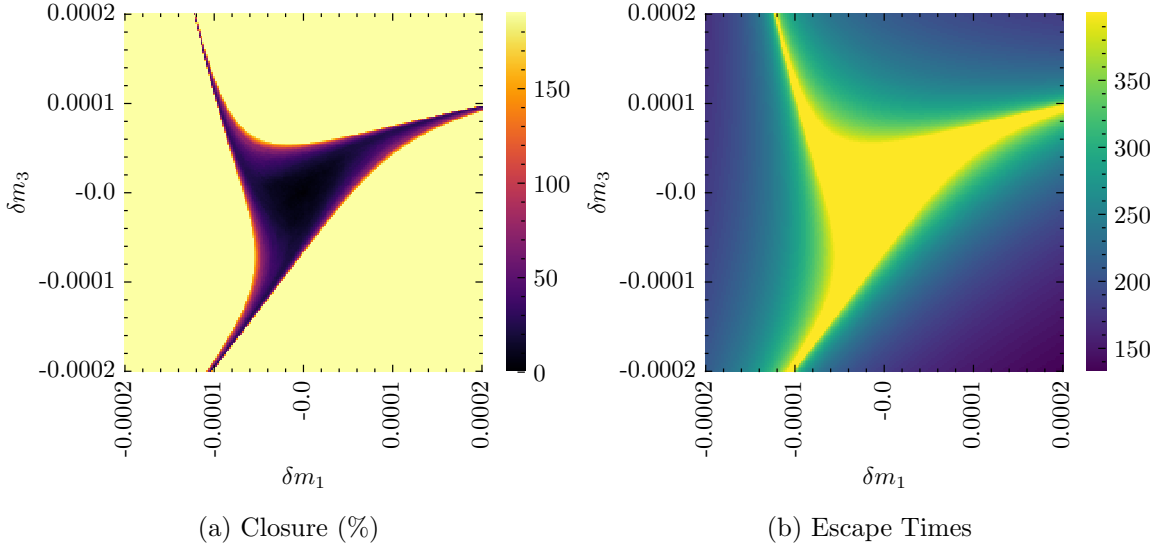


Figure 55: Stability of the masses of the figure-8 orbit.

Figure 55 shows a very distinct and small region of stability. As the masses move outside of this region, the orbit undergoes a bifurcation from stable to chaotic. The region of stability approximately agrees with Galán [10] but more thought ought to be put in to analysing this stability. For example, are the stopping parameters appropriate? Why not just fix one mass? With more time, questions like these should be answered.

Interestingly, the results of this means a figure-8 celestial system could exist, but under a very specific set of circumstances where all the bodies have approximately the same mass.

4.3 Stabilities of other Orbits

We want to see if the method used in section 4.2 can be applied to other periodic orbits, stable or unstable. This leads us to investigate the stability of both Euler and Lagrange's circular equal-mass solutions.

4.3.1 Euler's Solution

The perturbed initial conditions of Euler's solution can be written

$$\begin{cases} \mathbf{r}_1(0) = [-R, 0, 0]^T, & \mathbf{r}_2(0) = [0, 0, 0]^T, & \mathbf{r}_3(0) = [R, 0, 0]^T, \\ \mathbf{v}_1(0) = [\delta v_x, \omega + \delta v_y, 0]^T, & \mathbf{v}_2(0) = [0, 0, 0]^T, & \mathbf{v}_3(0) = [-\delta v_x, -\omega - \delta v_y, 0]^T, \end{cases} \quad (4.12)$$

where $\omega = \sqrt{5/4}$. These are picked such that the CM remains in place and R is calculated by equation (4.9). Due to the suspected instability, the integration may not be accurate up to many periods. Therefore, integration is stopped at $T = 50$ but the other stopping parameters are kept as in Section 4.2.4. Integration is done with $C = 0.2$ on a 51x51 search area with $-0.1 \leq \delta v_x, \delta v_y \leq 0.1$, yielding Figure 56.

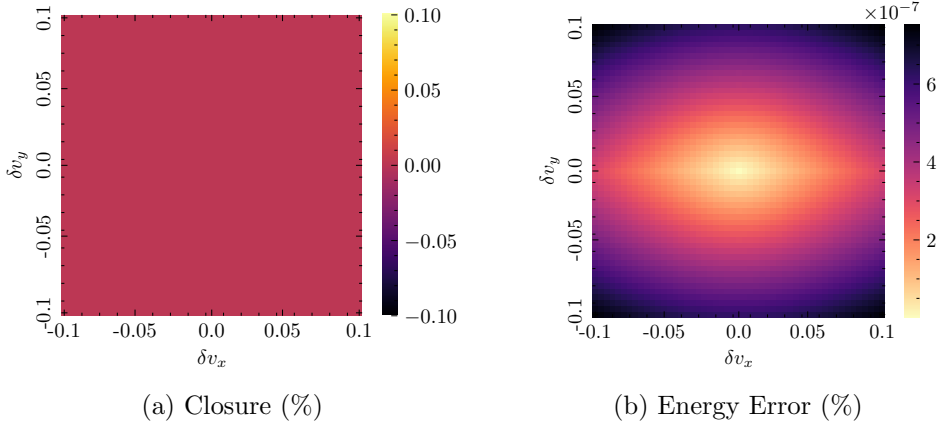


Figure 56: Stability of Euler's circular equal-mass solution.

Figure 56 is not the expected result. Every perturbation is closed, and the energy decreases toward the unperturbed orbit. This orbit could be considered stable, but we know it not to be. We can see what is happening at some of these perturbations and integrate them.

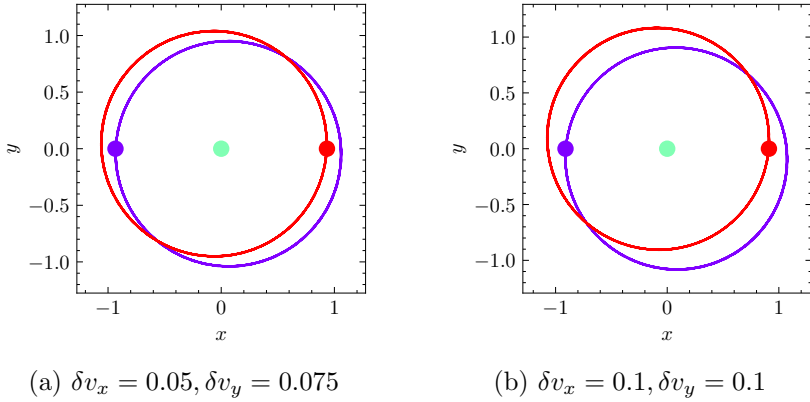


Figure 57: Trajectories of perturbations of Euler's circular equal-mass solution.

Figure 57 makes some sense of why the closures are equal - the masses are still admitting solutions to Euler's solution but are moving two separate circles. The masses stay in a line with the same distance ratios, so their measurement in shape space remains the same and therefore the closure too. Every integration is a variation of Euler's solution, so changing the stopping parameters is unlikely to have an effect. Considering small perturbations, but fixing $R = 1$ is likely to admit the same behaviour. The masses begin on the same line, so we are always going to get some variation of Euler's solution. Instead, we can perturb the masses off the line, and out of the Euler family of solutions. Let m_1 & m_3 make angles $\delta\theta_1$ & $\delta\theta_3$ with the negative and positive x -axis respectively. Then the initial conditions can be written

$$\begin{cases} \mathbf{r}_1(0) = [-R \cos \delta\theta_1, R \sin \delta\theta_1, 0]^T, & \mathbf{r}_2(0) = [0, 0, 0]^T, & \mathbf{r}_3(0) = [R \cos \delta\theta_3, R \sin \delta\theta_3, 0]^T, \\ \mathbf{v}_1(0) = [\omega \sin \delta\theta_1, \omega \cos \delta\theta_1, 0]^T, & \mathbf{v}_2(0) = [0, 0, 0]^T, & \mathbf{v}_3(0) = [\omega \sin \delta\theta_3, -\omega \cos \delta\theta_3, 0]^T, \end{cases} \quad (4.13)$$

where $\omega = \sqrt{5/4}$ and R is calculated with equation (4.9). Integration is done over $-0.01 \leq \delta\theta_1, \delta\theta_3 \leq 0.01$ on a 101x101 grid using the usual stopping parameters up to $T = 50$ and a mesh of 500x500 on the shape space.

Figure 58 shows more expected results. When the masses start collinearly, at $\delta\theta_1 = -\delta\theta_3$, the orbit is closed. When the masses aren't collinear, the closures are relatively very big, indicating a lack of periodicity. $\delta\theta_1 = -\delta\theta_3$ is an infinitesimally thin region, and any deviation from it gives

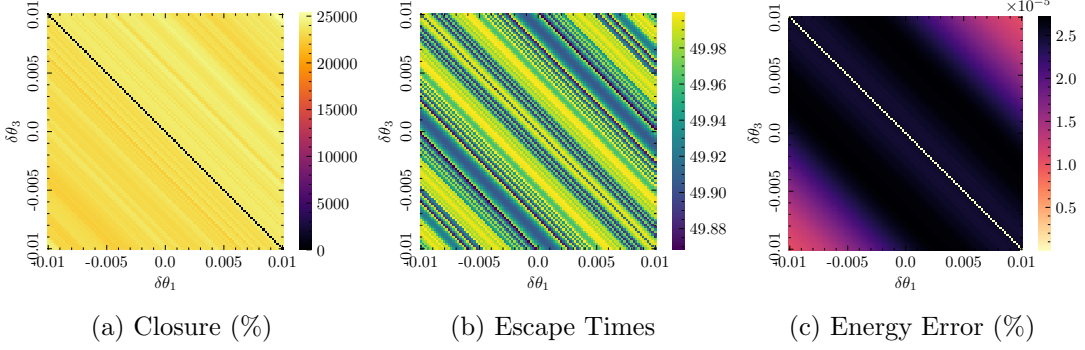


Figure 58: Stability of the collinearity of Euler's solution.

a non-closed orbit. Therefore, Euler's family of solutions is in fact unstable. The escape times don't tell us much, except for that most of the simulations complete integration. The energy error says that the region of least energy error is on the line of collinear solutions. Notice the symmetry about $\delta\theta_1 = -\delta\theta_3$ suggesting the orbit can be flipped and maintain its dynamics. T could be increased and other parameters changed, but these results suffice.

4.3.2 Lagrange's Solution

For Lagrange's solution, we can first see if the original method of perturbation works. However, we cannot perturb in quite the same way due to the different central configuration. Instead, we perturb by

$$\begin{cases} \mathbf{r}_1(0) = [0, R, 0]^T, & \mathbf{v}_1(0) = [\omega + \delta v_x, \delta v_y, 0]^T, \\ \mathbf{r}_2(0) = [-R \cos \frac{\pi}{6}, -R \sin \frac{\pi}{6}, 0]^T, & \mathbf{v}_2(0) = [-(\omega + \delta v_x) \sin \frac{\pi}{6}, (\omega + \delta v_y) \cos \frac{\pi}{6}, 0]^T, \\ \mathbf{r}_3(0) = [R \cos \frac{\pi}{6}, -R \sin \frac{\pi}{6}, 0]^T, & \mathbf{v}_3(0) = [-(\omega + \delta v_x) \sin \frac{\pi}{6} + \delta v_x, -(\omega + \delta v_y) \cos \frac{\pi}{6}, 0]^T, \end{cases} \quad (4.14)$$

where $\omega = 3^{-1/4}$. This perturbs the spin ω in the resolved directions for each body. Due to the change in potential energy, R needs to be calculated by

$$R = \frac{\sqrt{3}}{K'_0 - E_0}. \quad (4.15)$$

Recall that in figure 36 Lagrange's solution only completes 7 periods. We want to stop before this, so pick $T = 40$. The value $C = 0.2$ performed well for Euler's solution, so this is used again. We perform the stability search on a 201x201 grid where $-0.01 \leq \delta v_x, \delta v_y \leq 0.01$ and the remaining parameters the same as Euler's solution, giving figure 59.

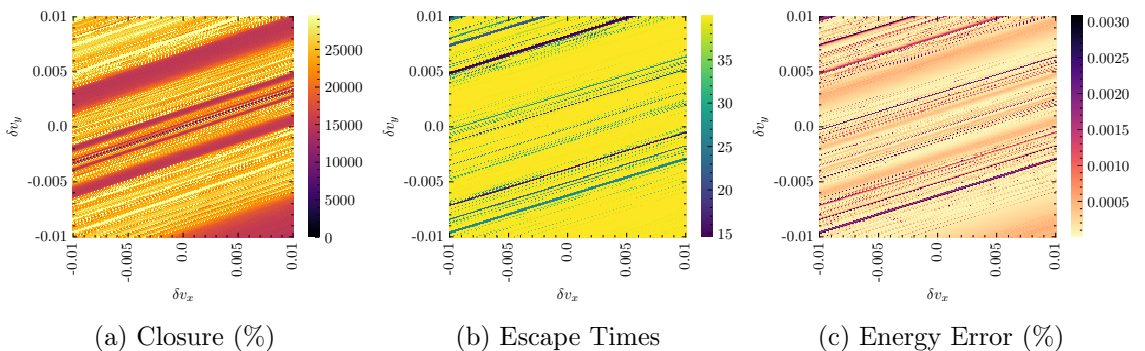


Figure 59: Stability of Lagrange's circular equal-mass solution.

Unlike Euler's solution, not all the perturbations are closed. In fact, there is a line of closed orbits given by picking the right relationship between δv_x and δv_y . The escape times are different too. Not every perturbation completed integration to $t = 40$ and for those that did not the energy error is high. The evidence points to Lagrange's solution being unstable, and more unstable than Euler's solution.

Much like Euler's solution, we can also investigate what happens when the masses are moved from being vertices of an equilateral triangle. The first mass is fixed in place at $[0, R, 0]^T$, then the remaining two masses make angles $2\pi/3$ around the circle. The angle be perturbed by $\delta\theta_2$ and $\delta\theta_3$ to give new initial conditions

$$\begin{cases} \mathbf{r}_1(0) = [0, R, 0]^T, & \mathbf{v}_1(0) = [\omega + \delta v_x, \delta v_y, 0]^T, \\ \mathbf{r}_2(0) = [-R \cos(\frac{\pi}{6} + \delta\theta_2), -R \sin(\frac{\pi}{6} + \delta\theta_2), 0]^T, & \mathbf{v}_2(0) = [-\omega \sin(\frac{\pi}{6} + \delta\theta_2), \omega \cos(\frac{\pi}{6} + \delta\theta_2), 0]^T, \\ \mathbf{r}_3(0) = [R \cos(\frac{\pi}{6} + \delta\theta_3) - R \sin(\frac{\pi}{6} + \delta\theta_3), 0]^T, & \mathbf{v}_3(0) = [-\omega \sin(\frac{\pi}{6} + \delta\theta_3), -\omega \cos(\frac{\pi}{6} + \delta\theta_3), 0]^T, \end{cases} \quad (4.16)$$

where $\omega = 3^{-1/4}$. Once again, R can't be easily calculated quite in the same way - for ease of calculation we let $R = 1$ and only consider small perturbations $-0.01 \leq \theta_2, \theta_3 \leq 0.01$ then the energy should be approximately the same.

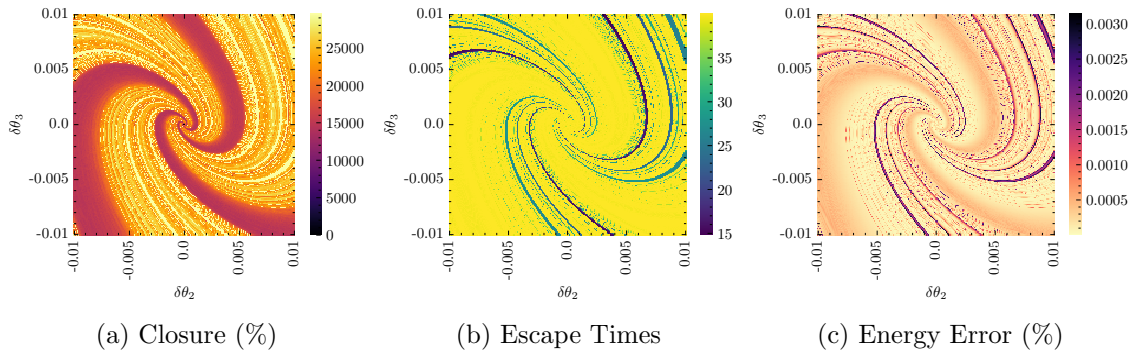


Figure 60: Stability of the triangular configuration of Lagrange's solution.

Figure 60 shows the results of changing the central configuration. Spirals of large closures come out from the central, unperturbed orbit. In fact, the only closed orbit is the unperturbed one. The masses have to be on an equilateral triangle to give a periodic solution, and anything else admits chaotic behaviour. In other words, the configuration is unstable. The escape times suggest $T = 40$ may have not been high enough, but this is a fine line.

When changing the configuration of Euler's solution we get a line of closed orbits, but when changing the configuration of Lagrange's solution we get a single point. In this sense, Lagrange's solution could be considered more unstable than Euler's.

It is clear that this method of perturbing and calculating closure works well for stable solutions, but really more thought needs to be put into the unstable solutions. For that reason, other definitions of stability should be considered, and we turn to looking at the Lyapunov stability.

5 Maximum Lyapunov Exponent

5.1 Definition of Stability

To learn more about the stability of an orbit, we are interested in the rate of separation of infinitesimal perturbations from the unperturbed orbit. In other words, we want to determine its Lyapunov stability, or the maximum Lyapunov exponent (MLE) [16, 31, 21, 18]. Two trajectories, with initial perturbation δ_0 , separate according to

$$\|\delta(t)\| = e^{\lambda t} \|\delta_0\|, \quad (5.1)$$

where λ is the Lyapunov Exponent and $\|\cdot\|$ is some distance metric, typically the distance in ‘phase space’. How we pick the initial perturbation direction may impact the rate of separation. Therefore, there is a spectrum of Lyapunov exponents (exactly the number of dimensions in the system) and a largest exponent, the MLE. Most initial separations will contain a component in the MLE direction, so over a long-enough time this becomes the dominating behaviour [18, 31]. Hence, we estimate the MLE using

$$\lambda = \lim_{t \rightarrow \infty} \ln \frac{\|\delta(t)\|}{\|\delta_0\|}. \quad (5.2)$$

For a stable periodic orbit, we expect linear growth in equation (5.1), so that $\lambda = 0$. For an unstable orbit, we expect exponential growth, so that $\lambda > 0$. An asymptotically stable solution to the dynamical system would have $\lambda < 0$ [16] but we do not consider these.

5.2 Measuring the Separation

To measure the MLE of an orbit, we need an appropriate way of calculating the separation $\|\delta(t)\|$ at any time. Let a prime denote the perturbed trajectory, then there are a few possibilities that come to mind:

- Euclidean distance between positions of m_1 , $\|\delta\| = |\mathbf{r}_1 - \mathbf{r}'_1|$;
- Euclidean distance between velocities of m_1 , $\|\delta\| = |\mathbf{v}_1 - \mathbf{v}'_1|$;
- Difference in step size, $\|\delta\| = |h - h'|$;
- Euclidean distance in phase space, $\|\delta\| = |\mathbf{w} - \mathbf{w}'|$, where $\mathbf{w} = [r_{x1}, r_{y1}, \dots, r_{zN}, v_{x1}, \dots, v_{zN}]^T \in \mathbb{R}^{6N}$ is a vector of all the positions and velocities in all directions, and r_{xi} denotes the x -position of the i -th mass for $i = 1, \dots, N$.

In the three-body system (2.3) we randomly pick a small perturbation in the 18-dimensional space. This vector should be small relative to the size of the orbit, so a magnitude of 10^{-6} is appropriate when compared to the size of our orbits. Furthermore, we are only interested in the behaviour when the two trajectories are close. Thus, we integrate up to a separation of order 10^{-2} . As a test case, we use the figure-8, for which linear growth is expected. Figure 62 shows that $C = 0.065$ gives a maximum energy error of order 10^{-8} over 300 periods, which is sufficiently small when compared to the perturbation size.

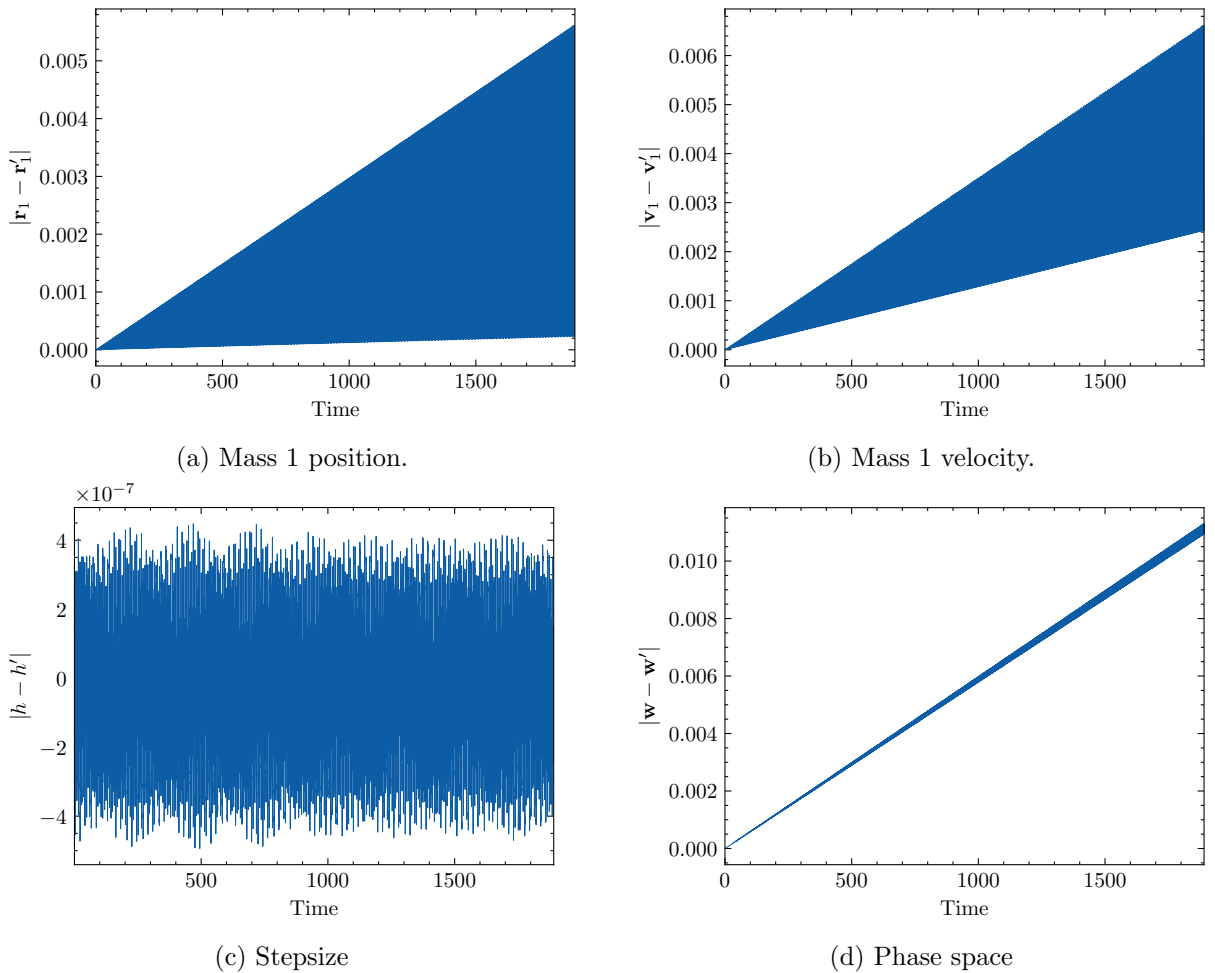


Figure 61: Separation of the figure-8 orbit and a small perturbation of order 10^{-6} , with different distance metrics.

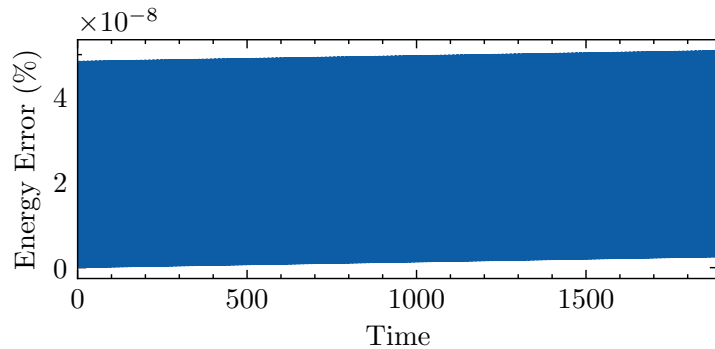


Figure 62: Energy error of 300 orbits of the figure-8, with $C = 0.065$.

Figure 61 shows the time-evolution of measuring the separation of the unperturbed figure-8 and its perturbation over 300 periods. The step size metric appears to be the worst, being periodic. Measuring the position or velocity difference of one mass shows linear growth but with periodic variation. The phase space distance is promising, however it comes with a caveat: position and velocity have different units, so directly calculating the Euclidean distance isn't entirely accurate. Instead, we ought to non-dimensionalise the positions and velocities. To do this, find the maximum position and velocity, in any direction, over one period:

$$\begin{cases} r_m = \max r_{x1}(t_0), r_{x1}(t_1), \dots, r_{x1}(t_n), r_{y1}(t_0), \dots, r_{y1}(t_n), \dots, r_{z3}(t_0) \dots r_{z3}(t_n), \\ v_m = \max v_{x1}(t_0), v_{x1}(t_1), \dots, v_{x1}(t_n), v_{y1}(t_0), \dots, v_{y1}(t_n), \dots, v_{z3}(t_0) \dots v_{z3}(t_n). \end{cases} \quad (5.3)$$

Then \mathbf{w} becomes

$$\mathbf{w} = \left[\frac{r_{x1}}{r_m}, \frac{r_{y1}}{r_m}, \dots, \frac{r_{zN}}{r_m}, \frac{v_{x1}}{v_m}, \frac{v_{y1}}{v_m}, \dots, \frac{v_{zN}}{v_m} \right]^T \in \mathbb{R}^{6N} \quad (5.4)$$

and \mathbf{w}' is adjusted in the same way. The Euclidean distance $|\mathbf{w} - \mathbf{w}'|$ is now unit-less and much more useful. Note that r_m and v_m take one value and their exact accuracy is not too important to non-dimensionalise. For the figure-8 they are found to be $r_m = 1.06$ and $v_m = 1.19$.

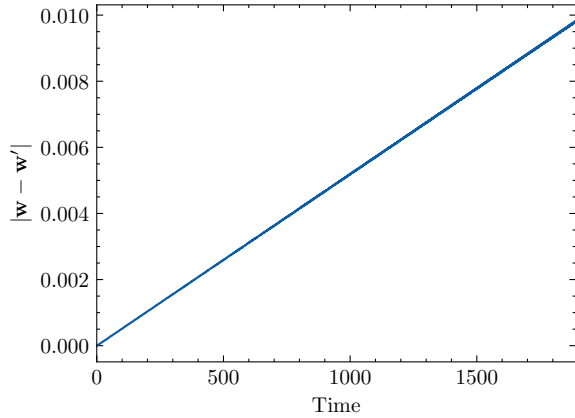


Figure 63: Euclidean distance between the figure-8 orbit and a small perturbation of order 10^{-6} , in the adjusted phase space.

The results of this adjusted distance measure are seen in figure 63. It shows a linear divergence between the trajectory of the unperturbed figure-8 and the perturbed orbit, with no periodic variation. Naturally, the limit of this gives $\lambda = 0$ and therefore the figure-8 is indeed Lyapunov stable, agreeing with the conclusion made in section 4.2.4.

Other measures of separation could be considered, such as the Euclidean distance of all the positions or velocities. However, this adjusted phase space distance encompasses the entire system and seems to do a good job. This measure of the Lyapunov exponent can now be applied to the other orbits seen throughout this thesis.

5.3 The Figure-8

It would be interesting to see if Lyapunov stability is in agreement with the stability region found in section 4. To do this, we look at the separation of a few perturbations of the figure-8. These are: a stable orbit close to the unperturbed figure-8, with $\delta v_x = 0.01$ & $\delta v_y = 0.01$; a stable but not so close orbit with $\delta v_x = 0.15$ & $\delta v_y = 0.05$; an unstable perturbation with $\delta v_x = -0.2$ & $\delta v_y = 0.2$; and Moth I. The unstable figure-8 perturbation is picked such that it highlights the unstable separation behaviour. The stable orbits are both shown in figure 42 - we expect the closer orbit to be more stable than the outer orbit.

The initial conditions are integrated from initial perturbation size 10^{-6} to 10^{-2} . A value of $C = 0.01$ is used to minimise the energy error to an order less than 10^{-8} . For each initial condition, the r_m and v_m are found from integration of one period, and stated in figure 64.

Figure 64 shows that the orbits thought to be stable exhibit linear growth, and are therefore Lyapunov stable. Notice that it takes Moth I much longer to reach a separation of 10^{-2} and the closer figure-8 perturbation takes longer than the farther perturbation. A conclusion could be drawn that the more shallow a gradient, the more stable the orbit is. However, Moth I has a $v_m = 3.47$ which scales the phase space distance down more than the other orbits, so a direct comparison between any combination is not fair.

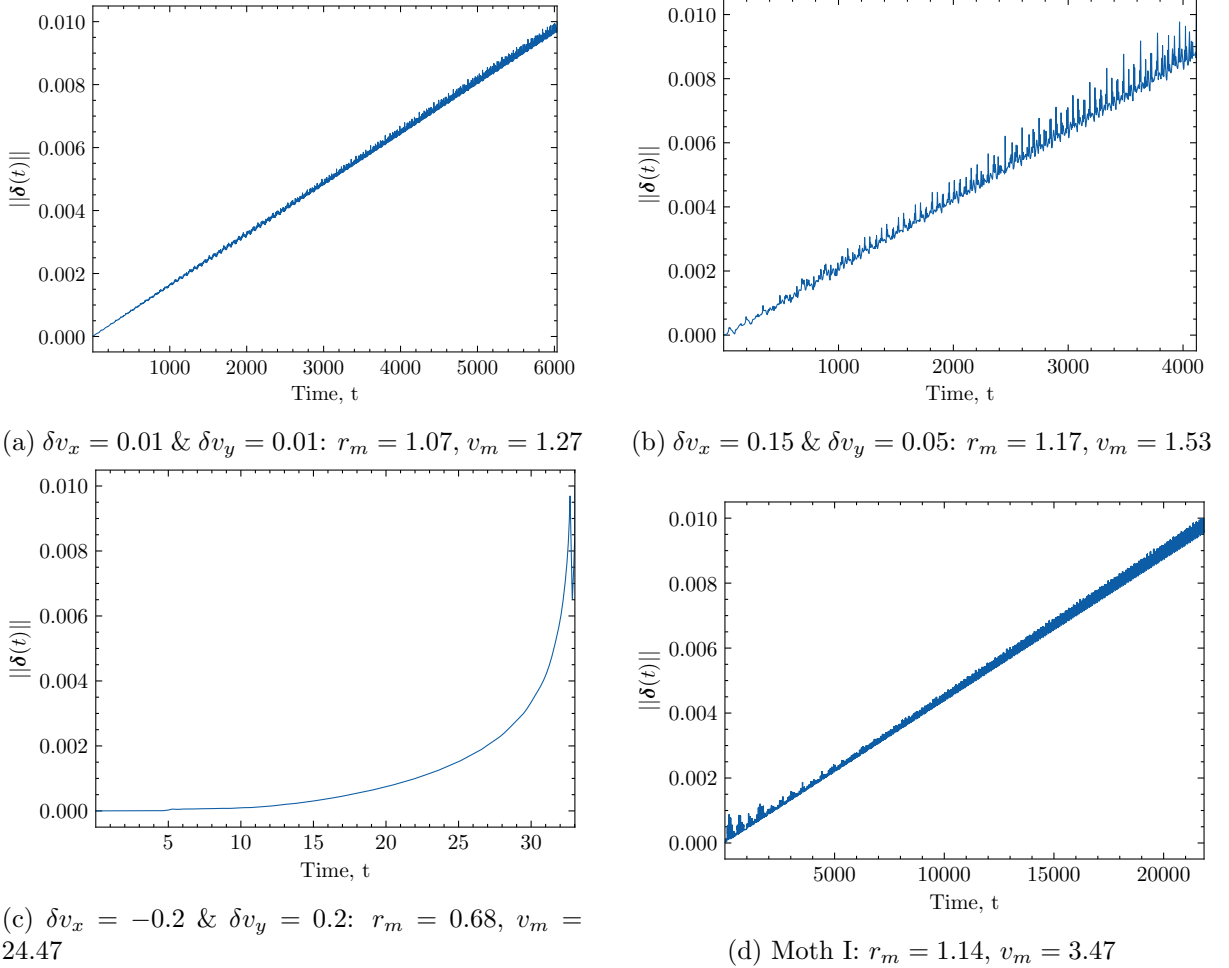


Figure 64: Separation of small perturbations of nearby orbits to the figure-8.

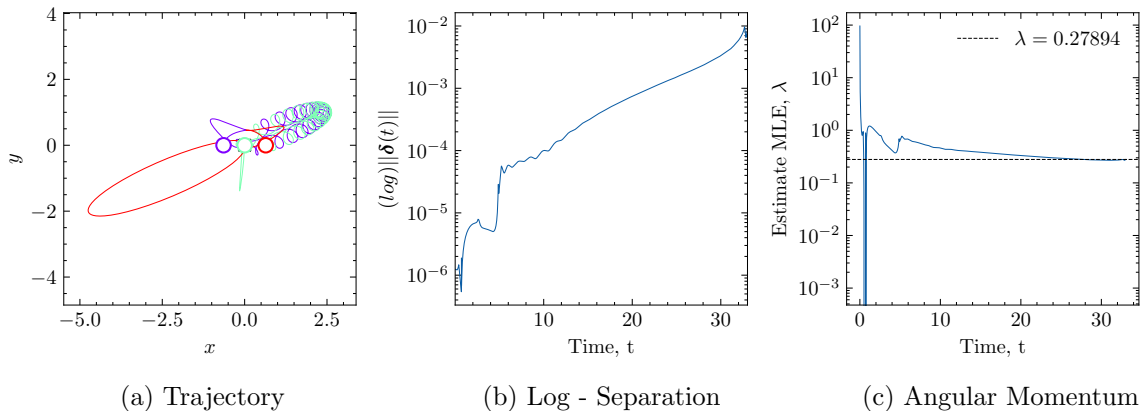


Figure 65: Analysis on the unstable orbit. $\delta v_x = -0.2 \& \delta v_y = 0.2: r_m = 0.68, v_m = 24.47$

The unstable case looks exponential, but we can't be certain. Instead, we explore further, as shown in figure 65. The separation is messy until order 10^{-4} , but then reveals linear growth on the log scale. The MLE can be estimated by equation (5.2) at $\lambda = 0.28 > 0$. Therefore, the growth is exponential, and this unstable choice is also Lyapunov unstable.

It is seen, at least for this choice of orbits, that Lyapunov stability agrees with the region of stability for the figure-8. For unstable orbits, the Lyapunov exponent gives a direct value as to how unstable an orbit is. In contrast, using the MLE to determine which orbits are more stable than others requires more work. With more time, it would be intriguing to measure the MLE over a whole search-area of perturbations of the figure-8, to see if the two definitions of stability completely agree. This is a computationally heavy task - integration is required to be highly accurately ($C = 0.01$) over many periods to see the long-term effects. Instead, we turn our eye to analysing unstable orbits with the MLE, i.e. Euler and Lagrange's solutions.

5.4 Euler and Lagrange's Solutions

Section 4.3 showed that both Euler and Lagrange's solutions are unstable. We are interested in how unstable they are and whether we can use the MLE to quantify this. They are grouped together to make a direct comparison.

5.4.1 Initial Investigation

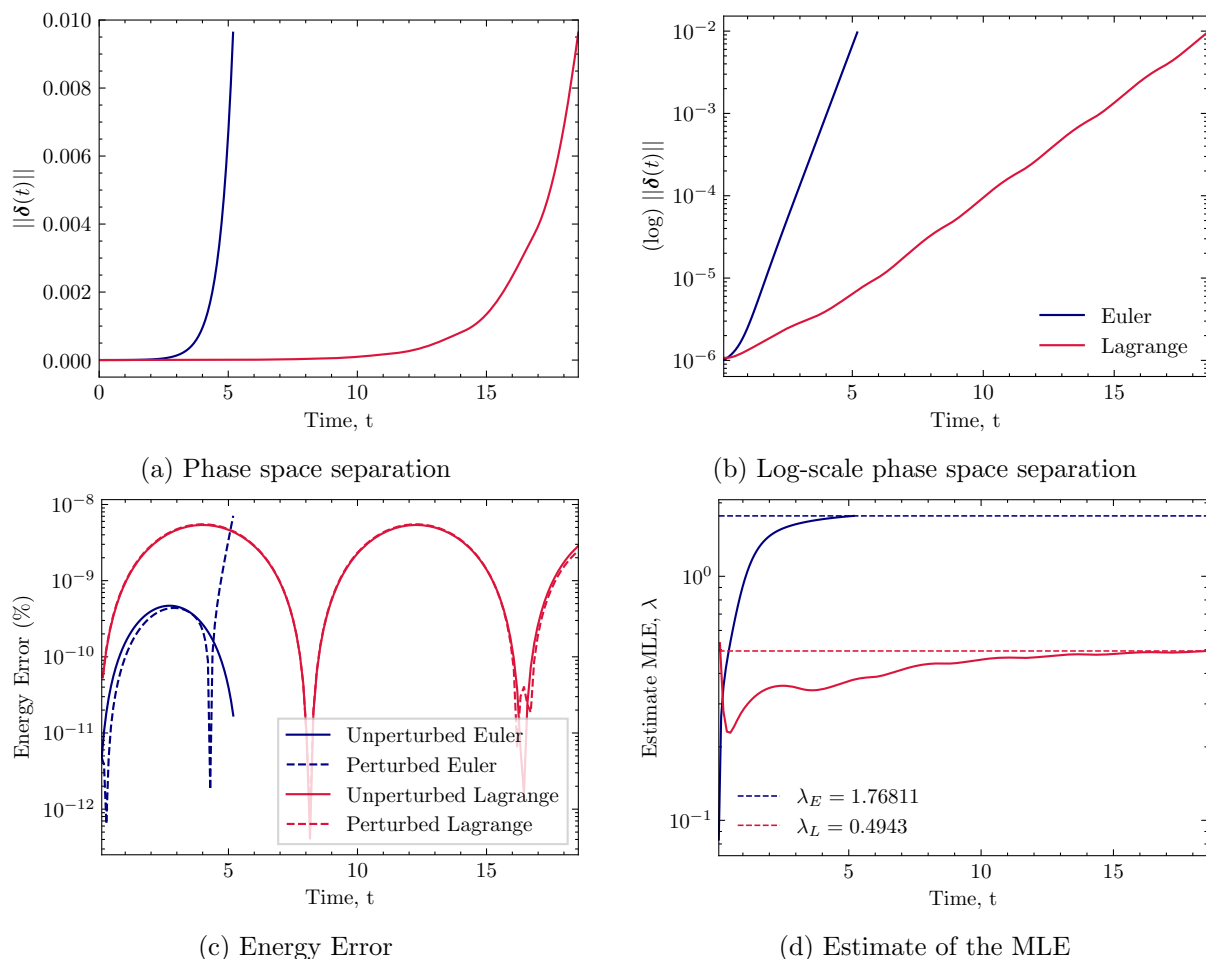


Figure 66: Separation of Euler and Lagrange's circular equal-mass three-body solutions.

As before, we integrate from 10^{-6} to 10^{-2} , and look at the rate of separation using the adjusted phase space distance. It is found that Euler's orbit has $r_m = 1.0$ and $v_m = \omega_E = 1.12$, and Lagrange's orbit has $r_m = 1.0$ and $v_m = \omega_L = 0.76$. A value of $C = 0.1$ is used to calculate to an accuracy of 10^{-8} , as seen in figure 66c.

In figure 66a perturbations of both Euler and Lagrange's orbits appear to separate exponentially. On a log-scale (figure 66b) both are linear, confirming exponential growth. The MLE is estimated in figure 66d using equation 5.2. Euler's solution has an MLE of $\lambda_E = 1.76811$ and Lagrange's solution has $\lambda_L = 0.49430$. This implies that both are Lyapunov unstable, but Euler's solution is actually more unstable than Lagrange's solution, in disagreement with the results found in section 4.

This could be for a number of reasons: we are now considering perturbations in the z -direction; the random perturbation doesn't contain the MLE (unlikely); the energy error is too high; the integration is not long enough, though both seem to be admitting almost limiting behaviour. Therefore, it makes sense to verify and re-calculate the MLE for a number of different perturbations.

5.4.2 Distribution of the MLE

We repeat 10000 iterations of the experiment, yielding Figure 67. A value of $C = 0.01$ is used to give energy errors of order 10^{-12} , ensuring precise results. In Figures 67a & 67b every simulation exhibits exponential growth, so we confirm that both orbits are unstable for many perturbations. The limiting MLE is found for every simulation and distribution is plot in figures 67e & 67f. The results of the distribution are summarised in table 6.

Both distributions are skewed to the right, which tells us the modal value for λ is more important. Therefore, the MLE of Euler's solution is found to be $\lambda_E = 1.83$, which is much higher than Lagrange's solution at $\lambda_L = 0.51$. The conclusion is that Euler's solution is more unstable than Lagrange's solution, in the Lyapunov sense.

Further research could involve calculating the MLE of different mass ratios of Euler and Lagrange's solution's. For example, Lagrange's solution is deemed to be stable when one mass is much larger than the others [23]. The MLE could be applied to see if this really is the case.

	Mean	Mode	Variance
Euler, λ_E	1.74117	1.82625	0.02470
Lagrange, λ_L	0.52909	0.51489	0.00095

Table 6: Distribution of the MLE over 10000 simulations of the Euler and Lagrange orbits.

5.4.3 An issue with Randomness

The skew-ness of the distribution indicates something may be wrong with the random selection of perturbations. In the simulations, we pick a random perturbation by the following method:

- Uniformly select a value between -1 and 1 in each direction, $\delta_k \sim U(-1, 1)$ for $k = 1, \dots, 6N$,
- normalise the random direction $\hat{\boldsymbol{\delta}} = \frac{\boldsymbol{\delta}}{\|\boldsymbol{\delta}\|}$,
- scale the unit random direction to $10^{-6} \cdot \hat{\boldsymbol{\delta}}$,
- recover the perturbed initial conditions $\mathbf{w}' = \mathbf{w} + 10^{-6} \cdot \hat{\boldsymbol{\delta}}$.

There is a problem with this: in scaling down the uniform distribution, certain directions are more common than others. The issue is exaggerated in figure 68. In the xy plane, the corners gather more perturbations. As a result, in our system the 18 dimensional corners will collect more perturbations. It is likely that this may impact the shape of the distribution, but is unlikely it will change the modal value as the direction of the MLE will be captured by most perturbations.

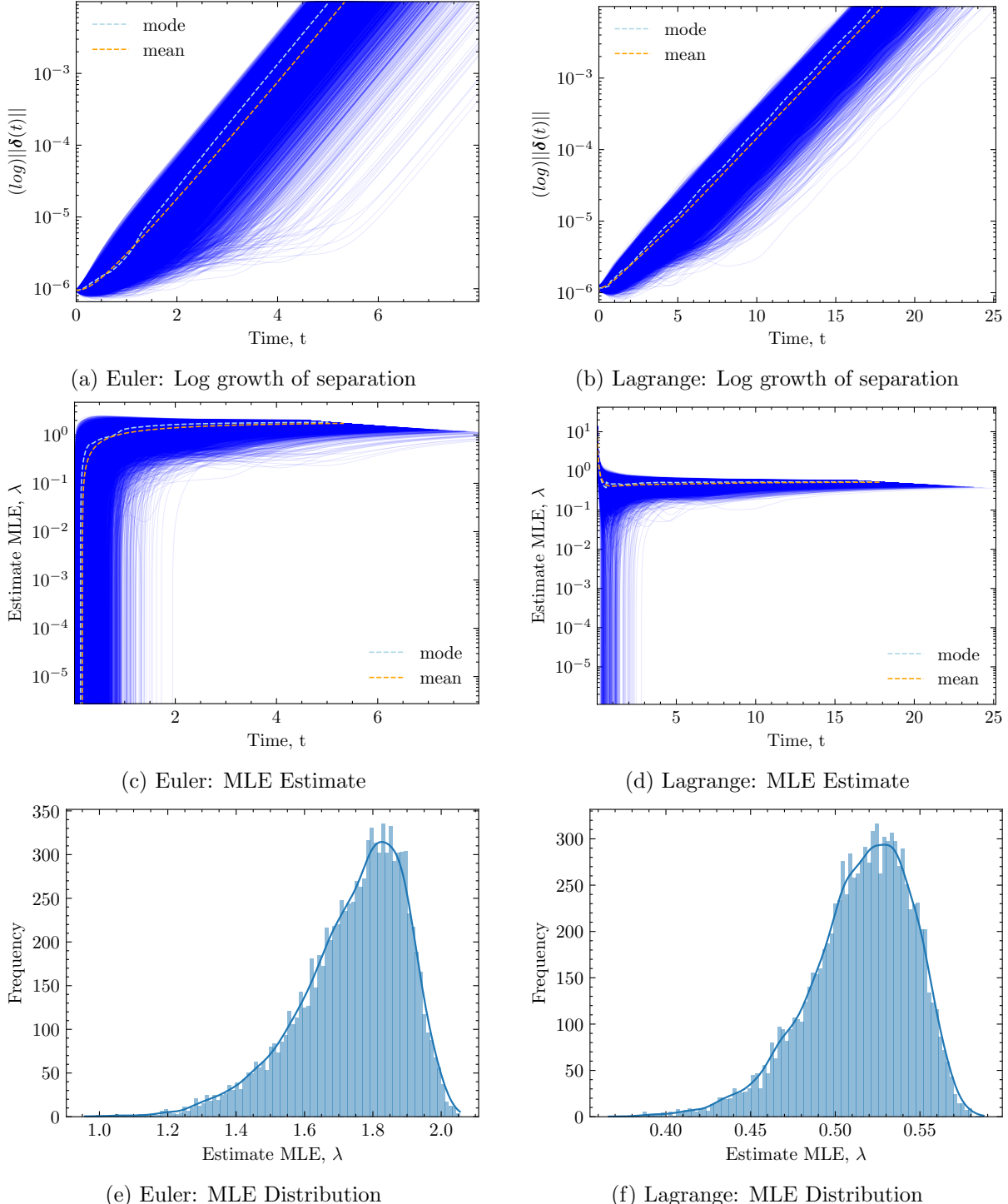


Figure 67: 10000 estimations of the MLE of Euler and Lagrange's circular equal-mass three-body solutions.

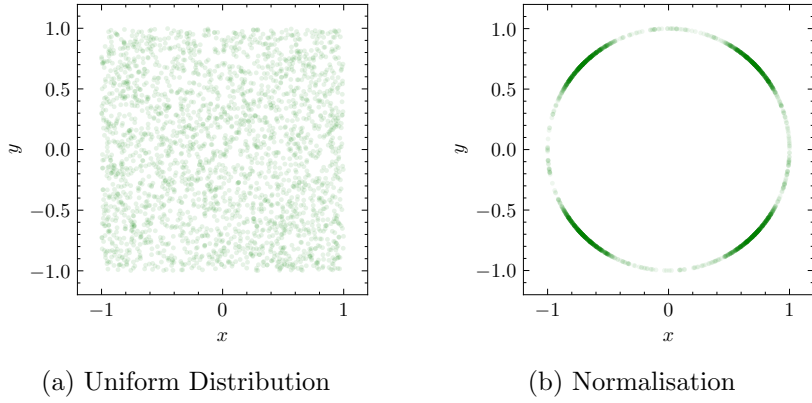


Figure 68: Uniformly distributed perturbations in the xy -plane.

We test whether this randomness needs changing by rotating the initial conditions about the CM, so that the bodies start in or out of the corners. Euler's solution is rotated by $\pi/4$ and Lagrange's by $\pi/8$. Re-calculating the distribution over 2000 simulations gives figure 69 and table 7. It can be seen that the distribution approximately remains the same, as do the modal, mean and variance values. Therefore, this method of generating random perturbations is valid.

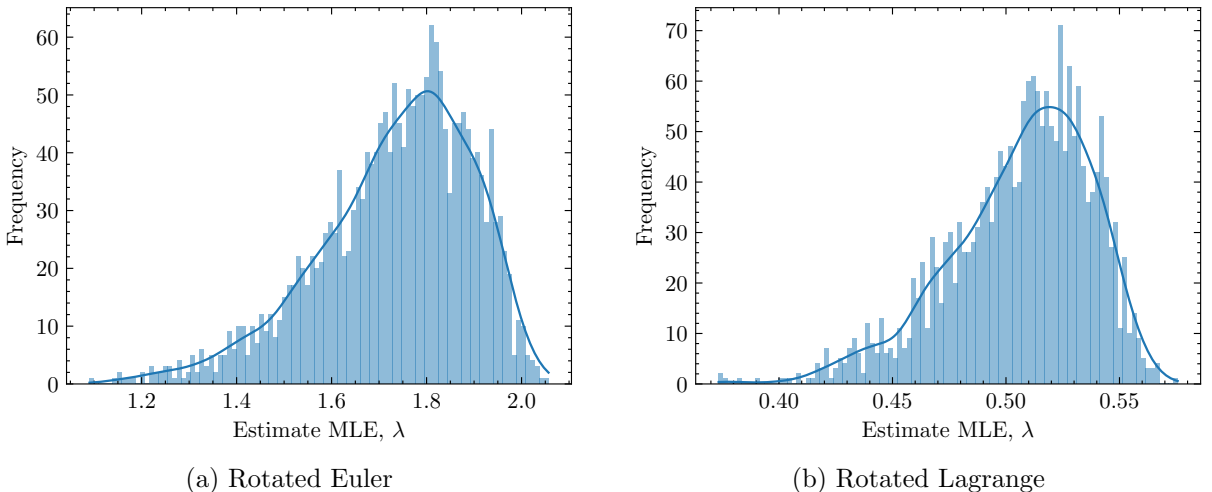


Figure 69: 2000 estimations of the MLE of rotated Euler and Lagrange's solutions.

	Mean	Mode	Variance
Euler, λ_E	1.73400	1.80229	0.02636
Lagrange, λ_L	0.50047	0.51916	0.00097

Table 7: Distribution of the MLE over 2000 simulations of the rotation Euler and Lagrange orbits.

5.5 N-body Choreographies

As previously discussed, there exist choreographic solutions to the N-body problem where each body follows the same path, phase shifted by T/N . The figure-8 and Lagrange's circular solution are examples of 3-body choreographies. Now we have access to Lyapunov exponent analysis, it can be used to investigate the stability of some N-body choreographies.

Lagrange's 3-body solution can be extended to N-bodies moving round a circle: By placing N bodies equidistant round a circle of radius one, the initial conditions are given by

$$\mathbf{r}_i(0) = [\cos \frac{2i\pi}{N}, \sin \frac{2i\pi}{N}, 0]^T, \quad \mathbf{v}_i(0) = [\omega \sin \frac{2i\pi}{N}, -\omega \cos \frac{2i\pi}{N}, 0]^T, \quad (5.5)$$

for $i = 1, \dots, N$. Using equation 4.2, the angular velocity ω can be found by equating the force on one body to the centrifugal force, so that $\omega = \sqrt{|\mathbf{F}_1|}$. Then the choreography has period $T = 2\pi/\omega$. The 4 and 5 circles are integrated with $C = 0.1$ until forced to stop.

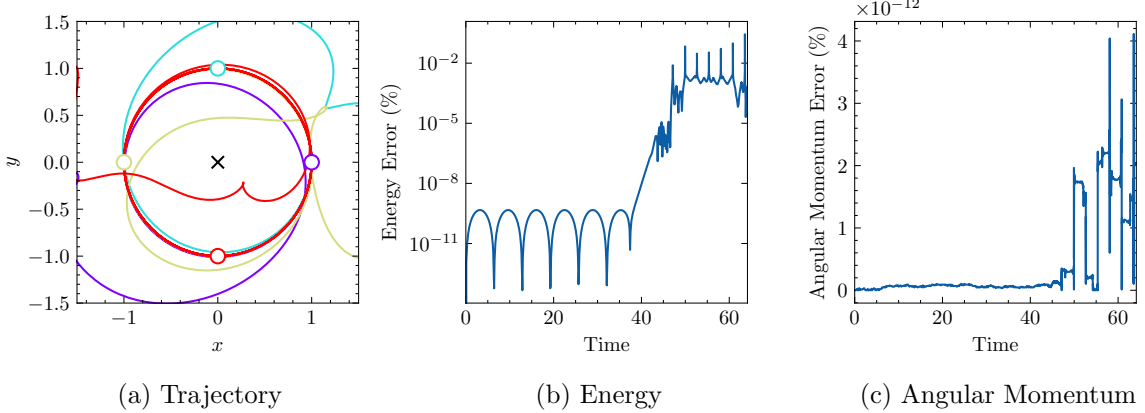


Figure 70: Integration of the 4-circle, with $C = 0.1$.

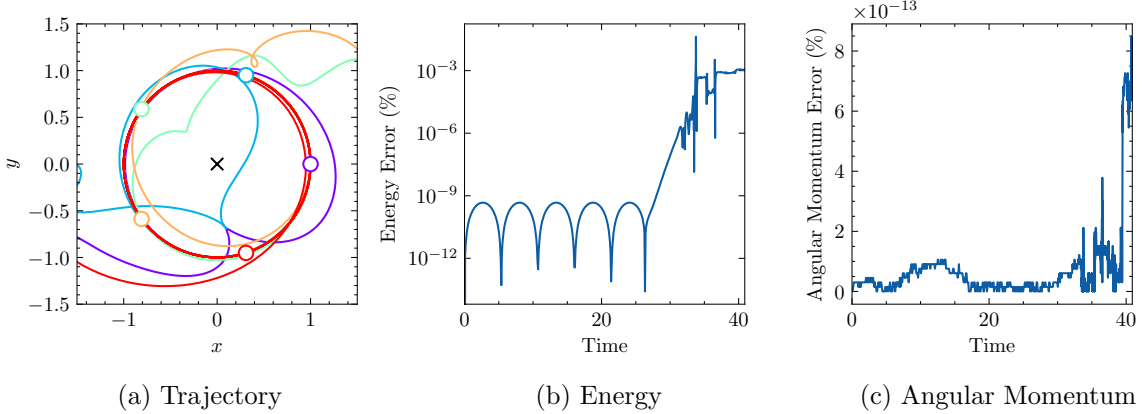


Figure 71: Integration of the 5-circle, $C = 0.1$.

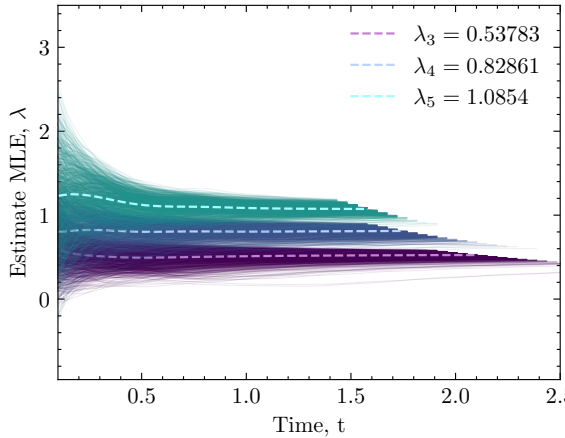
Figures 70 & 71 shows the 4-circle completes six periods before admitting chaotic behaviour, whereas the 5-circle only completes five periods. In addition, it has previously been seen that the 3-circle completes seven periods (Figure 35). This suggests that the more bodies added to the circle, the more unstable it becomes. Can we use the MLE to confirm it?

We generate 1000 estimates of the MLE, λ_N , for every N -circle. To avoid taking the mean of a skewed distribution, we use the modal value. Figure 72a shows the limiting MLE estimation for the 3, 4 and 5 circles. As expected, the 5-circle is more unstable than the 4-circle, which is more unstable than Lagrange's 3-circle solution. Figure 72 shows that the MLE does indeed increase the more bodies we add to the circle, up to $N = 20$.

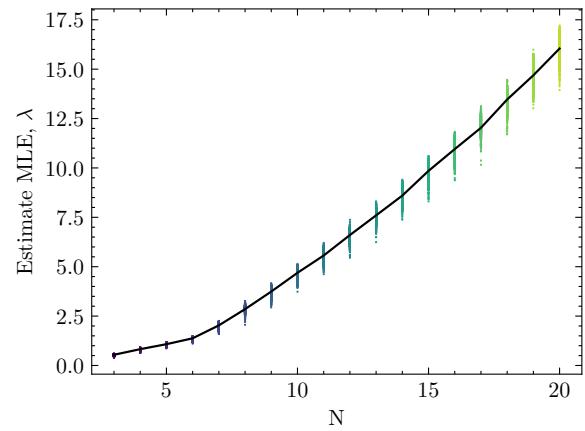
This is just one demonstration of how the MLE can be used to compare the instability of N -body orbits. This method could be applied to any selection of N -body orbits, providing a lot of substance in future research.

5.6 Extensions of the MLE

Accurately calculating the MLE of Euler and Lagrange's solution required many simulations of lots of random perturbations. This is obviously very inefficient, and using less computational power would be ideal. Furthermore, calculation of the Lyapunov spectrum would allow more



(a) Estimate MLE of the 3,4 and 5 Circles



(b) Estimate MLE against N

Figure 72: 1000 estimates of the MLE for the N-circle, with $3 \leq N \leq 20$.

insight in to the ways our orbits are unstable. For this, we look at alternative methods of calculating the MLE. One such method was suggested by Wolf [31] in 1985. A summary of the method is as follows:

- Integrate the unperturbed and perturbed trajectory until the separation gets too big,
- measure the MLE,
- scale the separation back down.
- repeat a large number of times,
- calculate the long-term average of the MLE.

The primary issue with this method is it requires very long-time calculation to be accurate. Margaris et al. [18] compares Wolf's algorithm to other algorithms that work on the time-series, known as BASGEN (dataBASe GENeration) and fixed evolution time (FET). Furthermore, Musilek and Quarles [23] suggest that the Fast Lyapunov Indicator (FLI) and the Mean Exponential Growth Factor of Nearby Orbits (MEGNO) methods can be used in the context of the N-body problem.

A natural extension to this section would be to apply some of these methods to the 3-body solutions discussed throughout this thesis. An accurate and fast MLE calculator could then be applied to real-life N-body orbits, such as our Solar system or the James-Webb telescope in L_2 of CR3BP.

6 Conclusions

The primary goal of this thesis is to analyse the stability of a select number of three-body orbits, namely the figure-8, Euler and Lagrange orbits. The intention is to learn more about the dynamics of the three-body problem and its solutions and to provide a framework for analysing stability.

To do this, first an effective numerical scheme is needed to integrate the N-body equations, forward or backward in time. In section 3 it was shown that a symplectic, fourth-order, Forest-Ruth integrator known as PEFR provides accurate solutions to the two-body equations and is better suited than other more common integrators like Leapfrog and RK4. Furthermore, the scheme is made more efficient by a tailored, time-adaptive step size modification, allowing for the calculation of hyperbolic interactions between bodies. This integrator can be used on any N-body system, such as our solar system!

In section 4, the time-adaptive PEFR accurately integrated the three-body orbits and its perturbations. By carefully integrating perturbations of the figure-8 orbit, a region of periodic figure-8-like solutions is found. Through measuring the closure of these perturbed orbits, it was shown that the figure-8 orbit is indeed stable. In the process of doing so another, but already known, stable orbit is found, known as ‘Moth I’. With more work, and utilising optimisation algorithms such as ‘gradient descent’, it is suspected that similar orbits could be found.

In addition, by perturbing Euler and Lagrange’s solutions away from the central configurations, they are shown to be unstable. However, more work needs to be done in determining which perturbations are appropriate.

In section 5, the maximum Lyapunov exponent was used to quantify the stability of these orbits. A small perturbation of the figure-8 orbit was shown to linearly separate from the figure-8, suggesting that the figure-8 is indeed Lyapunov stable. Further analysis demonstrated that the Lyapunov stability agreed with the prior region of stability.

Accurate estimates were made of the maximum Lyapunov exponent (MLE) for both Euler and Lagrange’s orbits. These estimates categorise their orbits as unstable, with Euler’s solution more unstable than Lagrange’s. Estimating the MLE to a high precision was computationally expensive, so more research should be done to in applying existing and efficient MLE estimators to the N-body problem.

Lastly, a demonstration was made on how the Lyapunov exponent can be used to analyse the stability of N-body orbits, specifically N-body choreographies. Finding and analysing the stability of these choreographies provides another place of research.

Although stability analysis has only been made on select 3-body orbits, the methodology can be applied to a range of N-body celestial mechanics. For example, building a region of stability around a satellite in Earth’s orbit would show if were a more stable location, saving fuel in course-correction. Calculating the Lyapunov exponent of exoplanets would be a marker of their suitability. A highly relevant and interesting avenue to take this research would be to go back to where it all started and apply the discussed techniques to real life planetary interactions, e.g. what is the Lyapunov stability of our solar system? Just how stable are the Lagrange points of Earth? And what are the consequences of an unstable Lyapunov exponent for the Earth and the thousands of satellites that circle it every day.

This thesis has only just touched the surface of the three-body problem and provided an overview in terms of stability. However, there is plenty to look at now the right tools have been developed.

References

- [1] U. M. Ascher and L. R. Petzold. *Computer methods for Ordinary Differential Equations and Differential-Algebraic Equations*. SIAM, 1998.
- [2] Bruns. Über die integrale des vielkörper-problems. *Acta*, 11:25–96, 1887.
- [3] J. C. Butcher. On Runge-Kutta processes of high order. *Journal of the Australian Mathematical Society*, 4(2):179–194, 1964.
- [4] C. L. Ernst Hairer, Gerhard Wanner. *Geometric Numerical Integration, Structure-Preserving Algorithms for Ordinary Differential Equations*. Springer, 2006.
- [5] L. Euler. E Motu Rectilineo Trium Corporum se Mutuo Attrahentium, Novi Commentarii. *Academiae Scientiarum Petropolitanae* 11, page pp. 144–151, 1767.
- [6] E. Fehlberg. Classical fifth-, sixth-, seventh-, and eighth-order Runge-Kutta formulas with stepsize control. *NASA Technical Report 287*, 1968.
- [7] E. Fehlberg. Low-order classical Runge-Kutta formulas with stepsize control and their application to some heat transfer problems. *National Aeronautics and Space Administration.*, 315, 1969.
- [8] E. Forest and R. D. Ruth. Fourth-order symplectic integration. *Physica D: Nonlinear Phenomena*, 43(1):105–117, 1990.
- [9] J. Frank. PHYS 7221 - The Three-Body Problem, special lecture. <https://pdf4pro.com/view/phys-7221-the-three-body-problem-lsu-7132be.html>, 2006. [Online; accessed 07-August-2023].
- [10] J. Galán, F. J. Muñoz Almaraz, E. Freire, E. Doedel, and A. Vanderbauwhede. Stability and Bifurcations of the Figure-8 Solution of the Three-Body Problem. *Phys. Rev. Lett.*, 88:241101, May 2002.
- [11] M. Henkel. Sur la solution de Sundman du Problème des Trois Corps, 2002.
- [12] G. W. Hill. On the part of the motion of the lunar perigee which is a function of the mean motions of the Sun and Moon. *Acta Mathematica*, 8:1–36, 1886.
- [13] C. G. Jacobi. Sur le mouvement d'un Point et sur un cas Particulier du Problème des trois Corps. *Compte Rendus de l'Académie des Sciences*, 3:59, 1836.
- [14] G. S. Krishnaswami. An Introduction to the Classical Three-Body Problem. *Resonance vol. 24*, page 87–114, 2019.
- [15] J.-L. Lagrange. Essai sur le Problème des Trois Corps. *Prix de l'Académie Royale des Sciences de Paris, tome IX, in vol. 6 of Oeuvres*, page 292, 1772.
- [16] A. Liapounoff. Problème Général de la Stabilité du Mouvement. Annales de la Faculté des sciences de Toulouse. *Mathématiques, Serie 2, Volume 9*, pages 203–474, 1907.
- [17] J. E. Mansilla. Stability of Hamiltonian Systems with Three Degrees of Freedom and the Three Body-Problem. *Celestial Mechanics and Dynamical Astronomy*, 94(3):249–269, Mar. 2006.
- [18] A. Margaris, N. Kofidis, and M. Roumeliotis. A detailed study of the Wolf's algorithm. *International Journal of Computer Mathematics*, 86(7):1135–1148, 2009.
- [19] K. R. Meyer and D. C. Offin. *Introduction to Hamiltonian Dynamical Systems and the N-Body Problem*. Springer, 2017.

- [20] E. F. Milone and W. J. Wilson. *Celestial Mechanics*, pages 31–60. Springer New York, New York, NY, 2008.
- [21] R. Montgomery. A New Solution to the Three-Body Problem. In *American Mathematical Society, Vol 48, 5*, 2001.
- [22] C. Moore. Braids in classical dynamics. *Phys. Rev. Lett.*, 70:3675–3679, Jun 1993.
- [23] Z. E. Musielak and B. Quarles. The Three-Body Problem. *Reports on Progress in Physics*, 77(6):065901, jun 2014.
- [24] N. Neil J. Cornish. What is a Lagrange Point? <https://solarsystem.nasa.gov/resources/754/what-is-a-lagrange-point/>, 2020. [Online; accessed 07-August-2023].
- [25] I. Omelyan, I. Mryglod, and R. Folk. Optimized Forest–Ruth- and Suzuki-like algorithms for integration of motion in many-body systems. *Computer Physics Communications*, 146(2):188–202, jul 2002.
- [26] Quarles, B., Eberle, J., Musielak, Z. E., and Cuntz, M. The instability transition for the restricted 3-body problem - iii. the lyapunov exponent criterion. *A&A*, 533:A2, 2011.
- [27] S. Ross, W. Koon, M. Lo, and J. Marsden. *Dynamical Systems, the Three-Body Problem, and Space Mission Design*. California Institute of Technology, 10 2022.
- [28] C. Simó. New Families of Solutions in N-Body Problems. In C. Casacuberta, R. M. Miró-Roig, J. Verdera, and S. Xambó-Descamps, editors, *European Congress of Mathematics*, pages 101–115, Basel, 2001. Birkhäuser Basel.
- [29] C. Simó. Dynamical properties of the Figure Eight Solution of the Three-Body Problem. *Contemp. Math.*, -1:209, 01 2002.
- [30] P. Virtanen, R. Gommers, T. E. Oliphant, M. Haberland, T. Reddy, D. Cournapeau, E. Burovski, P. Peterson, W. Weckesser, J. Bright, S. J. van der Walt, M. Brett, J. Wilson, K. J. Millman, N. Mayorov, A. R. J. Nelson, E. Jones, R. Kern, E. Larson, C. J. Carey, İ. Polat, Y. Feng, E. W. Moore, J. VanderPlas, D. Laxalde, J. Perktold, R. Cimrman, I. Henriksen, E. A. Quintero, C. R. Harris, A. M. Archibald, A. H. Ribeiro, F. Pedregosa, P. van Mulbregt, and SciPy 1.0 Contributors. SciPy 1.0: Fundamental Algorithms for Scientific Computing in Python. *Nature Methods*, 17:261–272, 2020.
- [31] A. Wolf, J. B. Swift, H. L. Swinney, and J. A. Vastano. Determining Lyapunov Exponents from a time series. *Physica D: Nonlinear Phenomena*, 16(3):285–317, 1985.
- [32] S. Wolfram. *A New Kind of Science*. Wolfram Media, May 2002.
- [33] P. Young. Physics 115/242, The Leapfrog Method and other “Symplectic” Algorithms for Integrating Newton’s Laws of Motion. <https://young.physics.ucsc.edu/115/leapfrog.pdf>, 2014. [Online; accessed 20-June-2023].
- [34] M. Šuvakov and V. Dmitrašinović. A guide to hunting periodic Three-body Orbits. *American Journal of Physics*, 82(6):609–619, 06 2014.

Appendices

A Source Code

This GitHub repository contains the source code and documentation for this thesis: <https://github.com/williamjones7/Dissertation>.